

UNIVERSITY OF HAWAII
The LIBRARY

PHILOSOPHICAL MAGAZINE

FIRST PUBLISHED IN 1798

2 Eighth Series

No. 16

April 1957

A Journal of Theoretical Experimental and Applied Physics

EDITOR

PROFESSOR N. F. MOTT, M.A., D.Sc., F.R.S.

EDITORIAL BOARD

SIR LAWRENCE BRAGG, O.B.E., M.C., M.A., D.Sc., F.R.S.

SIR GEORGE THOMSON, M.A., D.Sc., F.R.S.

PROFESSOR A. M. TYNDALL, C.B.E., D.Sc., F.R.S.

PRICE £1 5s. 0d.

Annual Subscription £13 10s. 0d. payable in advance

ALERE FLAMMAM.

Printed and Published by

TAYLOR & FRANCIS LTD.

RED LION COURT, FLEET STREET, LONDON, E.C.4

The Scientific Work of René Descartes

(1596—1650)

By

J. F. SCOTT, B.A., M.Sc., Ph.D.

With a foreword by H. W. TURNBULL, M.A., F.R.S.

This book puts the chief mathematical and physical discoveries of Descartes in an accessible form, and fills an outstanding gap upon the shelf devoted to the history of philosophy and science.

There is to be found in this volume the considerable contribution that Descartes made to the physical sciences, which involved much accurate work in geometrical optics and its bearing upon the practical problem of fashioning lenses, as also the deeper problems of light and sight and colour. The careful treatment that Dr. Scott has accorded to this work of Descartes is welcome, is well worth reading and will be an asset to all libraries. Publication is recommended and approved by the Publication Fund Committee of the University of London

212 pages, 7" × 10", amply illustrated

Price £1 - 0 - 0 net

First published July 1952

Printed & Published by

TAYLOR & FRANCIS, LTD.

RED LION COURT, FLEET STREET, LONDON, E.C.4

The L/K-Capture Ratio of Germanium 71†

By R. W. P. DREVER and A. MOLJK

Natural Philosophy Department, University of Glasgow

[Received November 9, 1956]

ABSTRACT

A direct measurement of the L/K-capture ratio of ^{71}Ge has been made using a special proportional counter system which avoids the effects of x-ray escape. One proportional counter is effectively enclosed by another, without any intermediate wall. With a gaseous source of germanium hydride and an argon filling at 6 atmospheres, the ratio of the L- and K-peaks from the central counter, in anticoincidence with the surrounding counter, was determined. The L/K-capture ratio was found to be $0.128^{+0.005}_{-0.003}$. In addition, in a separate measurement, a value of 0.53 ± 0.03 was obtained for the K-fluorescence yield of gallium.

§ 1. INTRODUCTION

THE ratio of the probabilities of decay by the capture of orbital electrons from the L-shell and K-shell has been determined experimentally for a number of nuclei, but the data available are still insufficient to provide a satisfactory check of the relevant theory. The situation has been reviewed recently by Radvanyi (1955) and by Robinson and Fink (1955), and very few nuclei were found for which experimental results could be compared with theory.

In general there are large discrepancies between calculated and measured values of the L/K-capture ratio. Relatively good agreement is found only for ^{37}A and ^{79}Kr , in the latter case after a recalculation of the experimental results with a revised value of fluorescence yield. In some of the other nuclei the disagreement may be due to uncertainties in decay schemes. A particularly large discrepancy in the case of germanium 71 cannot be explained in this way, however, since the decay is simple and well established. A further study of electron capture in this nucleus is therefore desirable and this is the subject of the present work.

Germanium 71 is a pure electron capture source with a half-life of 12.5 days (Bisi *et al.* 1955). The internal bremsstrahlung spectrum associated with the electron capture was studied first by Saraf *et al.* (1953) and Saraf (1954) who found agreement with the theoretical shape from the end point down to 100 kev. Langevin (1954 b) observed a low energy component

† Communicated by Professor P. I. Dee, F.R.S.

with longer half-life in his measured spectrum and suggested that the decay might be complex. However more recent work by Bisi *et al.* (1955) has shown that this effect was due to the presence of a radioactive contaminant, since their spectrum agreed closely with theory down to 50 keV when well purified sources were used. From the measured end point of the bremsstrahlung spectrum the transition energy is found to be 231 keV (Bisi *et al.* 1955) and the decay is allowed with $\log fT = 4.6$.

The theoretical value for the L/K-capture ratio of ^{71}Ge obtained from the calculations of Brysk and Rose (1955) with these data is 0.106. Experimentally a higher value of 0.30 has been found by Langevin (1954 b and 1955) using a proportional counter containing the source in gaseous form. The method employed in the present experiment, although somewhat different in principle, also depends on the measurement of a gaseous source with a proportional counter. It may therefore be useful to give a brief review of some of the features common to this type of measurement.

In a determination of an L/K-capture ratio with a gaseous source proportional counter the intensities N_L of the L-peak and N_K of the K-peak are measured. The observed K-peak is due to Auger electrons and to those x-rays emitted following K-capture that are absorbed in the filling gas. The L-peak is due to Auger electrons and x-rays following L-capture events as well as to L-radiation emitted, after K-capture, simultaneously with $K\alpha$ x-rays that escape undetected from the counter. If F is the K-fluorescence yield of the daughter element, k the fraction of $K\alpha$ x-rays in the K series and P the probability of a K x-ray escaping from the counter without being detected, then the L/K-capture ratio R is given by

$$R = \frac{N_L}{N_K} (1 - PF) - PFk.$$

The escape of L x-rays from the counter is usually small, and is neglected here.

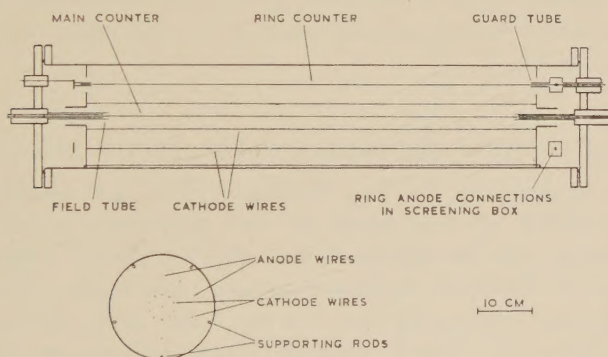
In practice it is convenient to choose the dimensions of the counter and the filling gas so that the probability P of x-ray escape approaches either 1 or 0. The former method is experimentally the simpler one. A small low pressure counter is used, preferably with a filling gas of low atomic number. The measurement of the L/K-capture ratio of ^{71}Ge by Langevin was performed in this way, propane being used as filling. Unfortunately, the wide scatter of measured values of fluorescence yield introduces some uncertainty into the result. Langevin took for the fluorescence yield of gallium the value 0.45 given by a semiempirical formula by Burhop (1952). However more recent values of fluorescence yield suggested by Broyles *et al.* (1953) and by Burhop (1955) are higher, and results of calculations by Rubenstein and Snyder (1955) and measurements by Heintze (1955) for argon and krypton show the same tendency. With the value of 0.50 of Broyles *et al.* the L/K-capture ratio found by Langevin is brought down from 0.30 to 0.19.

The alternative method of measuring an L/K-capture ratio, in which $P=0$, gives a result independent of the fluorescence yield and is therefore to be preferred. All radiations resulting from a K-capture or an L-capture event are integrated and recorded only in the corresponding K- or L-peak, so that the L/K-capture ratio is given directly. This method has been employed in the case of ^{37}A by Pontecorvo *et al.* (1949), and recently by Langevin and Radvanyi (1955). Its application to ^{71}Ge is more difficult since the half-thickness for absorption of the 9.2 kev K x-rays in argon at 1 atmosphere is 5.0 cm. For an escape correction to the final result of 5%, the diameter of a counter filled with argon to 6 atmospheres would have to be 1.0 metre. However with a technique developed in the present work the same accuracy can be achieved in a practicable counting system of moderate dimensions.

§ 2. OUTLINE OF THE METHOD

The arrangement consists effectively of two proportional counters, one inside the other, connected in anticoincidence. A diagram of the system is given in fig. 1. The inner circle of wires acts as cathode for the central proportional counter, while alternate anode wires in the outer

Fig. 1



Internal construction of the counter.

circle turn the surrounding layer of gas into a separate counter. With a gaseous source, and an argon filling at 6 atmospheres, the spectrum of pulses from the central counter in anticoincidence with pulses from the ring counter is measured. It may be shown that the ratio of the intensities of the L- and K-peaks then observed is closely equal to the L/K-capture ratio.

It should be noted first that with the filling used the half-thickness for absorption of K x-rays is 0.81 cm, and the probability of an x-ray passing out from the central counter and not being absorbed and detected in the ring counter is less than 0.1%. It will be neglected in this preliminary discussion, as will end effects.

All pulses due to L-capture events in the central counter are recorded in the L-peak. Incomplete absorption of radiations following a K-capture event in the central counter does not lead to the recording of a spurious L-count, since the escaping $K\alpha$ x-ray is detected in the surrounding ring counter and closes the gating circuit. Thus the number N_L of counts in the L-peak is equal to the number of L-capture events that have taken place in the central counter.

The total number of counts in the recorded K-peak is also equal to the number of K-capture events that have occurred in the central counter, although in this case the peak is made up of two separate components. One of these is due to K-capture events that take place, and are also detected in the central counter. The other component is due to K x-rays which are produced by K-capture in the surrounding layer of gas, pass into the central counter, and are absorbed there. Since the layer of gas is assumed to be infinitely thick, these x-rays compensate for the x-rays that escape from the central counter, provided the gating circuit is biased so that pulses corresponding to the L-absorption energy do not close it. The two components of the peak differ slightly in energy since the latter is caused by K x-rays while the former has the total K-absorption energy. In practice they are not resolved and the area of the complex peak gives the total number of K-capture events in the central counter.

The L/K-capture ratio is therefore given directly by the ratio N_L/N_K , though some small corrections are required for end effect and inefficiency of the ring counter.

§ 3. CONSTRUCTION AND OPERATION OF THE COUNTING SYSTEM

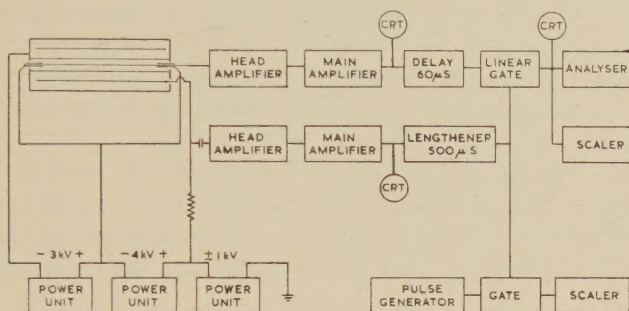
The wires making up the ring counter system are mounted between brass plates which are held apart by five supporting rods. The whole cage-like system can be removed from the containing vessel as a unit, which makes the fitting of the 20 wires relatively simple. The 10 cathode wires of the inner circle, and the 5 in the outer circle, are stainless steel 0.2 mm in diameter. The 5 counting wires, 0.07 mm in diameter, are fitted with guard tubes and are connected together inside the counter, the connections also being screened by an annular metal box. The central counter is end-corrected and has a sensitive length of 76.0 cm. Its diameter is 4.5 cm while the ring counters are slightly larger. Both central and ring counters operate at voltages in the region of 6.8 kv when filled to 6 atmospheres.

Pulses from the central counter, after amplification pass through a 60 μ sec delay line to a linear gate circuit and thence to a multichannel kicksorter, as shown in fig. 2. From the ring counter, pulses are fed to an amplifier, discriminator, and lengthener controlling the gate.

The counting rate in the ring counter is 15 times greater than that in the central counter. However with the electronic system shown, the high counting rate in the ring counter does not affect the efficiency of gating

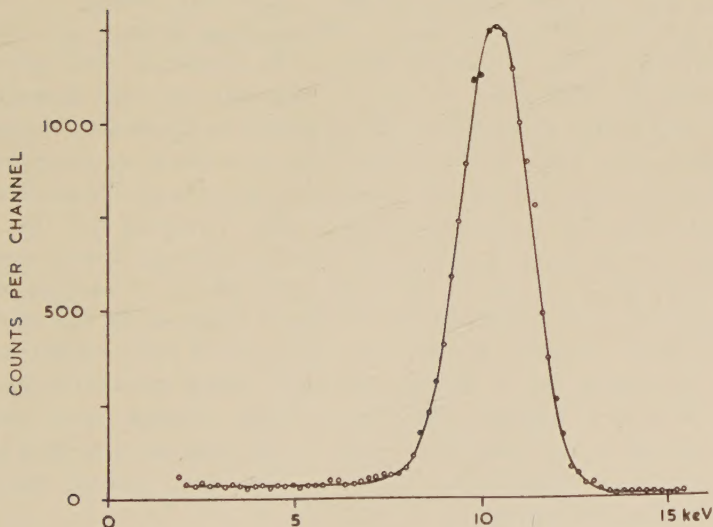
since the circuits controlling the gate are sensitive the whole time, even immediately after a pulse. There may be a reduction in the effective counting time but this does not alter the ratio of the measured intensities of the L- and K-peaks since the relative loss of time is the same in both cases. It is necessary that the time constant of the lengthener does not change and this condition is checked by a timing unit shown in the diagram, which measures directly the effective counting time, by counting pulses of constant repetition rate with a gated scaler.

Fig. 2



Schematic diagram of the electronic equipment.

Fig. 3

K-peak from a ^{71}Ge gaseous source, given by the ring counter system.

In view of the unusual design of the counter system its operation was checked by measuring the pulse distribution of the K-peaks given by the central centre and ring counters with a ^{71}Ge gaseous source. In the case of the central counter the symmetrical arrangement of the many wires

forming the cathodes leads to a field distribution which differs little from that obtained with a complete cylindrical electrode and the counter was found to behave normally. In the ring counters, the cathode wires are arranged so that the field distribution around the counting wires is distorted as little as possible. Satisfactory performance is obtained, as is shown by the 10.2 kev peak in fig. 3, which indicates in addition that there is no appreciable variation of gain between individual counting units.

For an accurate measurement of the L/K-capture ratio it is essential that the ring counter system has a high efficiency, in that every K x-ray absorbed in the gas causes a pulse large enough to trigger the gate circuit. The small amplitude of the low energy tail of the peak in fig. 3 gives evidence that the counter fulfills this condition sufficiently well. The major part of the tail is caused by end effect due to the absence of field correcting tubes, and by the natural background.

It may be remarked that the movement of the ions in the central counter induces small pulses of opposite sign on the anode wires of the ring counter system. Their amplitude is about 1/40 of that of the corresponding normal pulses, so they have no effect on the measurements.

§ 4. EXPERIMENTAL PROCEDURE AND RESULTS

Germanium 71 was made by (n, γ) reaction on germanium oxide at A.E.R.E. Harwell, and was stored for a time long enough to allow the 12-hour activity of ^{77}Ge to decay. Germanium hydride gas was then prepared by the action of sodium amalgam on a solution of the germanium oxide. The gas was dried by cooling with dry ice, and hydrogen was pumped off with the germanium hydride frozen at liquid air temperature.

The germanium hydride was found to have no effect on the operation of the counter at the low partial pressure of less than 0.1 mm of mercury used. The absence of residual activity after pumping out the counter indicated that there was no chemical reaction with the counter materials.

Measurements were carried out with argon fillings at various pressures up to a maximum of 6 atmospheres, this limit being set by the mechanical strength of the counter. Methane at a pressure of 15 cm of mercury was used as quenching gas. At each pressure, pulse spectra in the region of the 10.2 kev K-peak and the 1.3 kev L-peak were analysed. The change in energy range was made by altering the amplifier gain, all other conditions being kept constant. The gate control circuit was biased at 3 kev throughout.

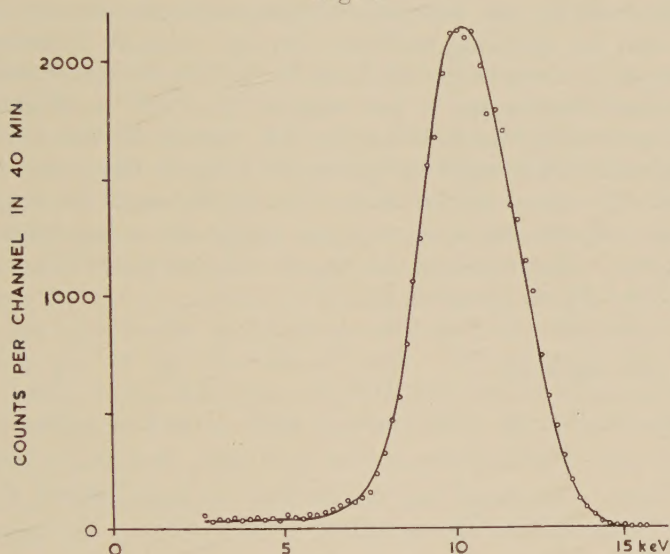
Typical spectra of K- and L-peaks obtained with the central counter in anticoincidence with the ring counter are given in figs. 4 and 5. In these diagrams the background, which was measured separately, has not been subtracted.

The half-width of the K-peak shown is slightly greater than would normally be expected at this energy due to the presence of the two

components, of K-absorption energy and K x-ray energy, and also partly to a technical fault in the assembly of the counter which made it difficult to centre the anode wire accurately. However the area of the peak is still well defined and this broadening does not affect the measurement.

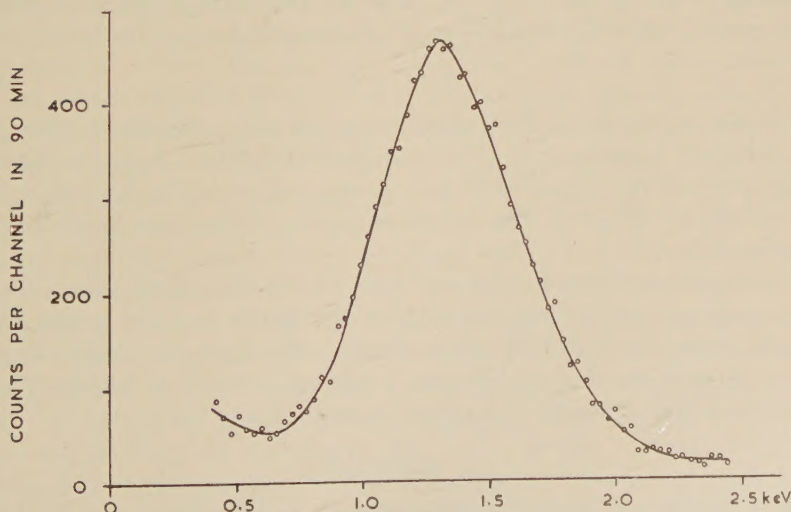
The ratio of the counting rates observed at various pressures from 2 to 6 atmospheres are given in the table. The small corrections required for kicksorter dead-time, which was 0.6 msec, have been applied.

Fig. 4



^{71}Ge K-peak from the central counter, in anticoincidence with the ring counter.

Fig. 5



^{71}Ge L-peak from the central counter, in anticoincidence with the ring counter.

At the lower pressures the condition of negligible x-ray escape through the ring counter, assumed above, is not fulfilled and high values of the L/K-ratio are obtained. At higher pressures when escape through the ring becomes small there is little variation with pressure. However even at 6 atmospheres some corrections have still to be applied to find the true value of the L/K-capture ratio since the shielding of the central counter by the ring counter is not quite complete.

K x-rays which leave the sensitive volume of the central counter through the ends are not detected. An approximate calculation by the methods used for shielding problems (see for example Glasstone 1956) shows that at 6 atmospheres the fraction P_1 of K x-rays emitted in the central counter that escape in this way is $P_1=7 \times 10^{-3}$. Further, some x-rays are prevented from entering the ring counter by the wires making up the cathode. The calculated probability P_2 for this is $P_2=7 \times 10^{-3}$. The remaining correction, for x-rays passing through the layer of gas forming the ring counter without being absorbed, is relatively small at 6 atmospheres. The width of the ring is then 7.6 half-thicknesses, and the probability P_3 for escape is $P_3=6 \times 10^{-4}$.

Pressure in atmospheres	2	3	4	5	6
Observed L/K-ratio (%)	16.5	14.4	13.6	13.5	13.5

When these corrections are taken into account, the L/K-capture ratio R is obtained from the measured ratio N_L/N_K by the expression

$$R = \frac{N_L}{N_K} [1 - (P_2 + P_3)F] - (P_1 + P_2 + P_3)Fk.$$

A mean of the values of N_L/N_K obtained from three separate measurements gives a value for the L/K-capture ratio of germanium 71 of

$$R = 0.128.$$

The statistical error of the measurement is 1%. However there is a possibility of a systematic error in establishing the shape of the low energy part of the L-peak, and to a lesser extent of the K-peak. With an estimate of this error, the overall accuracy of the final result may be stated as $(\pm 4)_2\%$.

In calculating the L/K-capture ratio above the values taken for the K-fluorescence yield of gallium and for the fraction of $K\alpha$ x-rays in the K-series were 0.50 and 0.86 respectively. However the result obtained is very insensitive to these factors, a change of 10% in either of them leading to a change in the L/K-capture ratio of only 0.5%.

§ 5. DISCUSSION

The L/K-capture ratio obtained here is considerably lower than that found by Langevin. However, as mentioned above, it is probable that

his high result is due in part to the value taken for the fluorescence yield of gallium.

In an attempt to check this explanation, the counter described here has been used also to make an independent measurement of the fluorescence yield. The experiment is described briefly in the Appendix. The value of the fluorescence yield obtained was 0.53 with an estimated accuracy of 6% and in addition the fraction of K α x-rays in the K-series was found to be 0.83. With these values the experimental result of Langevin comes into closer agreement with the result of the present measurement.

The theoretical calculation of the L K-capture ratio originally carried out by Marshak (1942) involves ratios of the components of L- and K-electron wave functions. These are becoming more accurately known now and have been recently computed by Rose and Jackson (1949) and by Brysk and Rose (1955). The L K-capture ratio of ^{71}Ge obtained from the results of the latter authors is 0.106, which is appreciably lower than the value found in the present measurement.

It seems difficult to explain the difference in the results by a systematic error in the experiment, and it is possible that the discrepancy arises in the calculation of the theoretical value. Recent work by Odier and Daudel (1956) shows that when correlations between the positions of the electrons are taken into account higher values of the L/K-capture ratio result, but at present correction factors are available only for helium, beryllium, and argon.

APPENDIX

The K-fluorescence Yield of Gallium

The fluorescence yield was measured, independently of the L/K-capture ratio, using the counter described above with the anticoincidence circuit disconnected. The counter was filled with methane to a pressure of 1 atmosphere together with a trace of germanium hydride source. The intensity of the K-peak in the central counter, which in this case was due to Auger electrons only, was measured. Argon was then added to bring the total pressure to 5 atmospheres and the intensity of the K-peak, due to both Auger electrons and x-rays was measured again.

After applying corrections for the absorption of K x-rays in the methane, which has a probability of 2.5%, and for the escape of K x-rays when the argon filling is used, which has a probability of 0.8%, the fluorescence yield of gallium was found to be 0.53. The accuracy is estimated as 6%.

In addition the fraction of K α x-rays in the K-series was determined from the intensity of the L-peak observed with the methane filling. After subtracting the component due to L-capture, calculated from the known L K-capture ratio, the rate of emission of K α x-rays is obtained. With similar corrections to those mentioned above, a value of 0.83 was found for the fraction of K α x-rays in the K-series of gallium. However

the difference between this value and the value of 0.865 used by Langevin is not considered significant.

ACKNOWLEDGMENTS

We would like to thank Professor P. I. Dee for his interest and encouragement. We are grateful to Dr. S. C. Curran for his continued interest and to Dr. G. M. Lewis for some helpful discussions. One of the authors (R.W.P.D.) would like to acknowledge the financial support of the Department of Scientific and Industrial Research, while the other is indebted to the University of Ljubljana for leave of absence.

REFERENCES

- BISI, A., GERMAGNOLI, E., ZAPPA, L., and ZIMMER, E., 1955, *Nuovo Cim.*, **2**, 290.
BROYLES, C. D., THOMAS, D. A., and HAYNES, S. K., 1953, *Phys. Rev.*, **89**, 715.
BRYSK, H., and ROSE, M. E., 1955, *Oak Ridge National Laboratory Report*, ORNL 1830.
BURHOP, E. H. S., 1952, *The Auger Effect* (Cambridge: University Press), p. 48; 1955, *J. Phys. Rad.*, **16**, 625.
GLASSTONE, S., 1956, *Principles of Nuclear Reactor Engineering* (New York: Van Nostrand Co., Inc.).
HEINTZE, J., 1955, *Z. Phys.*, **143**, 153.
LANGEVIN, M., 1954 a, *C.R. Acad. Sci.*, **238**, 2518; 1954 b, *Ibid.*, **239**, 1625; 1955, *Ann. de Physique*, **1**, 57.
LANGEVIN, M., and RADVANYI, P., 1955, *C.R. Acad. Sci.*, **241**, 33.
MARSHAK, R. E., 1952, *Phys. Rev.*, **61**, 431.
ODIOT, S., and DAUDEL, R., 1956, *J. Phys. Rad.*, **17**, 60.
PONTECORVO, B., KIRKWOOD, D. H. W., and HANNA, G. C., 1949, *Phys. Rev.*, **74**, 982.
RADVANYI, P., 1955, *J. Phys. Rad.*, **16**, 509.
ROBINSON, B. L., and FINK, R. W., 1955, *Rev. Mod. Phys.*, **27**, 424.
ROSE, M. E., and JACKSON, J. L., 1949, *Phys. Rev.*, **76**, 1540.
RUBENSTEIN, R. A., and SNYDER, J. N., 1955, *Phys. Rev.*, **97**, 1653.
SARAF, B., 1954, *Phys. Rev.*, **94**, 642.
SARAF, B., VARMA, J., and MANDEVILLE, C. E., 1953, *Phys. Rev.*, **91**, 1216.

Some Observations on the Nature of Fatigue Damage†

By P. J. E. FORSYTH

Metallurgy Department, Royal Aircraft Establishment, Farnborough, Hants.

[Received December 18, 1956]

§ 1. INTRODUCTION

It has been observed in a number of studies on the fatigue behaviour of metals that fatigue cracks are initiated along slip bands. This paper describes some observations on the nature of these bands at the stage when fatigue cracks are forming.

When the surface steps or grooves of slip are removed by electrolytic polishing, faint residual traces may remain or may be revealed by subsequent etching. These traces may be revealed in certain materials even after unidirectional strain (Jacquet 1945, McLean 1948, Samuels 1954). If slip occurred by a shear displacement only, then it should not be possible to reveal these bands. However, dislocations along a slip plane may make this a region of preferential etching if a reagent sensitive to these differences of lattice disorder is used. Certain reagents may produce rows of pits along slip bands and these pits have been interpreted as sites of discrete dislocations. Apart from the presence of disturbed lattice, other local changes may allow the slip traces to be revealed (Forsyth and Stubbington 1955). These changes may be very local recrystallization or polygonization, or slip band ageing accelerated by strain. Another suggested cause for the persistence of slip traces is the diffusion of oxygen down slip planes during a fatigue test (Wadsworth and Thompson 1954).

All of these effects are more likely to occur with fatigue stresses and to become more prominent with time. They are therefore most likely to be visible along slip bands which are in the stage of development into cracks, particularly near the ends of the initial cracks.

These bands are the only signs of permanent fatigue damage which can be detected microscopically. A particular case of residual bands or zones in aluminium 4% copper alloy fatigued at room temperature, has already been reported (Forsyth and Stubbington 1955). In order to reveal these bands specimens were etched in 10% NaOH solution, a relatively drastic etchant which no doubt greatly widened the affected fatigue zones.

§ 2. DAMAGE BANDS IN ALUMINIUM 7.5% ZINC 2.5% MAGNESIUM ALLOY

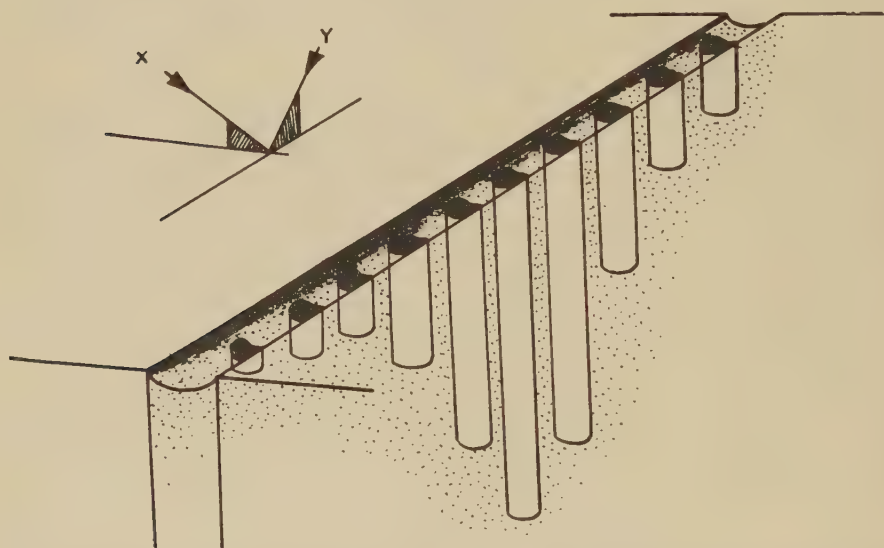
A number of specimens of the above alloy have been fatigued in torsion using a pendulum torsional vibrator. It has been observed that slip traces can be revealed by subsequent electrolytic polishing alone. The material was tested in the following condition :

† Communicated by the Author.

Solution heat treated 450°C for 1 hour, cold water quenched, then aged at 150°C for $\frac{1}{2}$ hour unless otherwise indicated. This treatment is not long enough to age harden the alloy to peak hardness but brings the hardness from 80 d.p.h. (solution treated condition) to 150 d.p.h., whereas peak hardness is about 185 d.p.h.

It was found that the effects which will be described also occurred in the solution treated and over-aged conditions but were less marked.

Fig. 3



A schematic illustration of a damage band with tubular holes distributed along it.

The zones which were observed are illustrated in fig. 1 (Pl.). They appear to be due to more rapid polishing along the slip traces and are best observed by oblique lighting. A series of holes are also revealed along these zones, as indicated by arrow A, fig. 1 (Pl.) and arrow A, fig. 2 (Pl.). It appears that fatigue cracks develop by breaking through these holes and it is very noticeable that they are very evenly spaced. The mean spacing measured on a number of specimens being 0.36μ . The distribution of these holes in the slip plane cannot as yet be explained. In spite of the random sectioning of the crystal planes which necessarily occurs with a polycrystalline specimen, there is a consistent spacing of holes from grain to grain. This suggests that the holes are in some way aligned with the surface and may exist as tubes normal to the specimen surface, the marked decrease in the number of holes visible as the surface is removed being due to the different lengths of tube. By sectioning specimens in a direction normal to the surface it is sometimes possible to observe these tubes as shown in fig. 2 (Pl.) (arrow B) although

due to their small size it is only rarely that they can be revealed in length by a random section. Figure 3 illustrates in schematic form a possible arrangement of these holes. The direction of oblique lighting is denoted by X normal to the slip trace and Y parallel to the slip trace. It can be seen from this diagram that X direction lighting is necessary to reveal clearly the grooves whereas Y direction lighting more clearly reveals the holes as there will be no obscuring shadow from the groove in this direction.

The fact that the slip zones are preferentially dissolved by the electrolyte suggests that these regions are more anodic than the general matrix, perhaps due to less stable anodic films forming at these places during the electropolishing process. It had been found in earlier work that zones depleted of solute atoms such as occur at the grain boundaries and subgrain boundaries in this alloy are less readily attacked and therefore appear as ridges after electropolishing. This is shown in fig. 4 (Pl.). Arrow A indicates an artificially made reference groove which is included to show that the boundary zones are in fact ridges. This specimen had been electropolished, at which stage only the ridges could be observed. It was subsequently etched for 20 seconds in Wassermann's reagent ($25 \text{ cm}^3 10\% \text{ H}_2\text{Cr}_2\text{O}_7$, $10 \text{ cm}^3 \text{ HCl}$, $100 \text{ cm}^3 \text{ NH}_4\text{OH}$, $2.7 \text{ cm}^3 \text{ HF}$ (60%) $500 \text{ cm}^3 \text{ H}_2\text{O}$) which then revealed the precipitate. The electropolishing alone will only reveal large precipitates which are formed after much longer ageing times. It is therefore suggested that the pits or holes which appear in the 'as polished' condition in the fatigued specimens are not precipitates which have been dissolved out, but are in fact voids along the slip planes. This has now been confirmed by the fact that these holes are clearly visible after mechanical polishing of sections of these specimens. It might also be suggested that as the slip traces electropolish as grooves whereas the depleted zones at the grain boundaries appear as ridges, the slip zones are richer in solute atoms than the surrounding matrix, and therefore more anodic. However, this is not necessarily the explanation as the presence of lattice defects would also be expected to make these zones more anodic than the less disturbed matrix.

If the holes along the slip zones are in fact due to the condensation of vacancies then it may be that the zones represent regions of fairly dense vacancy distribution where the defects are still in free motion and not yet attached to the holes. However, this does not seem likely as the slip zones in solution heat treated material do not etch as grooves; they are in fact extremely difficult to reveal but there is some evidence that they form ridges when electropolished. Experiments with other alloys and with pure aluminium have shown that the formation of holes seems to be a common occurrence although the grooves along slip striations are only clearly observed in aged alloys.

These slip zones and holes occur in profusion in the surface layers of the specimen but extend only a few microns into the surface grains, except for a few actively propagating cracks. Sections taken through fatigue specimens revealed that the cracks advance by the formation of holes along advancing slip zones. This is shown in fig. 5 (Pl.). Small

pits of a similar spacing to the holes found in the surface layers can be detected on the as polished surface of the fatigue specimens with no subsequent polishing. This is shown in fig. 6 (Pl.). This specimen was fatigued in the solution treated condition. That these pits represent the holes as they appear along the slip band itself is not absolutely certain, but it seems probable that this is so. Slip band extrusion occurs profusely along these bands, and if the surface is then repolished and refatigued the extrusion often occurs as narrow filaments from the slip zones between holes.

A subsequent solution treatment of specimens which had been fatigued (450°C for $\frac{1}{2}$ hr) removed the slip zones but did not heal all of the holes. It is not possible to ascertain whether any of the holes were healed as repolishing is necessary after the heat treatment, and there is such an intense density gradient of holes from the surface that no numerical comparison can be made. The fact that re-solution does not necessarily remove the holes also suggests that they are not the sites of precipitate.

§ 3. CONCLUSIONS

Fatigue stresses produce damage in such materials as aluminium 7.5% zinc 2.5% magnesium in the form of persistent bands which at an advanced stage contain rows of holes.

The bands can be removed by heat treatment, but the holes are not healed.

There is some evidence that these holes are in the form of tubes, penetrating to different depths in the surface of the grains.

Slip band extrusion occurs along these damaged planes and the presence of the holes may on occasion cause very fine extrusions in the form of filaments.

The holes can be observed after electrolytic polishing or mechanical polishing, but electrolytic polishing also reveals the bands in the form of grooves.

It has been ascertained that grooves may be produced by the presence of concentrations of solute atoms, and conversely zones depleted of solute atoms are electrolytically polished less rapidly than the matrix and appear as ridges.

Although pure aluminium and also solution heat treated aluminium 7.5% zinc 2.5% magnesium alloy show holes along the slip band traces, marked grooves are not observed. This suggests that the grooves are not primarily due to the presence of defects, but to variations in the distribution of the solute atoms.

REFERENCES

- FORSYTH, P. J. E., and STUBBINGTON, C. A., 1955, *J. Inst. Metals*, **83**, 395.
JACQUET, P. A., 1945, *Rev. Met.*, **42**, 133.
MCLEAN, D., 1948, *J. Inst. Metals*, **74**, 95.
SAMUELS, L. E., 1954, *Defence Standards Labs. Report* 206.
WADSWORTH, N. J., and THOMPSON, N., 1954, *Phil. Mag.*, **45**, 223.

Ratios of Specific Heat and High-Frequency Viscosities in Organic Liquids under Pressure, derived from Ultrasonic Propagation†

By E. G. RICHARDSON and R. I. TAIT
King's College, Newcastle-upon-Tyne

[Received September 9, 1956]

ABSTRACT

Measurements of the velocity and attenuation of plane sound waves in a number of organic liquids at pressures up to 10 000 lb/in.² have been made. From the velocity, the adiabatic compressibility is derived and from this, by comparison with the measured isothermal compressibility, the ratio of specific heats as a function of pressure is calculated.

By introducing the measured attenuation into the Kirchhoff formula an 'ultrasonic' viscosity as a function of pressure is also derived.

§ 1. INTRODUCTION

MEASUREMENTS of the (isothermal) compressibility of liquids under pressure have in the recent past been obtained in the main in piezo-metric experiments and of their viscosity from transpiration experiments. Recent developments in ultrasonic techniques have made it possible to measure the velocity of sound with precision and so to derive the adiabatic compressibility. In conjunction with the aforesaid value of isothermal compressibility, it is then possible to derive the ratio of specific heats of a fluid.

From measurements of the absorption of sound waves in the liquid it is possible, putting the coefficient into the Stokes-Kirchhoff formula, to find how the coefficient of (kinematic) viscosity varies with pressure, though it is true that the measured value of the latter coefficient may be a function of the frequency employed. The expression for the absorption coefficient (α) of plane waves of frequency f in a liquid of kinematic viscosity ν is $8\pi^2 f \nu / 3c^3$, c being the velocity of sound in the liquid.

The first measurements of ultrasonic velocity in liquids under pressure were made by Swanson (1933, 1934) using a Pierce interferometer at 200 kc/s in nine organic liquids. Next Biquard (1939) used the optical diffraction method devised by himself and Lucas (Lucas and Biquard 1932) in five liquids up to 650 atmospheres pressure (at 7 and 10 Mc/s). His accuracy was of the order of that reached by Swanson, the limit in both cases being governed by uncertain temperature fluctuations.

†Communicated by the Authors.

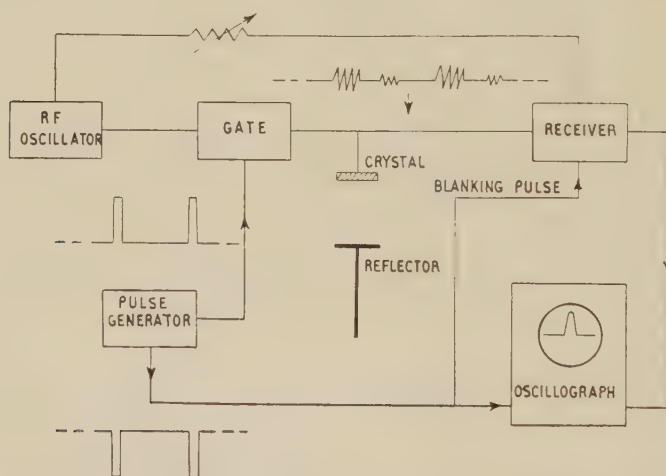
More recently a number of measurements of ultrasonic velocity to higher pressures have been made by several American investigators. As they confined their experiments to water they will not be discussed here.

Only Biquard has reported absorption measurements (in toluene) but his optical diffraction technique, though capable of good precision in measuring ultrasonic wavelengths, is scarcely amenable to that determination of amplitudes in different parts of the ultrasonic beam, necessary if absorption coefficients are to be deduced.

§ 2. APPARATUS

For the present experiments, both variable-path and fixed-path ultrasonic systems were built. It is common when working in liquids to send pulses, or short bursts of radiation, from the crystal source and to receive the echoes back from a reflector placed in the path of the wave. It is comparatively easy then to estimate the size of the echo as the path is lengthened at constant pressure or kept constant while the pressure is varied and so to measure the amplitude absorption coefficient. It is

Fig. 1



Block diagram of ultrasonic pulse generator and receiver, showing waveforms at three stages of modulation.

less common to use the pulse technique to measure wavelength and so to derive velocity, but Mason (1950) has described a method which is well adapted to experiments under high pressure, and a circuit based on this principle was used to measure wavelength in the present work.

A continuously running radio-frequency oscillator (fig. 1) supplies short pulses selected by a gating valve and applied to the transducer. Echoes from the reflector are received in the usual way but are then mixed with a set fraction of the original r.f. As the reflector is moved the phase

of the echo alters continuously, and as it moves in and out of phase with the original r.f., an echo 'beat' effect is observed on the oscilloscope screen. One such 'beat' or pulse maximum occurs for each half wavelength traversed by the reflector. A large number of such wavelengths can be counted, the change in path length observed and from the wavelength and frequency the velocity determined.

The technique thus combines the accuracy obtainable with a continuous wave method with all the advantages of the pulse method. An added advantage is that it can be used for very viscous liquids where high attenuation might make normal continuous wave methods impracticable.

All measurements were made in the Fresnel zone of the transducer, i.e. at distances $< R^2 \lambda$, where R is the radius of the transducer and λ the ultrasonic wavelength in the liquid, and with a reflector of greater radius than R . A check with a moving reflector showed that the attenuation was linear with path length up to $\frac{3}{4}R^2/\lambda$, after which the effects of beam divergence became apparent. Great care was exercised in setting the face of the reflector parallel to that of the crystal and in aligning both perpendicular to the path of the waves.

In using the fixed-path apparatus for absorption measurements some difficulty was experienced. The obvious method would be to measure the change in echo-size as the pressure is varied, but the adoption of such an expedient would overlook the fact that the characteristic impedance of the liquid varies with pressure and so, therefore, does the load on the crystal and the intensity reflected at the solid-liquid boundaries.

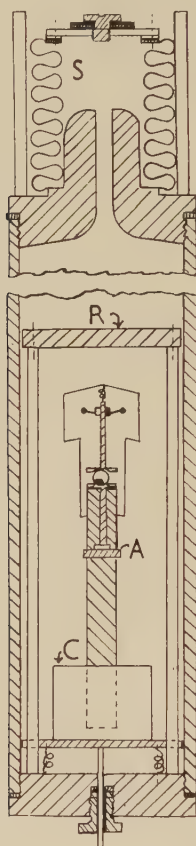
The arrangement finally adopted was to mount in the beam path an auxiliary reflector of small dimensions compared with the main reflector. A proportion of the beam was thus intercepted to provide a reference echo. Measurements were made by comparing echo levels from both reflectors and in this manner the main sources of error discussed above were eliminated.

The acoustic system was mounted in a steel vessel capable of withstanding 1000 atm pressure. Details of this and its associated equipment are given elsewhere (Tait 1957). Liquid was fed in from a reservoir and, after closing a cock, pressure was applied by screwing up a piston into a compression cylinder, connected to the main vessel. The acoustic measuring vessel was surrounded by a liquid jacket with a thermostat. The thermostat was set in operation overnight which meant that the system was given more than 12 hours to attain temperature equilibrium before measurements were started. The range of pressure, measured on a Budenberg gauge (N.P.L. calibrated), was then covered both up and down.

Some liquids were used in sufficient quantity (about 2 litres) to fill the whole system, including the compression cylinder, but in most cases the acoustic measurement chamber, which alone contained the liquid under test, was cut off from the compression cylinder and connecting pipes by a sylphon bellows, which communicated the stress applied to

water in the compression cylinder to the experimental liquid. Figure 2 shows the acoustic chamber with the subsidiary reflector as mounted for the absorption measurements.

Fig. 2



Fixed-path apparatus for absorption measurements; S, syphon; R, main reflector; A, auxiliary reflector; C, crystal mounting.

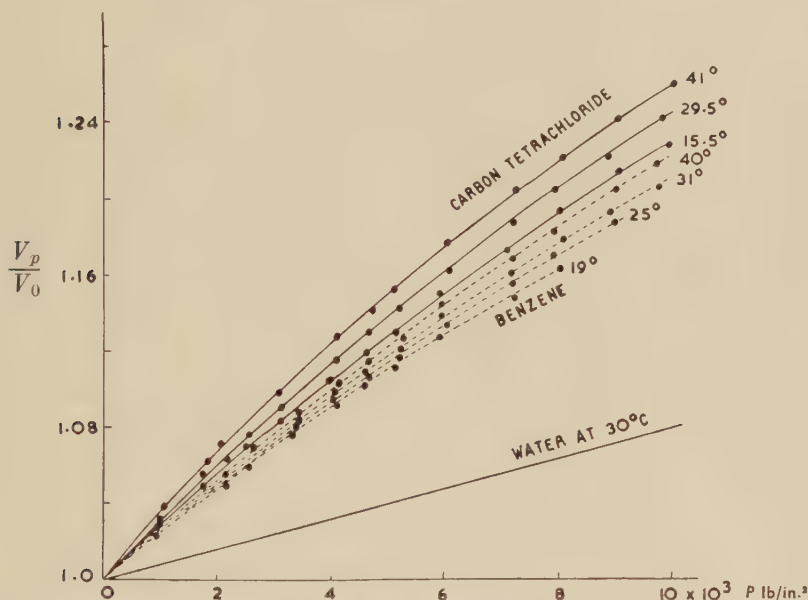
§ 3. RESULTS

In this paper results are reported in :

- (A) carbon tetrachloride and benzene, typical of non-associated liquids showing 'anomalous absorption' ;
- (B) ether and pentane, liquids with a high compressibility at room temperature ;
- (C) carbon dioxide and monofluor-trichlormethane or freon 11, typical of fluids which are vapours at n.t.p. ;
- (D) glycerine, having a high shear viscosity.

(A) Carbon tetrachloride and pentane were obtained in Analar purity. Tables 1 and 2 give the velocity results at 3 Mc/s and three or four temperatures and on fig. 3 they are plotted as isotherms. Swanson's points are rather scattered and bear a different slope to ours, but having regard to the difference in temperature there is excellent agreement between the present ones and Biquard's.

Fig. 3



Ratio of velocity V_p to that at atmospheric pressure V_0 in carbon tetrachloride and benzene, with water for comparison.

Table 1. Velocity in Carbon Tetrachloride

$T=15.5^\circ\text{C}$ $P \text{ lb/in.}^2 \quad V \text{ m/sec}$		$T=25^\circ\text{C}$ $P \text{ lb/in.}^2 \quad V \text{ m/sec}$		$T=40^\circ\text{C}$ $P \text{ lb/in.}^2 \quad V \text{ m/sec}$	
0	950	0	908	0	872
2280	1010	2000	962	3100	1058
3900	1047	4100	1014	4000	1080
5900	1090	5900	1054	6000	1024
8000	1130	8100	1098	8000	1065
10000	1165	10000	1132	9000	1083

In comparison with results obtained for water (for which a mean curve is given) the two striking features of the curves for benzene and carbon tetrachloride are the greater slope and the curvature. Over the measured temperature range V_p/V_0 increases steadily with temperature. This is in accordance with the observed increase in compressibility with temperature for these liquids.

In table 3 is shown the adiabatic compressibilities β_A which, together with the isothermal compressibilities β_I measured by Dolazalek and Scheidel (1920), enable values of γ to be calculated.

Table 2. Velocity in Benzene

$T=19^\circ\text{C}$		$T=25^\circ\text{C}$		$T=31.0^\circ\text{C}$		$T=40^\circ\text{C}$	
P lb/in. ²	V m/sec	P lb/in. ²	V m/sec	P lb/in. ²	V m/sec	P lb/in. ²	V m/sec
0	1326	0	1302	0	1276	0	1231
520	1342	450	1318	530	1291	510	1245
1030	1359	930	1332	1100	1307	940	1258
1570	1377	1460	1349	1530	1323	1390	1273
2130	1394	2010	1367	2060	1337	1870	1288
2760	1412	2580	1384	2620	1355	2340	1303
3400	1430	3180	1402	3210	1372	2860	1318
4100	1449	3820	1420	3830	1390	3390	1335
4820	1468	4510	1439	4490	1408	3960	1351
5590	1488	5240	1458	5180	1426	4540	1468
6400	1508	6020	1478	5770	1444	5170	1386
7280	1529	6780	1498	6500	1464	5870	1403
8200	1551	7660	1518	7330	1484	6570	1422
Freezes		8530	1540	7800	1487	7320	1440
		9270	1557	8070	1504	8100	1459
				9000	1525	8860	1478
				9570	1539	9770	1498

Table 3

P lb/in. ²	Carbon Tetrachloride at 15.5°C			Benzene at 19°C		
	$\beta_A \times 10^{12}$ cm ² dyne ⁻¹	$\beta_I \times 10^{12}$ cm ² dyne ⁻¹	γ	$\gamma_A \times 10^{12}$ cm ² /dyne	$\beta_I \times 10^{12}$ cm ² /dyne	γ
0	74.2	104.4	1.41	67.8	96.4	1.42
418	72.6	102	1.41	66.4	94.1	1.42
1392	68.3	96.3	1.41	63	87.8	1.40
2781	63.2	88.7	1.40	58.6	81.6	1.40
4180	58.8	81.5	1.39	55	75.4	1.37
5560	54.5	75.4	1.38	51.9	70.2	1.35
6960	51.3	69.2	1.35	48.9	65.1	1.34
8350	48.6	63.9	1.32	46.5	61.9	1.33

The values for γ are given to the nearest three figures. It will be observed that γ for both liquids decreases with pressure. For atmospheric pressure there are for comparison the values of γ : 1.43 for CCl_4 and 1.54 for C_6H_6 given by Schulze (1925). The discrepancy is well accounted for by the uncertainty in the isothermal compressibility values. Reference to the International Critical Tables and other sources shows that the values of isothermal compressibility given by different observers do not

agree within 5%. The error in the absolute values of γ may well be of the order of 3% but the figures given in the table should represent the relative change in γ to better than 1%.

Absorption in these two liquids was measured at 3 Mc/s and several temperatures. Table 4 gives the results in terms of the parameter α/f^2 and the kinematic viscosity corresponding to this frequency (ν_f) when α/f^2 is substituted in the Stokes-Kirchhoff formula. The fourth column gives the low-frequency or shear value of the kinematic viscosity

Table 4
Carbon Tetrachloride Benzene

P in lb/in. ² $\times 10^{-3}$	$\alpha/f^2 \times 10^{15}$	ν_f cs	ν_s cs	$\alpha/f^2 \times 10^{15}$	ν_f cs	ν_s cs
0	5.20	14.7	0.530	8.50	66.5	0.652
2	4.56	16.4	0.636	7.70	70.7	0.737
4	4.04	16.8	0.706	6.76	74.0	0.833
6	3.64	17.7	0.805	6.00	76.2	0.937
8	3.30	19.0	0.902	5.35	77.5	1.05
10	3.10	20.2	1.020	4.80	78.8	1.18
12	2.85	19.3	1.045	4.30	80.6	1.34

(The units of kinematic viscosity in the tables are centistokes.)

Table 5. Velocity in Ether in M/sec

P lb/in. ²	16°C	25°C	30°C	44°C
0	1023	976	945	862
560	1047	1002	976	892
1000	1071	1025	1003	921
1500	1093	1051	1028	946
2000	1117	1073	1050	968
2500	1138	1096	1073	992
3000	1157	1116	1094	1013
3500	1177	1137	1117	1133
4000	1198	1154	1137	1054
4500	1217	1174	1156	1075
5000	1233	1192	1176	1095
5500	1253	1209	1192	1113
6000	1268	1225	1207	1130
6500	1283	1241	1227	1148
7000	1300	1256	1241	1164
7500	1313	1272	1261	1180
8000	1328	1287	1274	1196
8500	1342	1302	1287	1211
9000	1358	1316	1300	1225†

† Extrapolated value.

(ν_s) calculated from the viscosity and specific volume data of Bridgman (1931) and Schulze (1925).

There are two contrary effects here, which one may expect to find in all liquids; the velocity isothermals (fig. 3) curve towards the pressure axis whereas the isotherms of shear viscosity curve up, so that if both factors are inserted in the Stokes-Kirchhoff formula to derive what one might call the 'classical' absorption coefficient, a minimum will appear (at about 10 000 lb/in.²) and thereafter the coefficient will rise.

(B) Pentane and ether have the highest compressibilities among common organic fluids which exist in the liquid state at n.t.p. Tables 5 and 6 show the velocity results at 3 Mc/s.

Table 6. Velocity in Pentane M/sec

P lb/in. ²	15°C	25°C	35°C	44°C
0	1027	986	944	908†
500	1049	1012	972	940
1000	1074	1035	998	970
1500	1100	1060	1025	998
2000	1122	1085	1050	1025
2500	1143	1107	1077	1050
3000	1167	1132	1102	1072
4000	1208	1175	1148	1118
5000	1247	1213	1187	1162
6000	1282	1253	1223	1202
7000	1319	1290	1262	1242
8000	1350	1327	1300	1278

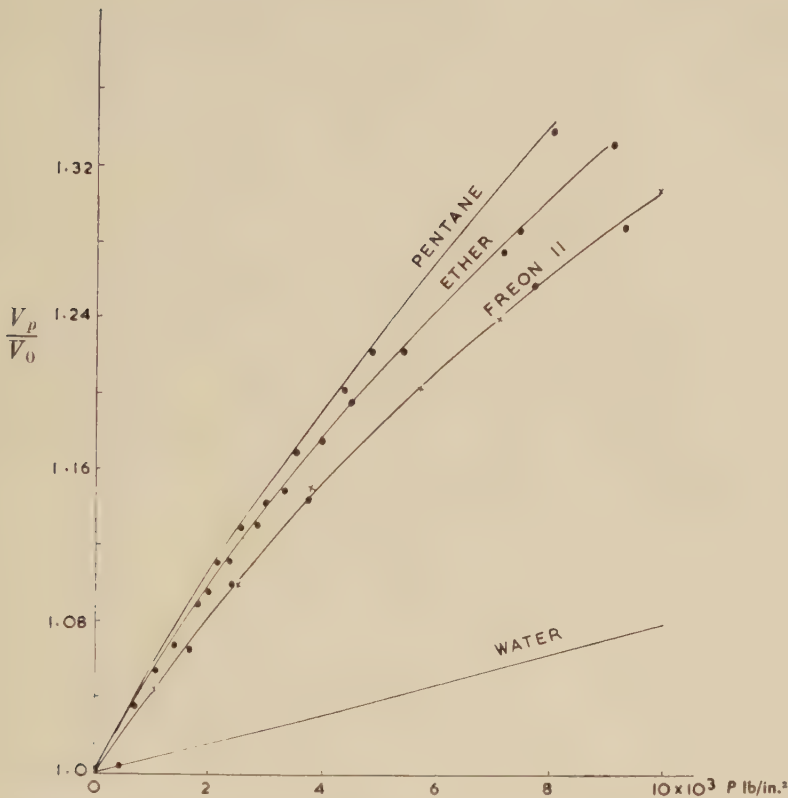
At 18°C both have the same velocity but that in ether is subject to the greater temperature coefficient.

The isotherms are shown in fig. 4 and the compressibilities and values for γ in table 7.

To calculate the isothermal compressibility of ether there are Bridgman's values, but we could not find any for pentane. Accordingly the compression cylinder itself filled with pentane was used as a piezometer, i.e. p - v plots were obtained by finding the number of turns of the (calibrated) screw driving the piston necessary to increase the pressure on the gauge by a determinate amount. This, of course, assumes that the change in volume of the thick steel vessel can be neglected in comparison with that of pentane over the range of pressure up to 10 000 lb/in.². This was checked with—less compressible—water in the apparatus, when it was found that deviations from published data on the isothermal compressibility did not exceed 3% at the highest pressures.

As the absorption shown by these two liquids is much less than by those in group (A), it was necessary to measure it at a higher frequency, i.e. 12 Mc/s. Furthermore it was necessary to make the measurements at room temperature or lower because of fluctuations in the signal at higher

Fig. 4



Ratio of velocity V_p to that at atmospheric pressure V_0 at 15°C in pentane, ether and freon 11, with water for comparison.

Table 7

Ether at 16°C				Pentane at 15°C		
$P \text{ lb/in.}^2$	$\beta_A \times 10^{12}$	$\beta_I \times 10^{12}$	γ	$\beta_A \times 10^{12}$	$\beta_I \times 10^{12}$	γ
0	126	170	1.34	151	190	1.26
2000	100	130	1.30	127	153	1.23
4000	87.5	112	1.28	115	136	1.175
6000	79.5	98	1.24	96.5	108	1.125
8000	71.5	87	1.22	87	93	1.07
10000	65.5	78	1.21	80.5	84†	1.045†

† Extrapolated value.

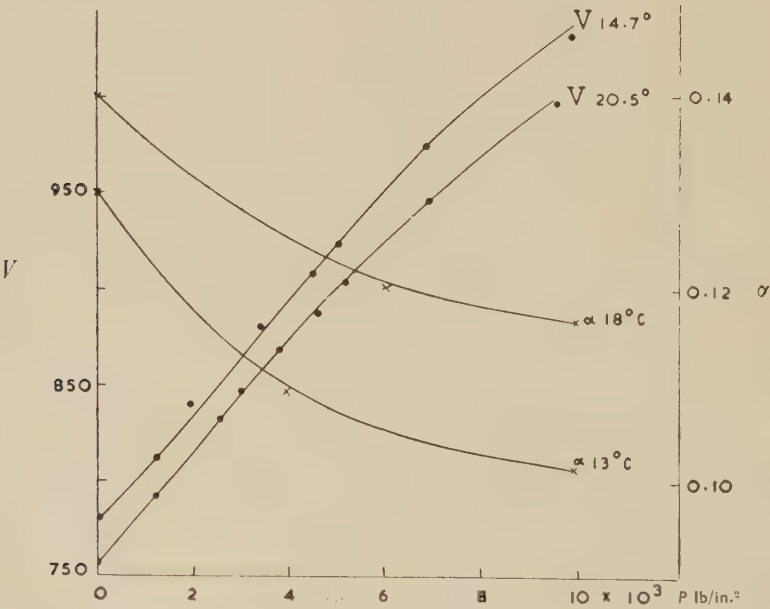
temperatures, attributed to scattering of the radiation by thermal inconsistencies such as occur near the critical state. Even at room temperature we must report some lack of reproducibility in the absorption measurements which reduces the accuracy of results below those of group (A).

A comparison of ultrasonic and shear viscosities appears in table 8.

Table 8

	Ether at 16°c			Pentane at 15°c		
$P \times 10^{-3}$	$\alpha/f^2 \times 10^{15}$	ν_f cs	ν_s cs	$\alpha/f^2 \times 10^{15}$	ν_f cs	ν_s cs
0	0.60	1.66	0.233	1.00	2.20	0.205
2	0.475	1.88	0.264	0.93	2.70	0.231
4	0.398	1.92	0.296	0.865	3.20	0.264
6	0.334	1.98	0.327	0.81	4.88	0.291
8	0.288	2.03	0.358	0.77	4.53	0.325
10	0.255	2.05	0.390	0.745	5.26	0.359

Fig. 5

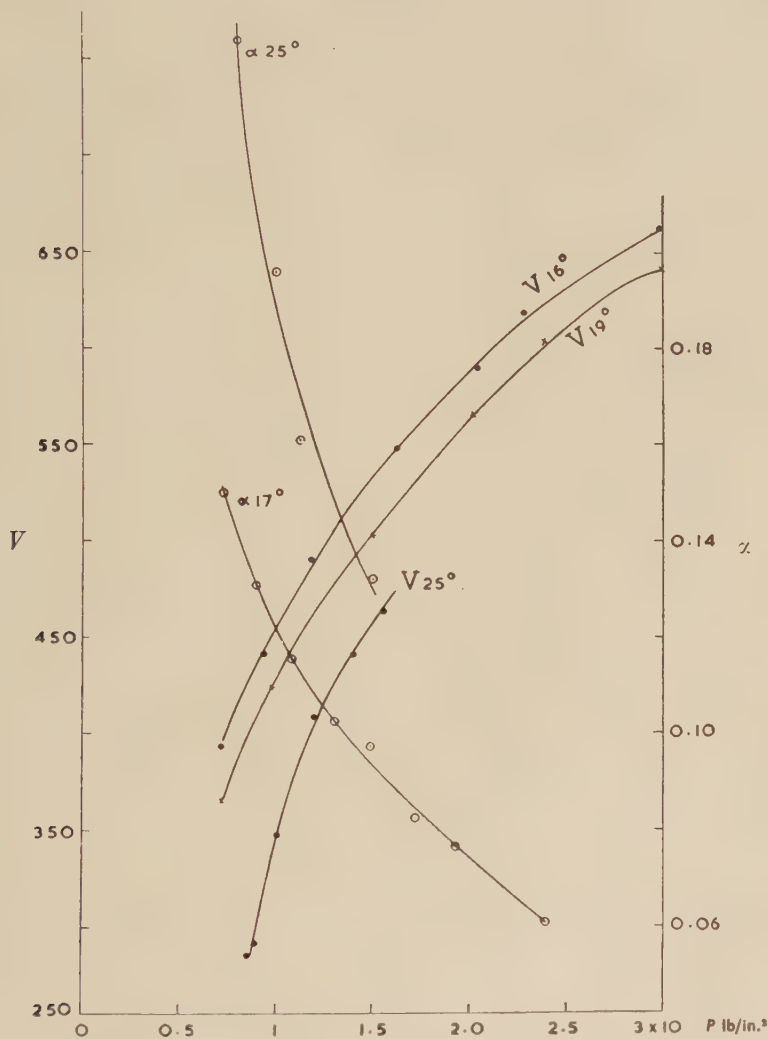


Velocity and attenuation in freon 11 at two temperatures.

(C) Measurements in the vapour state have been made on carbon dioxide (critical temperature 31°c, critical pressure 76 atm.) by Parbrook and Richardson (1952) and in monofluor-trichlor methane or freon 11 (critical temperature 198°c, critical pressure 43 atm.) by Miyahara and Richardson (1956). They, as liquids, are therefore in the same situation as the last two substances (group (B)) in that at room temperature they are highly compressible.

Table 9 gives the adiabatic and isothermal compressibilities of the liquids, the latter being derived for carbon dioxide from Bridgman's measurements and for freon 11 from our own.

Fig. 6



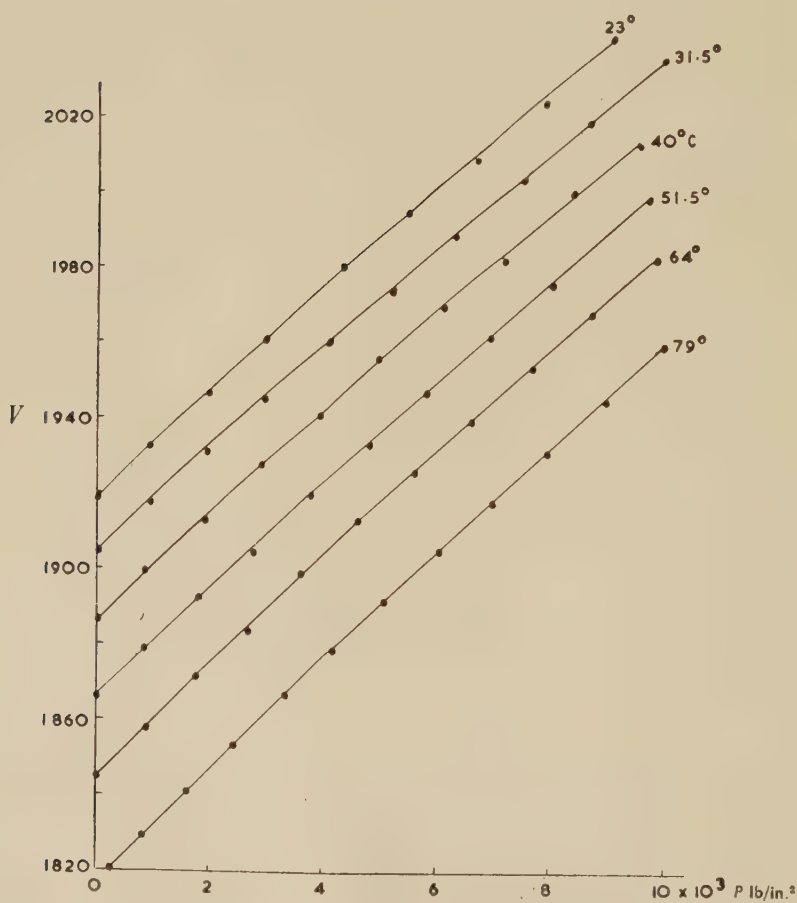
Velocity and attenuation in carbon dioxide at two temperatures.

In the present research measurements have been made on the liquid state at one frequency (1 Mc/s) and α/f^2 is plotted in the two figures (fig. 5 for CO_2 and fig. 6 for CCl_3F) which comprise these results. It is characteristic of fluids at super-critical pressures that the velocity isotherms are sharply curved. This is especially shown by these results in carbon dioxide, which carry the earlier measurements (Parbrook and Richardson 1952) to higher pressures.

Table 9

Carbon dioxide at 19°C				Freon 11 at 15°C			
P lb/in. ²	$\beta_A \times 10^{12}$	$\beta_I \times 10^{12}$	γ	P lb/in. ²	$\beta_A \times 10^{12}$	$\beta_I \times 10^{12}$	γ
1000	55.5	130	2.3	0	113	167	1.47
1500	41.6	78	1.9	2000	92.5	130	1.41
2000	30.8	55	1.75	4000	80.6	110	1.37
2500	26.8	40	1.50	6000	71.5	95	1.33
3000	21.7	32	1.35	10 000	59.5	74	1.24

Fig. 7



(D) Glycerine is typical of the rather few liquids which exhibit a large viscosity both to shear and to ultrasonic waves. The velocity isotherms are shown in fig. 7. Table 10 shows, as for the other liquids, values of adiabatic and isothermal elasticity. There appear to be no extant values for the latter, so we determined the volume: pressure relationships in our compression cylinder. So the γ values were calculated.

Finally, table 11 exhibits the (α/f^2) coefficients and the calculated 'ultrasonic viscosity'.

Bridgman has shear viscosities for comparison. It will be observed that the 'ultrasonic viscosity' is of the same order as that derived from shear experiments.

Table 10. Glycerine at 23°C

P lb/in. ²	0	2000	4000	6000	8000	10 000
$\beta_A \times 10^{12}$	21.95	20.9	20.4	19.9	19.6	19.4
$\beta_{\pm} \times 10^{12}$	28.0	25.5	24.0	23.0	22.5	21.0
γ	1.275	1.215	1.18	1.155	1.125	1.085

Table 11

P lb/in. ² $\times 10^{-3}$	$\alpha f^2 \times 10^{15}$	ν_f Stokes	ν_s Stokes
0	13.00	3.42	3.02
2	13.72	3.90	3.40
4	14.45	4.38	3.82
6	16.20	5.05	4.38
8	15.90	5.70	4.95
10	16.60	6.72	5.84

§ 4. DISCUSSION OF RESULTS

It is the purpose of this work to provide experimental data which might form a basis for theoretical discussion rather than to propound theories, to which indeed the velocity results do not lend themselves. No tabulation of absorption coefficients would however be complete without some reference to relaxation processes. It is well known that the postulate of a mean relaxation time for the molecules varying directly with pressure explains well the propagation of ultrasonic waves through gases, remote from their critical states, but this idea meets great difficulties in application to liquids because (a) no dispersion of velocity with frequency has been found, (b) the absorption per wavelength in most cases changes steadily with frequency in most liquids and does not show the peak required by relaxation theory. It is true that most of our attenuation measurements have been made at one frequency but the steady change

of the coefficient with pressure and its nearly constant ratio to shear viscosity gives no indication of relaxation within the range of frequency and pressure employed.

Of course, there remains to be explained the very much greater values of the deduced 'ultrasonic viscosity' in comparison to those in shear, except in glycerine. To justify a suggestion, on these grounds, that the Stokes-Kirchhoff formula is generally invalid and that its applicability to the case of glycerine is fortuitous would take us outside the scope of this paper, but the invocation of a bulk viscosity several hundred times that of the shear viscosity, which some have favoured, does not really help the understanding of this phenomenon.

REFERENCES

- BIQUARD, P., 1939, *Rev. d'acoust.*, **8**, 130.
BRIDGMAN, P. W., 1931, *Physics of High Pressure*, pp. 32, 130.
DOLAZALEK, F., and SCHEIDEL, F., 1920, *Z. Phys. Chem.*, **94**, 72.
LUCAS, R., and Biquard, P., 1932, *J. de Phys.*, **3**, 464.
MASON, W. P., 1950, *Piezoelectric Crystals and their Application to Ultrasonics*, 374.
MIYAHARA, Y., and RICHARDSON, E. G., 1956, *J. Acoust. Soc. Amer.*, **28**, 1016.
PARBROOK, H. D., and RICHARDSON, E. G., 1952, *Proc. Phys. Soc. B*, **65**, 437.
SCHULZE, F. A., 1925, *Z. Phys.*, **26**, 153.
SWANSON, J. C., 1933, *Rev. Sci. Instrum.*, **4**, 603; 1934, *J. Chem. Phys.*, **2**, 689.
TAIT, R. I., 1957, *Acustica*, **7**, No. 3.

On the Texture of Evaporated Films†

By R. B. KEHOE

Physics Department, Imperial College, London ‡

[Received September 24, 1956]

ABSTRACT

Copper, silver and gold have been evaporated onto heated cleavage surfaces of alkali halide crystals in an electron diffraction camera. The diffraction patterns have been studied continuously as the depositions were carried out and the crystalline arrangement in the films has been deduced as a function of thickness. When the growth is epitaxial the orientations are predominantly parallel, with subsidiary twinning and the (112) orientation. The proportion of the latter orientations, the crystal size and the degree of disorientation at different levels in the films may vary considerably. Single crystal growth by evaporation is found in certain cases to cease beyond a certain thickness; an explanation of this is put forward. Fine structure effects have been observed in the patterns. These effects have been analysed in some detail, and possible explanations are suggested.

§ 1. INTRODUCTION

It is now well known that a metal layer condensed from the vapour onto a single crystal surface may, under certain conditions, crystallize epitaxially. Study of this phenomenon originated with the now classic experiment of Lassen and Bruck (1935) who deposited silver onto cleavage surfaces of rocksalt maintained at various temperatures. For substrate temperatures of over 100°C the silver was found to give an electron diffraction pattern characteristic of a single crystal oriented with its cubic axes parallel to those of the rocksalt. Since then the great deal of work which has been carried out on the epitaxy of metallic layers has been largely dominated by attempts to explain the observed orientations in terms of the geometrical theories of Royer (1928, 1954) and Menzer (1938) and the more recent ideas of Engel (1953) and of Frank and van der Merwe (1948 a, b). These seek to explain orientation solely in terms of the relative atomic spacings and arrangements in the contact planes of the substrate and the deposit. No other line of approach appears to have been considered theoretically. The experimental results on epitaxy have led Neuhaus (1952) to suggest that the hardness of the substrate may

† Communicated by Dr. M. Blackman.

‡ Now at the Research and Development Laboratories, U.K.A.E.A., Culcheth, Warrington.

be important, and very recently Gottsche (1956) has shown that the substrate hardness can be related to the degree of epitaxy in deposits of copper, silver, gold and aluminium condensed onto four different alkali halide crystals.

In a study of twinning in oriented deposits of silver on rocksalt (henceforth denoted thus: Ag/NaCl) Kirchner and Cramer (1938) found that the crystallographic structure in the films varied with the mean thickness. In particular, diffraction spots from twinning on $\{111\}$ planes, not observed from films only 8 Å thick, were strong in the patterns from films of thickness 200 Å but were again weak in films of 1000 Å thickness. Such a result makes it clear that the greatest care must be exercised in any discussion on the structure of condensed layers. The true orientation of the deposit on the substrate can only be inferred from deposits a few angstroms thick. Once the substrate is covered with the deposit material it will cease to have any direct effect on further deposits which can, and in many cases do, crystallize in a different way. The mode of crystallization of the continued deposit will, at any thickness, depend primarily upon the crystalline nature of the surface, on the temperature of that surface, on the rate of evaporation and on the residual gas pressure in the apparatus. The structural changes which occur in evaporated deposits at different stages during their growth have been the subject of very little experimental work. Uyeda (1942) has studied Ag/NaCl at 350°C and also the evaporation of silver onto a number of other substrates by carrying out the evaporation in the electron diffraction camera. This work was not extensive, the results on Ag/NaCl, for example, being little more detailed than those of Kirchner and Cramer (1938). Recently much work has been published on the structure and topography of oriented films as shown by combined electron microscopy and diffraction (e.g. Yoshida 1956, Fischer and Richter 1955), but the films used have been comparatively thick (≈ 1000 Å) and have not been studied during their formation. Trillat *et al.* (1956) have used a novel technique in the study of a Au/NaCl, 400°C deposit. Bombardment of such a deposit by high energy ions in the electron diffraction camera causes the gold to evaporate and thus the deeper layers successively produce diffraction until the substrate pattern appears. It was found that the initial 1000 Å deposit gives a Debye-Scherrer pattern but that when a certain amount of gold is removed, an oriented single crystal pattern of gold appears and persists until the rocksalt pattern shows through. The catastrophic effect which the ion beam has on the gold must, however, preclude any detailed deductions on the structure of deposited layers.

In the work described here, the metals copper, silver and gold have been evaporated onto heated alkali halide cleavage surfaces under carefully controlled conditions. The evaporations were carried out in an electron diffraction camera and so the crystalline nature of the films could be studied continuously from the thinnest detectable deposits of mean thickness less than 1 Å to the maximum thickness of about 200 Å.

§ 2. APPARATUS

The details of the specimen chamber, which incorporates a specimen furnace and an evaporator, have been described elsewhere (Kehoe *et al.* 1954, 1956 a). The diffraction patterns were recorded on film, thus allowing a large number of exposures to be made during the course of an experiment.

The rate of evaporation from a bead of molten metal is approximately constant and it is therefore possible to estimate the deposit thickness at any stage of an experiment from a knowledge of the time taken for the evaporation of a known weight of the metal. Thicknesses found in this way were in tolerable agreement with estimates based on the thickness at which the Kikuchi pattern from the substrate became obscured. The latter thickness has been determined for copper by Newman and Pashley (1955) with the aid of a radio-active isotope. The rate of deposition was always 3–4 Å per minute. Each experiment lasted about an hour and during this period the temperature of the specimen was held constant to within a few degrees.

§ 3. THE STRUCTURE IN EVAPORATED FILMS

In nearly all the orientations observed in this work the plane of the metal deposit parallel to the (001) cleavage surface of the substrate contains a [110] direction oriented parallel to the [110] directions of the substrate surface. For such orientations it is necessary to name only the deposit plane which is parallel to the substrate surface.

In general, the diffraction pattern of a deposit consists of spots from one or more orientations superimposed on Debye-Scherrer rings from that portion of the substance which has crystallized at random. The relative intensities of the spot and ring patterns give an indication of the proportions of oriented and disoriented material. When a surface is studied in reflection, only the uppermost 10 Å or so of the specimen contribute to the pattern and the proportions estimated refer to this thickness only.

3.1. *The Evaporation of Copper*

The principal substrate was rocksalt and the first results given are of the Cu/NaCl experiments. Estimates of the orientation proportions are given in table 1 for a series of substrate temperatures. The character of the crystallization at some temperatures depends markedly on the deposit thickness. At 160°C and below the orientation tends to improve with thickness but at the highest temperatures random crystallization occurs on initially perfect orientation.

In a few experiments with each of the three metals an interesting, transitory feature of the diffraction patterns was noticed. The pattern from the substrates comprised spots and Kikuchi lines and bands. Immediately the evaporation was started, very faint diffuse haloes appeared in addition to the much stronger substrate pattern. The visibility of the haloes was poor and in many experiments it was difficult to be sure of

their presence. At a mean deposit thickness of about 2 Å, the haloes could no longer be distinguished, the diffraction rings or spots from the deposit having developed and increased the background intensity of the pattern. It must be presumed that these haloes resulted from amorphous or liquid-like aggregates of deposit atoms on the flat substrate surface. The most prominent halo lay for each metal between the (111) and (002) Debye-Scherrer ring positions.

Table 1. Orientation proportions in the copper/rocksalt films

Substrate temperature (°C)	Mean deposit thickness		
	2 Å	12 Å	200 Å
20	O	O	O
90	O	D	D
130	C	B	B
160	B	B	A
195	A	A	A
230	A	A	A
265	A	A	A
315	A	A	B
345	A	A	B
385	A	A	B

Key: A: completely oriented.
 B: mostly oriented.
 C: oriented and random crystal comparable.
 D: mostly random.
 O: completely random.

The spot pattern from the substrate became obscured at a deposit thickness of about 6 Å, while the Kikuchi pattern persisted until the thickness was about double this value.

Orientation was first observed at 90°C and the growth characteristics were almost identical at 130°C. At deposit thicknesses of less than 12 Å the orientation was solely parallel, i.e. the cubic axes of the copper were parallel to those of the rocksalt. The mean crystallite size was about 30 Å. At 12 Å mean thickness two further orientations occurred to a small extent and continued in the same proportion as the deposit was further built up. These were the (112) and (221) orientations, the latter arising from twinning on the {111} planes of the parallel crystallites.

At substrate temperatures of 160°C and over, the initial, and dominant, orientation was again parallel, with the twin and (112) orientations appearing at 12 Å. Figures 1 and 2 show the diffraction patterns from deposits of 2 Å and 20 Å respectively on rocksalt at 160°C. The mean crystallite size was about 50 Å at this thickness. The extent of the twinning in the deposit increased with thickness and reached a maximum at 50 Å to 80 Å and double diffraction between the parallel and twin

orientations was then considerable. The tendency to twin decreased as the thickness went beyond 100 Å. While the twinning was at its maximum, the strong diffraction spots of the parallel orientation became slightly streaked towards the shadow edge. The behaviour after this stage differed in the two temperature ranges 160–265°C and 315–385°C. In the lower range the streaks in the diffraction patterns became very strong and almost masked their parent spots. This is clearly illustrated in fig. 3, the pattern from 160 Å of copper at 160°C. The streaks arise from refraction of the spots and show the copper surface to be smooth. Kikuchi bands from the copper were usually seen at this stage, showing a considerable degree of perfection in the deposit. Faint streaks were observed along the $\langle 111 \rangle$ directions of patterns, due to the presence of $\{111\}$ stacking faults in the parallel orientation. Furthermore, the spots of the twin orientations were streaked along their $\langle 111 \rangle$ directions, again an indication of stacking faults. This can be seen in fig. 3.

In the temperature range 315–385°C, the refraction streaks which appeared at about 60 Å were sharper and did not lengthen as the evaporation continued. In the main, the patterns retained their cross grating nature, indicating a rough surface. At about 100 Å thickness random crystallization started, the proportion increasing with thickness.

A few deposition experiments were carried out with potassium chloride, bromide and iodide substrates. Below 220°C for potassium chloride and below 150°C for the other two salts the structure of the deposited copper was, thickness for thickness, exactly like that on rocksalt below 160°C. Above these temperatures the similarity was with Cu/NaCl above 300°C in that the surfaces were never observed to become smooth and random crystallization occurred when the thickness reached 100 Å.

Fine structure effects were observed in some Cu/KI experiments; they are described and analysed in § 4.

In diffraction patterns from the thinnest layers (less than about 6 Å) the sharp streaks and spots from the substrate still showed, and provided a standard spacing with which to compare the deposit spacing. This could be done with an accuracy of about 1% and to within this figure the copper spacing was found in all experiments to have its normal value.

3.2. The Evaporation of Silver

Silver has been condensed on to rocksalt and potassium bromide with almost identical results. The relative proportions of oriented and disoriented crystallites have been estimated in table 2. At all temperatures there was a tendency towards disorientation as the films were built up.

At 50°C and 90°C the initial orientation was solely parallel, but at 10 Å the twin and (112) orientations appeared to a small extent. The crystal size at this stage was about 50 Å. There were no further changes in the character of the deposits as more silver was deposited. The mode of growth of the silver is clearly similar to Cu/NaCl up to 130°C. The similarity with copper growth also holds at higher substrate temperatures.

Ag/NaCl and Ag/KBr at 145°C, 180°C and 215°C correspond to Cu/NaCl in the range 160–265°C. A minor difference was that when the twin and (112) orientations appeared, the (111), (115) and

Ag (112) $[1\bar{1}0] \parallel \text{NaCl } (001) [100]$

orientations were also observed.

Finally silver deposition at temperatures over 215°C was similar to Cu/NaCl 315–385°C. At no temperature were Kikuchi bands observed from silver deposits. No changes in the silver lattice spacing were observed.

Table 2. Orientation proportions in silver layers

Substrate temperature (°C)	Mean deposit thickness		
	2 Å	12 Å	100 Å
20	O	O	O
	O	O	O
50	C	C	C
	B	B	B
90	A	A	B
	A	A	B
145	A	B	B
	A	A	B
180	A	A	B
	—	—	—
215	A	A	B
	A	B	B
255	B	B	B
	—	—	—
295	B	B	B
	—	—	—
340	A	B	B
	A	B	B

Key :

NaCl
KBr

Symbols as in table 1.

3.3. The Evaporation of Gold

Gold was deposited only on to rocksalt. The proportion of orientation, estimated in table 3, again tended to decrease with thickness.

Orientation was first observed at 130°C and up to 230°C was of a type not found with copper or silver. The thinnest deposits gave a diffuse halo pattern which resolved into rings and spots from the parallel and (111) orientations in comparable proportions. At about 10 Å, the twin, (112), (115) and other unidentified orientations began to appear. As the deposition continued the intensity in the diffraction pattern arising from oriented gold decreased until, at 150 Å, the only spots remaining were

those of the (111) orientations on the centre line. Crystallization had thus become random except for a slight tendency for the close packed (111) planes to form parallel to the substrate surface.

With the substrate at 260°C, the sequence was the same until the thickness of the gold reached 40 Å, when the parallel orientation instead of dying out became more prominent at the expense of the (111) and other orientations. This process reached completion at about 80 Å when only the parallel and twin orientations remained. At 150 Å the gold surface tended to become smooth.

Table 3. Orientation proportions in gold/rocksalt films

Substrate temperature (°C)	Mean deposit thickness		
	2 Å	10 Å	100 Å
20	O	O	O
85	O	O	O
130	O	C	D
160	C	C	D
190	C	C	D
230	D	C	C
260	O	C	C
295	B	A	see text
315	A	A	see text
330	A	A	see text
385	A	A	see text

Symbols as in table 1.

At 295°C the change in crystallization sequence reached its final form, and did not change further at higher temperatures. The initial orientation was solely parallel with crystallite size about 50 Å. Refraction streaks appeared at 20 Å. A crystal size increase occurred when twinning commenced at 40 Å thickness. Between 80 Å and 100 Å thickness, the gold surface became very smooth and also Kikuchi bands appeared. At about 120 Å, a tendency of the gold to crystallize at random became apparent and at 150 Å the proportion of disoriented gold was appreciable. The ratio of intensity in the spot pattern to that in the ring pattern depended markedly on the incident angle of the electron beam. This is seen in figs. 4 and 5, which are patterns from a 150 Å deposit. At a glancing angle of 0.7 the contribution of oriented crystallites to the pattern is negligible, whereas at 1.7 the contributions from oriented and random gold are comparable. The situation is qualitatively the same after a further 25 Å deposit but the proportion of spots for a given angle of the electron beam is even less.

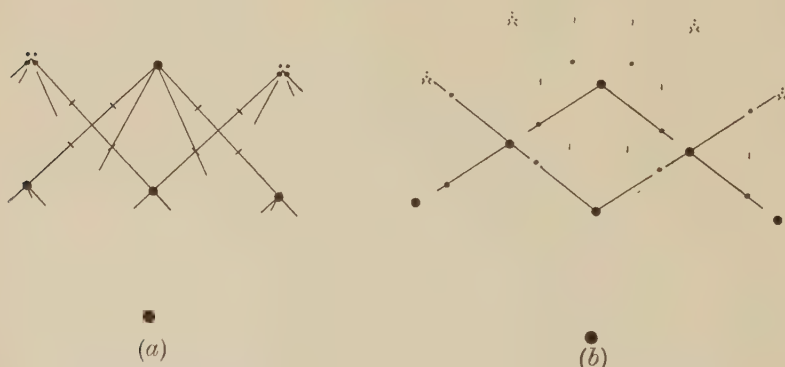
No changes of lattice parameter were detected in the initial gold deposits.

§ 4. SUBSIDIARY DIFFRACTION EFFECTS

In § 3, the main crystallographic features of the metal deposits have been described. A number of secondary effects observed in the diffraction patterns and which do not permit of such definite interpretations form the subject of this section.

In patterns from smooth copper surfaces, Cu/NaCl 160–265°C, extra streaks were observed midway between the normal spots at the [100] and [010] azimuths. These might have been due to adsorbed monolayers of gas. Oxygen monolayers on copper cube faces have been studied by Schlier and Farnsworth (1954) by the diffraction of slow electrons. They found two stable arrangements, the surface density of oxygen in one being twice that in the other. In the present work such monolayers would only be detectable on a smooth surface. The more densely packed oxygen layer would produce diffraction streaks coincident with the copper refraction streaks. However, the other type of layer would produce additional streaks midway between those from the copper at the [100] and [010] azimuths. It seems likely, therefore, that the streaks arose from an adsorbed monolayer of oxygen, but it must be noted that a similar arrangement of any other atoms, e.g. nitrogen, would produce similar continuous streaks. They are not consistent with a distortion of the copper atoms on the (001) surface having the periodicity of the unit cell.

Fig. 6



Patterns from 200 Å of copper on potassium iodide at 220°C.
(a) [100] azimuth. (b) [110] azimuth.

The fine structure effects mentioned in connection with Cu/KI took the form of fine lines ('spines') and very small spots or short dashes ('specks'). The appearance of spines and specks can be interpreted unambiguously in terms of thin filaments of intensity in reciprocal space (Kehoe *et al.* 1956 b). The relevant features of the patterns at the [100] and [110] azimuths of Cu/KI 220°C are shown diagrammatically in fig. 6. The spines at the [100] azimuth are consistent with filaments passing through all reciprocal lattice points in the following directions: [102], $\bar{1}02$, [012], $0\bar{1}2$, [101], $\bar{1}01$, [011] and $0\bar{1}1$. These bundles of filaments produce the

spines at the $[100]$ azimuth and some of the specks which occur are associated with them. The above filaments give neither spines nor specks at the $[110]$ azimuth. The remaining specks at the $[100]$ azimuth and those at the $[110]$ azimuth are consistent with $\langle 111 \rangle$ bundles of filaments passing not through the integral reciprocal lattice points but through $0, \frac{2}{3}, \frac{2}{3}$ and all equivalent points. The expected hexagonal symmetry of these bundles would be achieved if extra parallel filaments passed through the integral points in the $\langle 111 \rangle$ directions. Such filaments occur as a result of stacking faults, in any case, and would mask spines in these positions.

A slightly different type of fine structure was observed in patterns from Ag NaCl 340°C and Ag KBr 340°C . Short, sharp spines appeared at the $[100]$ azimuth passing through spots in the $[010]$, $[01\bar{1}]$ and $[011]$ directions. No specks were observed. The intensity in reciprocal space was examined by making exposures every 2° between the $[100]$ and $[110]$ azimuths. The short spines were found not to disappear off azimuth but continuously to change direction and finally to merge with the stacking fault streaks at the $[110]$ azimuth. They therefore arise from thin $\{111\}$ sheets of intensity surrounding each reciprocal lattice point.

The spots and refraction streaks in the patterns from smooth silver and gold surfaces always split into two components separated by twice the distance of the Ewald sphere from the expected positions of the intensity in reciprocal space. The effect was not confined to the parallel orientation but was observed with spots of the (112) and (111) orientations also. No interpretation of this effect can at present be offered.

In the patterns from some smooth copper and gold deposits there occurred streaks, normal to the shadow edge, and bearing no simple relation to the metal lattice spacing. Moreover, their general appearance was quite unlike that of refraction streaks or spines. It was concluded that they were produced by an oriented impurity, in the form of either a monolayer or of crystallites giving diffraction only by double scattering with the metal.

§ 5. DISCUSSION

The results in §3 show clearly that in the most important aspects the crystalline arrangements in layers of each of the three metals on each of the substrates are similar. The crystallization is random at low substrate temperatures, and at higher temperatures the orientation is predominantly parallel. The twin and (112) orientations occur almost invariably at a mean thickness of 12 \AA . The quality of the deposited crystal generally improves with thickness until a thickness of $60\text{--}100\text{ \AA}$ is reached when the general tendency to disorientation manifests itself.

There is so far insufficient experimental data to permit of a definite interpretation of the diffuse haloes which were observed in a number of experiments during the initial stages of deposition. It has been shown that during the evaporation of copper onto a flat (111) silver surface the

deposited atoms can migrate over distances of the order of $1\ \mu$ (Kehoe *et al.* 1956 b). It is probable that the migrating units are not only single atoms but also liquid-like groups of atoms which crystallize only when sufficient energy is lost to the substrate and a suitable site is found. With the initial conditions of a clean flat surface and a sufficient density of migrating groups, the latter would be expected to contribute to the diffraction pattern, and it seems likely that this is the origin of the haloes.

The crystallites which thus form at this initial stage are widely separated on the substrate surface and are therefore influenced by only the substrate during crystallization. It is only for such deposits that epitaxy should properly be discussed, as Gottsche (1956) has recently pointed out. In his experiments he studied the orientation of deposits sufficiently thin for the crystallites to be widely separated. For each metal-substrate pair two substrate temperatures can be defined: T_0 , below which the deposit is completely random, and T_{\min} , above which orientation is complete. The values obtained for T_0 and T_{\min} in the present work are given for rocksalt substrates in table 4. For comparison, Gottsche's corresponding results are given in parentheses. The two sets of results show the same trends but naturally differ in details owing to different evaporation rates and substrate quality.

Table 4. Limiting Epitaxial Temperatures

	T_0 ($^{\circ}\text{C}$)	T_{\min} ($^{\circ}\text{C}$)
Ag/NaCl	20-50 (100)	50-90 (150)
Cu/NaCl	90-130 (100)	160-195 (150)
Au/NaCl	130-160 (120)	285-305 (400)

The departure from solely parallel orientation occurs when the mean thickness is about $12\ \text{\AA}$, i.e. when the surface coverage is 20-40%. The appearance of the twinning and of the (112) orientation marks the end of the ideal epitaxy experiment. The proximity of crystallites on the surface is such that strains develop, to be relieved only by the formation of subsidiary orientations. Twinning is brought about by stacking faults on {111} type planes and it might be expected that stacking faults in the twins themselves would occur, and produce further derived orientations which may be termed 'secondary twins'. However, there is no evidence of any such orientations in the above or any other work. The (112) orientation does not seem to have any simple structural relationship with the parallel orientation.

The size of crystallites in layers thinner than $50\ \text{\AA}$, and in many cases thicker, lies between $40\ \text{\AA}$ and $60\ \text{\AA}$. Keith (1956) has studied by x-rays the crystallite size in copper deposited on to surfaces at -183°C and subsequently annealed at room temperature. In high vacuum (better than

10^{-7} mm Hg) the original 40 Å crystallites grew to 400 Å by this process, but in the presence of oxygen the upper limit obtained by annealing was only 60 Å owing to an adsorbed oxygen layer on the copper surfaces. This seems to be in agreement with the present work in which the residual pressure in the apparatus was relatively high (between 10^{-3} and 10^{-4} mm Hg).

The respective temperature ranges for copper, silver and gold, in which smooth surfaces form, are probably those in which the mobility of the deposited atoms allows cracks and strains between adjacent crystallites to be coherently covered. The subsidiary orientations then weaken as uniform parallel crystals of large lateral size are formed. The relative perfection of the crystals is also indicated by Kikuchi patterns in the cases of copper and gold deposits. The appearance of disoriented crystallization in hitherto perfect deposits of copper and gold shows that crystal growth by evaporation on to a smooth (001) surface will not continue indefinitely, probably a direct consequence of the high surface mobility. While the crystal surface is rough there is an abundance of sites for parallel crystallization, but once a smooth surface has developed, sites will no longer be present to the same extent and consequently migration distances will be much greater. If, for any reason, disoriented patches should be present, they would provide sites and would grow more quickly than the regions of smooth parallel crystal. The slightly raised polycrystalline islands, increasing their surface coverage as the deposition is continued, would produce exactly the effects found with gold deposits in § 3. Trillat *et al.* (1956) observed that both parallel and polycrystalline gold existed in layers on rocksalt at 400°C, but their technique did not allow any further investigation of the phenomenon.

The high sensitivity of the structure in the evaporated films to the substrate temperature suggests that there is no large temperature increase at the surface of the deposit. Rises of a few hundred degrees which are claimed to occur in certain instances (Murbach and Wilman 1953, Wilman 1955) must be ruled out here.

Spines and specks in a diffraction pattern have for the first time been fully interpreted in terms of intensity in reciprocal space (§ 4). Elementary diffraction theory shows that sharp, uniform filaments of intensity can result either from extensive plane monolayers of atoms or from absent monolayers in an otherwise perfect crystal. Similarly, sharp sheets of intensity which were observed in reciprocal space from Ag/NaCl—340°C deposits can arise from extra or absent lines of atoms in the silver. The existence of dislocations in the deposits is an obvious possible explanation. The diffraction patterns of two dislocation models have been calculated (Wilson 1949, Suzuki and Willis 1956) and that of Wilson may be relevant to the effects observed from Ag/NaCl. He has shown that screw dislocations produce round the reciprocal lattice points discs of intensity perpendicular to the dislocation axis. Further work would be needed to compare the experimental work with the theory in full.

ACKNOWLEDGMENTS

The author wishes to express his thanks to Dr. M. Blackman for numerous helpful discussions during the course of this work. He is also indebted to the University of London and to the Department of Scientific and Industrial Research for grants.

REFERENCES

- ENGEL, O. G., 1953, *J. Res. Nat. Bur. Stand., Wash.*, **50**, 249.
 FISCHER, E. W., and RICHTER, H., 1955, *Ann. d. Phys.*, **16**, 193.
 FRANK, F. C., and VAN DER MERWE, J. H., 1949 a, *Proc. Roy. Soc. A*, **198**, 205 ;
 1949 b, *Ibid.*, **200**, 125.
 GOTTSCHÉ, H., 1956, *Z. Naturforsch.*, **11 a**, 55.
 KEHOE, R. B., NEWMAN, R. C., and PASHLEY, D. W., 1954, *J. Sci. Instrum.*,
31, 399 ; 1956 a, *Brit. J. Appl. Phys.*, **7**, 29 ; 1956 b, *Phil. Mag.*, **1**, 783.
 KEITH, H. D., 1956, *Proc. Phys. Soc. B*, **69**, 180.
 KIRCHNER, F., and CRAMER, H., 1938, *Ann. d. Phys.*, **33**, 138.
 LASSEN, H., and BRUCK, L., 1935, *Ann. d. Phys.*, **22**, 65.
 MENZER, G., 1938, *Z. Krist.*, **99**, 378.
 MURBACH, H. P., and WILMAN, H., 1953, *Proc. Phys. Soc. B*, **66**, 905.
 NEUHAUS, A., 1952, *Z. Elektrochem.*, **56**, 453.
 NEWMAN, R. C., and PASHLEY, D. W., 1955, *Phil. Mag.*, **46**, 927.
 ROYER, L., 1928, *Bull. Soc. Franc. Min. Crist.*, **51**, 8 ; 1954, *Ibid.*, **77**, 1004.
 SCHLIER, R. E., and FARNSWORTH, H. E., 1954, *J. Appl. Phys.*, **25**, 1333.
 SUZUKI, T., and WILLIS, B. T. M., 1956, *Nature, Lond.*, **177**, 172.
 TRILLAT, J. J., TERAOKA, N., TERTIAN, L., and GERVAIS, H., 1956, *J. Phys. Soc., Japan*, **11**, 406.
 UYEDA, R., 1942, *J. Phys.-Math. Soc., Japan*, **24**, 809.
 WILMAN, H., 1955, *Proc. Phys. Soc. B*, **68**, 474.
 WILSON, A. J. C., 1949, *Research, London*, **2**, 541.
 YOSHIDA, S., 1956, *J. Phys. Soc., Japan*, **11**, 129.

Relativistic Theory of Meson-Nucleon Scattering†

By S. F. EDWARDS and P. T. MATTHEWS

Department of Mathematical Physics, University of Birmingham, England

[Received November 5, 1956]

ABSTRACT

An effective range theory of low energy meson-nucleon scattering is developed based on the relativistic pseudo-scalar interaction. An approximate relativistic equation is derived which, unlike the ladder approximation to the Bethe-Salpeter equation, preserves crossing symmetry. The equation is solved approximately and all divergences are removed by renormalization before going to the low energy limit. The resulting equations for the phase shifts depend on only one parameter—the coupling constant. With a suitable choice of this constant the p-wave phases, in particular that of the $\frac{3}{2}, \frac{3}{2}$ phase, are in good agreement with experiment. The s-wave phases are of the right order of magnitude, but do not show the observed strong dependence on isotopic spin.

§ 1. INTRODUCTION

IN a previous paper (Edwards and Matthews 1957, to be referred to as I) a conceptually extremely simple derivation was given of the Chew and Low (1956) no-recoil effective range formula for meson-nucleon scattering. This derivation was based on the idea of an effective potential arising from pseudo-vector coupling. According to the effective range theory, the experimental points, appropriately plotted, lie on a straight line. The theory contains two positive parameters (the coupling constant g^2 and the cut off) and both are used in fitting this line. Thus apart from the general feature of leading to an effective range formula, only the sign of the slope, or physically the fact that the resonance occurs in the $J=\frac{3}{2} T=\frac{3}{2}$ state, is specifically predicted by the theory of paper I. The coupling constant required agrees with that determined by photo-production.

In this paper we give a relativistic generalization of I, starting from the renormalizable γ_5 coupling. We reproduce effective range formulae, but the theory is renormalized before the low energy limit is taken, so that only *one* parameter (the coupling constant) remains. It is shown that it is still possible to obtain a very reasonable fit to the experimental data on the (33) phase shift with qualitatively correct results for the (11) and (13) phase shifts. The coupling constant required remains at the value

† Communicated by Professor R. E. Peierls, F.R.S.

which agrees with the photoproduction data. This theory also gives s-wave phase shifts of the correct magnitude and some isotopic spin dependence observed experimentally. This is discussed further below.

To derive these results we put as a condition on our relativistic theory, that it reduces simply to the non-relativistic theory, and the approximate solution must reproduce the well known exact solution in the no-recoil limit for pair theory. It is important to note that this condition is not satisfied by the ladder approximation to the Bethe-Salpeter equation. This gives the Tamm-Dancoff approximation in its non-relativistic limit, which, as explained in I, excludes virtual meson pair creation, and actually replaces a trivial algebraic equation by an integral equation.

In § 2 we derive a new relativistic equation for the scattering T -matrix, which does not suffer from these defects. This equation is solved approximately in § 3 for the low energy p-wave phase shifts and in § 4 for the s-wave phase shifts.

§ 2. RELATIVISTIC THEORY

The Lagrangian L is given by

$$L = \frac{1}{2}(\partial_\nu \phi_\alpha \partial_\nu \phi_\alpha + \mu^2 \phi_\alpha^2) + J_\alpha \phi_\alpha + \bar{\psi}(i\gamma_\mu \partial_\mu - m + if\theta_\alpha \phi_\alpha)\psi, \quad (2.1)$$

where θ_α is the operator which defines the interaction, J_α is an external source, and ϕ_α includes a quantized field and a classical unquantized field ϕ_α^{ex} . Then the equation for the complete one nucleon propagator is (suppressing all space variables)

$$\left[S^{-1} + g\theta_\alpha \left(\phi_\alpha - i \frac{\delta}{\delta J_\alpha} \right) \right] \mathcal{G}(\phi) = \delta, \quad (2.2)$$

where

$$S^{-1} = \gamma_\mu \partial_\mu + i(m - i\epsilon). \quad (2.3)$$

If $\Delta_{\alpha\beta}$ is the complete meson propagator

$$-i \frac{\delta}{\delta J_\alpha} = \Delta_{\alpha\beta} \frac{\delta}{\delta \phi_\beta}. \quad (2.4)$$

Iterating eqn. (2.2) once, gives

$$\begin{aligned} S^{-1} \mathcal{G}(\phi) S^{-1} = S^{-1} & - \left[f\theta_\alpha \left(\phi_\alpha + \Delta_{\alpha\beta} \frac{\delta}{\delta \phi_\beta} \right) - f^2 \theta_\alpha \left(\phi_\alpha + \Delta_{\alpha\gamma} \frac{\delta}{\delta \phi_\gamma} \right) \right. \\ & \left. \times S\theta_\beta \left(\phi_\beta + \Delta_{\beta\pi} \frac{\delta}{\delta \phi_\pi} \right) \right] \mathcal{G}(\phi) S^{-1}. \end{aligned} \quad (2.5)$$

The T -matrix for meson-nucleon scattering is determined by

$$T_{rs} = \left[S^{-1} \frac{\delta^2 \mathcal{G}(\phi)}{\delta \phi_r \delta \phi_s} S^{-1} \right]_{J=\varphi^{\text{ex}}=0}. \quad (2.6)$$

Carrying out the differentiation on (2.5) we get

$$\begin{aligned} T_{rs} = & V_{rs} + V_{rt} \Delta_{tp} S T_{ps} + V_{st} \Delta_{tp} S T_{pr} \\ & + \frac{1}{2} V_{tp} S \Delta_{ti} \Delta_{pm} \frac{\delta^2 T_{rs}}{\delta \phi_i \delta \phi_m}. \end{aligned} \quad (2.7)$$

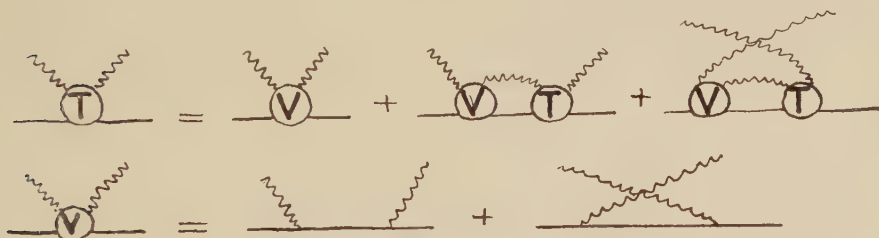
where

$$V_{rs} = f^2(\theta_r S \theta_s + \theta_s S \theta_r). \quad (2.8)$$

Note that V , S , and T are matrices both in γ -space and in the position of the nucleon, and matrix multiplication is implied. The suffices given explicitly carry both the charge label and the position of the nucleon.

This equation is exact. The approximation of taking only the first two terms on the right-hand side is precisely equivalent to the ladder approximation to the Bethe-Salpeter equation. This is very artificial from our present point of view, and the approximation we shall adopt is to take the first three terms. This obviously preserves the crossing symmetry, and the simplest technique of solution discussed below when applied to pair theory can be shown to reproduce the correct equation in the no-recoil limit. (It is true, in general, that the final term is predominantly a self energy effect in the limit of low energies and consists of a multiple of the first three terms which is absorbed in renormalization. Thus the condition mentioned above is satisfied. The proposed equation is shown graphically in fig. 1.

Fig. 1



Written in full with nucleons and mesons having incoming four vectors \mathbf{R} , \mathbf{P} and outgoing \mathbf{S} , \mathbf{Q} respectively, and meson charge indices r , s ,

$$T_{rs}(\mathbf{P}, \mathbf{Q}; \mathbf{R}, \mathbf{S}) = V_{rs}(\mathbf{P}, \mathbf{Q}; \mathbf{R}, \mathbf{S}) + \int V_{rt}(\mathbf{P}, \mathbf{P} + \mathbf{X}; \mathbf{R}, \mathbf{R} - \mathbf{X}) S(\mathbf{X} + \mathbf{P}) \\ \times \Delta(\mathbf{R} - \mathbf{X}) T_{ts}(\mathbf{P} + \mathbf{X}, \mathbf{Q}; \mathbf{R} - \mathbf{X}, \mathbf{S}) d^4 \mathbf{X} \\ + \int V_{st}(-\mathbf{Q}, \mathbf{X} - \mathbf{Q}; \mathbf{R}, \mathbf{R} - \mathbf{X}) S(\mathbf{X} - \mathbf{Q}) \Delta(\mathbf{R} - \mathbf{X}) \\ \times T_{ts}(\mathbf{X} - \mathbf{Q}, -\mathbf{P}; -\mathbf{X} + \mathbf{R}, \mathbf{S}) d^4 \mathbf{X}, \quad (2.9)$$

where $\mathbf{P} + \mathbf{Q} + \mathbf{R} + \mathbf{S} = 0$ and

$$V_{rs}(\mathbf{P}, \mathbf{Q}; \mathbf{R}, \mathbf{S}) = f^2 \theta_r S(\mathbf{P} + \mathbf{R}) \theta_s + f^2 \theta_s S(\mathbf{R} - \mathbf{Q}) \theta_r. \quad (2.10)$$

Spinor indices are not shown. We shall be interested in the value of T on the energy shell in the centre of mass system, i.e.

$$\left. \begin{aligned} \mathbf{P} &= (p_0, \mathbf{p}) = [(p^2 + \mu^2)^{1/2}, \mathbf{p}], \\ \mathbf{Q} &= (q_0, \mathbf{q}) = [(q^2 + \mu^2)^{1/2}, \mathbf{q}], \\ \mathbf{R} &= (r_0, \mathbf{r}) = [(r^2 + m^2)^{1/2}, \mathbf{r}], \\ \mathbf{S} &= (s_0, \mathbf{s}) = [(s^2 + m^2)^{1/2}, \mathbf{s}]. \end{aligned} \right\} \quad (2.11)$$

variational principle to the non-relativistic problem, as has been mentioned in I, so our solution below could also have been obtained by a relativistic treatment of the Cini-Fubini procedure. In other problems such as the two nucleon system, the two approaches would appear to be quite different however.

The approximate solution of (2.9) can therefore be constructed from a knowledge of the graphs of fig. 2 and those obtained from them by crossing. Their values, retaining only p-wave contributions, are, after renormalization,

$$\left. \begin{aligned} (\alpha) &= -i(2\pi)^4 f^2 \tau_r \tau_s \boldsymbol{\sigma} \cdot \mathbf{p} \boldsymbol{\sigma} \cdot \mathbf{q} / 4m^2 \omega, \\ (a) &= -3f^4 \tau_r \tau_s (\pi^2 / 2mi) \boldsymbol{\sigma} \cdot \mathbf{p} \boldsymbol{\sigma} \cdot \mathbf{q} / 4m^2, \\ (b) &= (c) \\ &= -f^4 \tau_r \tau_s (\pi^2 / 2mi) \boldsymbol{\sigma} \cdot \mathbf{p} \cdot \boldsymbol{\sigma} \cdot \mathbf{q} / 4m^2, \\ (d) &= -\frac{1}{3} f^4 [4\delta_{rs} - \tau_r \tau_s] (\pi^2 / 2mi) \mathbf{p} \cdot \mathbf{q} / 4m^2. \end{aligned} \right\} \quad (3.4)$$

The renormalization of the vortex part, is done so that terms (b) and (c) contain no terms in $1/\omega$, and thus the coupling constant is determined by the coefficient of the neutron pole at $\omega=0$ in Born approximation. Adding the crossed graphs, we find

$$\begin{aligned} S_\alpha^{(2)} &= -(2\pi)^4 f^2 (p^2 / 4m^2 \omega i) n_\alpha \mathbf{P}_\alpha, \\ S_\alpha^{(4)} &= f^4 (\pi^2 / 2mi) (p^2 / 4m^2) N_\alpha \mathbf{P}_\alpha, \end{aligned} \quad (3.5)$$

where

$$n_\alpha = -8, -2, 4, \quad (3.6)$$

$$N_\alpha = -13, -7, -10, \quad (3.7)$$

for $\alpha=11, 13$ and 33 respectively.

As in I, the phase shifts are now given by

$$\lambda_\alpha p^3 \cot \delta_\alpha / \omega = 1 - (\omega / \omega_\alpha), \quad (3.8)$$

$$\lambda_\alpha = \frac{1}{3} (g^2 / 4\pi) n_\alpha, \quad (3.9)$$

$$\omega_\alpha = (4\pi^2 r_\alpha / mg^1), \quad (3.10)$$

where

$$\gamma_\alpha = n_\alpha / N_\alpha, \quad (3.11)$$

and g is the pseudo-vector coupling constant

$$g = (f / 2m). \quad (3.12)$$

Thus the method again leads to the Chew and Low (1956) effective range plot, and, although there is now only one free parameter, one can again fit the experimental data for the 33 phase with

$$\begin{aligned} (g^2 / 4\pi) \mu^2 &\cong 0.08, \\ \text{or } (f^2 / 4\pi) &\cong 16, \end{aligned} \quad (3.13)$$

in agreement with the photoproduction data.

As noted by Chew and Low, crossing symmetry requires that

$$\omega_{11}^{-1} : \omega_{13}^{-1} : \omega_{33}^{-1} = -1 + \frac{1}{4}x : -x : 1. \quad (3.14)$$

An Analysis of the Reactions Induced in Complex Nuclei by Nucleons with Energies between 10 and 20 MeV†

By G. BROWN and H. MUIRHEAD

Department of Natural Philosophy, University of Glasgow

[Received June 25, 1956 ; and in revised form November 9, 1956]

SUMMARY

Calculations have been made of the absolute values of the cross sections for processes of the type

${}_Z\text{N}^A(n, p\gamma)_{Z-1}\text{N}^{A-1}$, ${}_Z\text{N}^A(n, pn)_{Z-1}\text{N}^{A-1}$, ${}_Z\text{N}^A(n, n')_Z\text{N}^A$ and ${}_Z\text{N}^A(p, p')_Z\text{N}^A$, which have been induced by nucleons with energies between 10 and 20 mev.

It has been assumed that the target nucleus may be represented as a Fermi gas of nucleons, and that the nuclear processes proceed by direct interactions between the incident particle and the target nucleons, followed by the de-excitation of the nucleus ; the ejection of a particle can occur during either process.

Comparisons between the calculated and experimental data for the total cross sections, energy spectra and angular distributions of the emitted particles, indicate satisfactory overall agreement except for the process ${}_Z\text{N}^A(p, p')_Z\text{N}^A$.

Empirical evidence is cited, which indicates differences in the level densities of the excited states of even-even, even-odd and odd-odd nuclei.

§ 1. INTRODUCTION

FESHBACH *et al.* (1953) and subsequent workers (Culler *et al.* 1956, Woods and Saxon 1954) have shown that the magnitudes of the total and differential cross sections for reactions between nucleons and complex nuclei may be successfully calculated by using a weak coupling theory. In these calculations a complex potential of the form $V_0(1+i\zeta)$ was used to describe the interaction between the incident nucleon and the target nucleus.

Members of this laboratory (Morrison *et al.* 1955) and others (Lane and Wandel 1955, Clementel and Villi 1955) have shown that it is possible to predict the behaviour of ζ as a function of the energy of the incident particle, and also its absolute magnitude. In demonstrating this result it was assumed that the nucleus could be represented as a Fermi gas of nucleons, and that the incident particle interacts individually with the

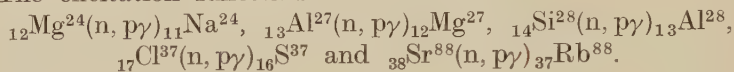
† Communicated by Professor P. I. Dee, F.R.S.

bound nucleons of the target with a cross section which differs only from that for free particles through the restrictions of the Pauli Exclusion Principle.

In this paper we have extended this approach to the description of the nucleon-nuclear interaction to the calculation of the cross sections for the processes listed below ; in all of them previous workers have shown that the normal statistical theory of the decay of the compound nucleus is inadequate for explaining the experimental observations.

(1) ${}_Z\text{N}^A(n, p)_{Z-1}\text{N}$ for neutrons with an energy of 14.5 Mev.

(2) The excitation functions for the reactions :



(3) The angular distribution of the neutrons emitted with energies between 4 and 12 Mev, following the interaction of neutrons of 14 Mev with bismuth.

(4) The energy spectrum of the protons emitted at 60° and 150° from iron, silver and platinum when bombarded by protons of 18 Mev.

§ 2. DISCUSSION OF PROCEDURE

We have assumed that the target nucleus may be represented as a Fermi gas of nucleons. Whilst this choice was primarily dictated by the need for a mathematical approach which would be both simple and consistent, there appears to be some justification for considering it as an approximate physical description of the normal and excited states of a heavy nucleus. Thus an assembly of non-interacting particles should approximate reasonably to the requirements of the shell model of the nucleus, in which definite physical states must exist for considerable periods of nuclear time. In addition, Lang and Le Couteur (1954) have used the model of a Fermi gas to calculate the level densities of excited states of nuclei ; their results are in good agreement with the experimental data.

We have assumed that a nuclear reaction proceeds in three stages, (i) an initial collision between the incident nucleon and one of those contained in the target nucleus followed by (ii) the formation of an excited nucleus which subsequently decays (iii). The nuclear excitation, according to our model, is concentrated initially in one or more nucleons moving inside the nucleus at energies above the Fermi maximum but too low to escape from the nucleus. Degradation of this energy in further collisions can occur, and the nucleus can pass through several modes of excitation before stage (iii) occurs. The emission of nucleons by process (i) occurs in a period of about 10^{-23} sec, whilst by (iii) it occurs in times which are many orders of magnitude longer than this period. Thus process (iii) will be essentially independent of (ii), and we have assumed that the

statistical arguments of Weisskopf and Ewing (1940) may be applied to the nuclear decay, whilst the direct collision process is examined separately. Our procedure is discussed in detail in §§ 3 and 4.

§ 3. THE CROSS SECTIONS FOR EMISSION OF NUCLEONS BY DIRECT COLLISIONS

3.1. Total Cross Sections for the Process ${}_Z\text{N}^A(n, p)_{Z-1}\text{N}^A$

Culler *et al.* (1956) have shown that the experimental data on the magnitude of the cross section for the interaction of neutrons of 14 mev with nuclei, may be satisfactorily reproduced by solving the Schrödinger equation for a complex potential well of the form $V=42(1+0.25i)$. As stated in § 1, imaginary potentials of this magnitude may be predicted by a Fermi gas model. Exact reproduction of the experimental data is difficult to achieve, since the theoretical results depend partly on the assumed shape of the potential at the surface of the nucleus. For convenience, therefore, we will use for the interaction cross sections σ_1 , of the incident neutrons the measured values of Amaldi *et al.* (1946) and Phillips *et al.* (1952) at 14 mev.

We have assumed that this interaction occurs through a collision with either a neutron or proton in the target nucleus. Assuming that the neutrons and protons in the nucleus can be represented as two independent Fermi gases, we may write the cross section, $(d\sigma/d\epsilon)_N$ for the production of a proton with energy ϵ in the target nucleus as

$$\left(\frac{d\sigma}{d\epsilon}\right)_N = \sigma_1 \frac{\rho_p(d\sigma/d\epsilon)}{[\alpha X(P_1)]_{np}\rho_p + [\alpha X(P_1)]_{nn}\rho_n} \quad \dots \quad (1)$$

where $X(P_1)$ = the cross section for a collision of a neutron of momentum P_1 with a free nucleon, $P_1 = \sqrt{2M(V_0 + E_1)}$, M = mass of nucleon, V_0 = depth of nuclear potential well, E_1 = energy of the incident neutron outside the nucleus, $\epsilon_1 = V_0 + E_1$, $d\sigma/d\epsilon$ = cross section for the production of a proton with energy ϵ in the collision between a single neutron and a proton, α = a factor which reduces the magnitude of $X(P_1)$ inside the nucleus through the operation of the Pauli Exclusion Principle and, ρ = the density of the nucleons inside the nucleus.

The subscripts n and p refer to neutrons and protons respectively: an expression for α will be given later in this section.

We have defined the depth of the nuclear potential well V_0 as the sum of the maximum Fermi energy ϵ_f for the neutrons in the target nucleus and the binding energy of the last nucleon in that nucleus. The magnitude of ϵ_f was calculated by assuming that the neutrons were contained within a sphere of radius $1.37 A^{1/3} 10^{-13}$ cm (A is the atomic weight of the nucleus). We have assumed that V_0 for the protons equals that of the neutrons, and that the maximum Fermi energy of the protons ϵ_p is given by the difference between V_0 and the binding energy of the last proton. The values for the binding energies were obtained from the tables of Feather (1953).

The expression for $d\sigma/d\epsilon$ in eqn. (1) may be written as

$$\begin{aligned} \frac{d\sigma}{d\epsilon} &= \frac{3MX(P_1)}{2\pi P_F^3} \int \frac{P_1^2}{|\mathbf{P}_1 - \mathbf{P}_2|^2} \frac{|\mathbf{P}_1 - \mathbf{P}_2|}{P_1} \frac{d\mathbf{P}_2}{|\mathbf{P}_1 - \mathbf{P}_2| |\mathbf{P}_1 + \mathbf{P}_2|} \\ &= \frac{3MX(P_1)}{\sqrt{(2)P_F^3}} \left[(P_1^2 + P_2^2)^{1/2} \tanh^{-1} \frac{2P_2 \sqrt{[2(P_1^2 + P_2^2)]}}{P_1^2 + 3P_2^2} \right. \\ &\quad \left. - 2\sqrt{(2)P_1} \tanh^{-1} \frac{P_2}{P_1} \right]_x^y \end{aligned} \quad (2)$$

where

$$y = \sqrt{(2M\epsilon_F)}, \quad x = \sqrt{[2M(\epsilon + \epsilon_F - \epsilon_1 - Q)]}.$$

In the above equations \mathbf{P}_2 represents the momentum of the struck proton (of energy ϵ_2). The cross section for scattering in the centre of momentum system of the two colliding particles has been assumed to be isotropic. Physically, this assumption is not correct, but the error introduced is negligible in this calculation†. In accord with experimental data, the cross section for the scattering of free neutrons and protons was assumed to vary inversely as the energy available in the centre of momentum system. In performing the integration the limits quoted above ensure that the Pauli Exclusion Principle is not violated. The symbol Q represents the normal definition of the term defining the release of energy in a nuclear process.

The term $\alpha X(P_1)$ of eqn. (1) may be obtained by performing the integration

$$\alpha X(P_1) = \int_{\epsilon_F}^{\epsilon_1 + Q} \left(\frac{d\sigma}{d\epsilon} \right) d\epsilon. \quad (3)$$

The final expression is unwieldy, but a numerically equivalent expression derived by an alternative method is given in eqn. (4).

$$\begin{aligned} \alpha X(P_1) &= \frac{X(P_1)}{2\sqrt{(2)P_F^3}} \\ &\times \left[(P_1^2 + P_2^2)^{1/2} (P_1^2 + P_2^2 - 6P_F^2 + 6MQ) \tanh^{-1} \frac{2P_2 \sqrt{[2(P_1^2 + P_2^2)]}}{P_1^2 + 3P_2^2} \right. \\ &\quad \left. + 4\sqrt{(2)P_1} (3P_F^2 - 3MQ - P_1^2) \tanh^{-1} \frac{P_2}{P_1} + 2\sqrt{(2)P_2} P_1^2 \right]_z \end{aligned}$$

where

$$z = \sqrt{[2M(2\epsilon_F - \epsilon_1 - Q)]}. \quad (4)$$

The energy of a proton which has escaped from the nucleus is given by $E = \epsilon - V_0$. The cross section $(d\sigma/dE)_{np}$, for the direct ejection of a proton with kinetic energy between E and $E + dE$ when a neutron enters a nucleus is given by

$$\left(\frac{d\sigma}{dE} \right)_{np} = \left(\frac{d\sigma}{d\epsilon} \right)_N \phi(E) \quad (5)$$

† A rough calculation indicated that the non-isotropy of neutron-proton scattering reduces $d\sigma/d\epsilon$ by about 20% in the energy region relevant to the present paper.

where $d(E)$ represents the probability of escape from the nucleus (see Appendix).

The total cross section $\sigma_n(\text{dir.})$, for the direct emission of protons from the nucleus as a result of the first collision of a neutron with a proton can be obtained by the numerical integration of eqn. (5).

$$\sigma_p(\text{dir.}) = \int_0^{E_1+Q} \left(\frac{d\sigma}{dE} \right)_{np} dE. \quad (6)$$

A rough numerical calculation showed that the probability for the direct emission of particles from second collisions is negligible, when the incident nucleon possesses an energy of less than 20 mev. The total cross section for the emission of neutrons by direct collisions $\sigma_n(\text{dir.})$ may also be calculated by the methods outlined above.

3.2. The Differential Cross Sections for Processes of the type

$${}_Z\text{N}^A(p, p'){}_Z\text{N}^A \text{ and } {}_Z\text{N}^A(n, n'){}_Z\text{N}^A$$

For convenience, we will consider the process ${}_Z\text{N}^A(p, p'){}_Z\text{N}^A$. A calculation of the differential cross section for the scattering of a nucleon by a Fermi gas of nucleons has been given by Hayakawa *et al.* (1955), and so will not be repeated here. The result of their elegant treatment may be written as

$$\frac{d^2\sigma}{d\epsilon dw} = \frac{3PF_1MX(P_1)}{4\pi qP_F^3} \log_e \frac{\sqrt{(\rho_2^2 + 2b\rho_2^2 + c) + \rho_2^2 + b}}{\sqrt{(\rho_1^2 + 2b\rho_1^2 + c) + \rho_1^2 + b}} \quad (7)$$

where $b = z_0^2 + q^2 - P^2$, $c = (P^2 + q^2 - z_0^2)^2$, $\rho_2^2 = P_F^2 - z_0^2$, $\rho_1^2 = P_F^2 - 2Q + P^2 - z_0^2 - P_1^2$, $z_0 = (1/2q)(P^2 + q^2 - P_1^2)$ and, $\mathbf{q} = \mathbf{P} - \mathbf{P}_1$.

The differential cross section $(d^2\sigma/d\epsilon dw)_N^\theta$, for the production of a proton with energy ϵ and in a direction θ inside the target nucleus may then be written as

$$\left(\frac{d^2\sigma}{d\epsilon dw} \right)_N^\theta = \frac{\sigma_I}{[{}_ZN(P_1)]_{pp}\rho_p + [{}_ZN(P_1)]_{pn}\rho_n} \left[2 \left(\frac{d^2\sigma}{d\epsilon dw} \right)_{pp} \rho_p + \left(\frac{d^2\sigma}{d\epsilon dw} \right)_{pn} \rho_n \right]. \quad (8)$$

The factor of 2 appears in the first term in the brackets since it represents the collision of identical particles.

§ 4. THE CROSS SECTION FOR THE EMISSION OF A PARTICLE BY THE DECAY OF A COMPOUND NUCLEUS

4.1. The Formation of a Compound Nucleus

Following the initial collision between the incident nucleon and a bound one, an excited nucleus is left: this nucleus may exist in various states of excitation.

† Equation (3.8) in the work of Hayakawa *et al.* (1955) is incorrect. Upon insertion of the correct expression the equations for b and c may be simplified to those given above. In addition we have allowed for the Q -value of a reaction.

When nucleon emission by direct collision occurs, the residual nucleus may have an energy of excitation which lies between 0 and E_1 . Nuclei in this state of excitation cannot contribute significantly to the processes which we wish to discuss, and so will be ignored.

When nucleon emission by direct collisions does not occur the nucleus is left with an excitation energy U , given by

$$U = E_1 + B,$$

where B is the binding energy of the incident nucleon in the compound nucleus. We have defined a cross section σ_c , for the formation of a nucleus with excitation energy U by

$$\sigma_c = \sigma_I - [\sigma_P(\text{dir.}) + \sigma_n(\text{dir.})]. \quad (9)$$

Thus σ_c/σ_I represents the probability that, subsequent to the initial collision, a compound nucleus will be formed with an excitation energy $(E_1 + B)$ and, momentarily, no particles with energy greater than V_0 .

4.2. The Decay of the Compound Nucleus

In calculating the relative probabilities for the various modes of decay of the excited nucleus we have assumed that the statistical theory of Weisskopf and Ewing (1940) is essentially correct. Thus the cross section σ_a (comp.), for the emission of a particle a , by the decay of the excited nucleus may be written as

$$\sigma_a(\text{comp.}) = \sigma_c \frac{\Gamma_a}{\sum_i \Gamma_i} \quad (10)$$

where Γ_a = partial width for the decay of the compound nucleus by emission of particle a , and Γ_i = partial width for the decay of the compound nucleus by emission of a particle i .

A convenient formula for the term Γ has been given by Le Couteur† (1950). We have assumed that, at all energies, the particles resulting from the decay process are emitted isotropically.

Recent comparisons (Paul and Clarke 1953, Forbes 1952, Cohen *et al.* 1954, Gugelot 1954, Graves and Rosen 1953) between the experimental data on the cross sections for the emission of charged particles and the predictions of the statistical theory have suggested that this theory is unsatisfactory. We believe that satisfactory comparisons have not been achieved through not taking into account the effect of direct collisions, and from a lack of suitable data on the level densities of the excited states of nuclei. The latter factor is of great importance, and will be considered separately in § 5.

† For the term representing the inverse cross section which appears in this formula we have used the data of Shapiro (1953), with $R = 1.5 A^{1/3} 10^{-13}$ cm, and of Beyster *et al.* (1955) at 4 mev. This may be done without considerable error since cross sections for the formation of a compound nucleus are roughly the same for both weak and strong coupling theories.

4.3. *The Level Densities of Excited Nuclei*

Recently, considerable experimental information has been obtained concerning the density ω , of levels in many nuclei at excitation energies of about 8 mev. This region of excitation energy is relevant to the present calculation, since that of the residual nucleus is in this energy range following the emission of a charged particle from the compound state.

Lang and Le Couteur (1954) have made an extensive theoretical study of the spacing of nuclear levels D (where $\omega D=1$) and have shown that application of the thermodynamic properties of a Fermi gas to the nucleons of a nucleus yields the following equation for the spacing of nuclear levels of zero spin D_0 in a nucleus of atomic weight A and excitation energy U .

$$D_0 = 0.11 A^2 (U+t)^2 \exp. - \left[2 \left(\frac{AU}{11} \right)^{1/2} + \frac{3}{32} (11U)^{2/3} \right] \quad (11)$$

where

$$t = \left(\frac{10.5U}{A} \right)^{1/2} - \frac{7.9}{A}.$$

The spacing of nuclear levels of spin I , D_I , was assumed to be given by

$$(2I+1) D_I = D_0. \quad (12)$$

In tables 1, 2 and 3 we compare the data on measured level spacings with the predictions of Lang and Le Couteur. The experimental data on the level spacings in light nuclei has been taken from the tables of Endt and Kluwyer (1954) and from Buechner *et al.* (1956), Paris *et al.* (1955) and Paul *et al.* (1956); that on heavy nuclei has been taken from the work of Harvey *et al.* (1955). An average quantum number of spin was assigned tentatively to each group of levels, the assignment being made either from information obtained in the individual experiments, or from reasonable assumptions concerning the magnitude of the spin of the initial and product nuclei involved in the individual reactions and the energy of the incident particles.

The agreement between the experimental and theoretical data in table 2 is remarkable, in view of the variation of level spacing by a factor of 10^4 . It is apparent from tables 1, 2 and 3 that there is a large difference between the level density of even-even nuclei and that of other nuclei: the existence of a difference between even-odd and odd-odd nuclei is not so certain. Taking an average of the final columns of the tables it is found that for nuclei of the same mass and excitation energy the average level densities are given by

$$\frac{\omega_{o-o}}{12} \sim \frac{\omega_{o-e}}{5} \sim \frac{\omega_{e-e}}{1} \quad (13)$$

These variations in the level densities have been used in the calculations on the decay of the compound nucleus. It is possible that, due to the lack of resolving power in the existing experimental techniques, some of the levels of excited nuclei have not been observed and, therefore, that the factors 12 and 5 could be higher.

§ 5. RESULTS

5.1. *The Cross Section for the process, ${}_Z\text{N}^A(\text{n,p})_{Z-1}\text{N}$, for Neutrons with an Energy of 14.5 mev*

We have been primarily interested in calculating the magnitudes of the cross sections for the process ${}_Z\text{N}^A(\text{n,p}\gamma)_{Z-1}\text{N}^A$ and comparing these values with those obtained by Paul and Clarke (1953) and Forbes (1952), using activation techniques. Therefore, in making comparisons with these experiments we have assumed that the permitted limits of energy for the emission of protons are $(E_1 + Q)$ and $(E_1 + q)$ where q represents the binding

Table 1. Odd-odd nuclei

Nucleus	Reaction	U in mev	Measured average level spacing in ev	Average I	$(2I+1)D_I$ in ev	Expt. Theory
${}_{11}\text{Na}^{24}$	(d,p)	3.5 (2.5-4.5)	1.5×10^5	2	7.5×10^5	0.4
${}_{13}\text{Al}^{26}$	(p, γ)	7.3 (7.0-7.6)	4×10^4	5/2	2.4×10^5	1.0
${}_{13}\text{Al}^{28}$	(d,p)	4.0 (2.25-5.85)	7×10^4	2	3.5×10^5	0.3
	(d,p)	7.0 (6.3-7.7)	5×10^4	3	3.5×10^5	1.5
${}_{15}\text{P}^{32}$	(d,p)	3.2 (2.2-4.2)	2×10^5	2	1.0×10^6	0.7
${}_{49}\text{In}^{114}$	Neutron Scattering	7.2	14 ± 2	9/2	$(1.4 \pm 0.2)10^2$	0.3
${}_{49}\text{In}^{116}$	„	6.6	14 ± 2	9/2	$(1.4 \pm 0.2)10^2$	0.2
${}_{55}\text{Cs}^{134}$	„	6.7	42 ± 5	7/2	$(3.4 \pm 0.4)10^2$	1.1
${}_{63}\text{Eu}^{152,4}$	„	5.7	2.2 ± 0.3	5/2	13.2 ± 1.8	0.03
${}_{65}\text{Tb}^{160}$	„	5.8	10 ± 1.0	3/2	40 ± 4	0.13
${}_{67}\text{Ho}^{166}$	„	5.7	12 ± 1.3	7/2	96 ± 10	0.4
${}_{69}\text{Tm}^{170}$	„	5.9	15 ± 2	1/2	30 ± 4	0.2
${}_{71}\text{Lu}^{176}$	„	6.0	7 ± 2	7/2	56 ± 16	0.6
${}_{73}\text{Ta}^{182}$	„	6.0	9 ± 1	7/2	72 ± 8	0.9

Table 2. Even-odd, odd-even nuclei

Nucleus	Reaction	U in mev	Measured average level spacing in ev	Average I	$(2I+1) D_I$ in ev	$\frac{\text{Expt.}}{\text{Theory}}$
$_{11}\text{Na}^{21}$	(p,p')	5 (3.5-6.5)	2.5×10^5	3/2	1.0×10^6	1.0
$_{11}\text{Na}^{23}$	(p, γ)	9.8 (9.3-10.3)	5×10^4	1	1.5×10^5	1.4
$_{12}\text{Mg}^{25}$	(d,p)	3.3 (2.0-4.6)	3×10^5	2	1.5×10^6	0.8
$_{13}\text{Al}^{25}$	(p,p')	4.1 (2.9-5.3)	3×10^5	2	1.5×10^6	1.3
$_{13}\text{Al}^{27}$	(p, γ)	9.0 (8.5-9.5)	7×10^4	3/2	2.8×10^5	2.8
$_{14}\text{Si}^{29}$	(d,p)	4.0 (2.0-6.0)	4×10^5	2	2.0×10^6	1.9
$_{14}\text{Si}^{31}$	(d,p)	3.3 (2.3-4.3)	4×10^5	2	2.0×10^6	1.4
$_{15}\text{P}^{31}$	(p, γ)	9.3 (9.0-9.6)	2.5×10^4	2	1.2×10^5	2.0
$_{16}\text{S}^{33}$	(d, α)	3.1 (2.0-4.2)	2×10^5	3/2	8×10^5	0.6
$_{20}\text{Ca}^{41}$	(d,p)	3.0 (1.95-3.95)	2.5×10^5	3/2	1.0×10^6	0.8
$_{42}\text{Mo}^{93, 5, 7, 9, 101}$	Neutron Scattering	6.9	$(5 \pm 1.5)10^2$	1/2	$(10 \pm 3)10^2$	0.5
$_{50}\text{Sn}^{113}$	„	8.0	$(1.5 \pm 0.8)10^2$	1/2	$(3 \pm 1.6)10^2$	1.2
$_{50}\text{Sn}^{117}$	„	7.3	$(1.5 \pm 0.7)10^2$	1/2	$(3 \pm 1.4)10^2$	0.7
$_{50}\text{Sn}^{119}$	„	6.6	$(2 \pm 1)10^2$	1/2	$(4 \pm 2)10^2$	0.5
$_{50}\text{Sn}^{121, 123, 125}$	„	6.1	$(5 \pm 2)10^2$	1/2	$(10 \pm 4)10^2$	0.9
$_{72}\text{Hf}^{179, 181}$	„	6.1	$(1 \pm 0.5)10^2$	1/2	$(2 \pm 1)10^2$	2.8
$_{92}\text{U}^{239}$	„	4.9	18 ± 2	1/2	36 ± 4	0.7

Table 3. Even-even nuclei

Nucleus	Reaction	U in mev	Measured average level spacing in ev	Average I	$(2I+1)D_I$ in ev	Expt. Theory
$^{12}\text{Mg}^{24}$	(p,p')	4.8 (4.1-5.5)	4×10^5	3	2.8×10^6	3
	(p, γ)	12.8 (12.0-13.6)	7×10^4	2	3.5×10^5	12
$^{12}\text{Mg}^{26}$	(d,p)	4.3 (3.0-5.6)	3×10^5	5/2	1.8×10^6	2
$^{14}\text{Si}^{28}$	(p, γ) (p,p')	12.0 (11.8-12.25)	5×10^4	5/2	3×10^5	13
$^{16}\text{Si}^{32}$	(p,p')	4.8 (3.8-5.8)	3×10^5	2	1.5×10^6	3
	(p, γ)	10.0 (9.2-10.9)	1.1×10^4	3/2	4.5×10^5	21
$^{18}\text{A}^{38}$	(p,n)	12.3 (11.8-12.7)	5×10^3	5/2	3×10^4	5.5
$^{42}\text{Mo}^{96}$	Neutron Scattering	9.2	$(3.7 \pm 1.2)10^2$	5/2	$(22 \pm 7)10^2$	8.5
$^{42}\text{Mo}^{98}$,,	8.3	$(3.7 \pm 1.2)10^2$	5/2	$(22 \pm 7)10^2$	4.5
$^{50}\text{Sn}^{118}$,,	9.3	$(1.2 \pm 0.3)10^2$	1/2	$(2.4 \pm 0.6)10^2$	5.3
$^{50}\text{Sn}^{120}$,,	8.6	$(3 \pm 1.4)10^2$	1/2	$(6 \pm 2.8)10^2$	7.7
$^{72}\text{Hf}^{178}$,,	7.6	5.6 ± 0.6	$\leq 3/2$	22 ± 2.4	2.3
$^{72}\text{Hf}^{180}$,,	7.4	8 ± 2	$\leq 3/2$	32 ± 8	2.8

The figures in brackets in the column for U indicate the limits of excitation energy over which the assessment of level spacing was made for light nuclei.

energy of the last proton in the target nucleus: this corresponds to assuming that the appropriate radioactive decay does not take place if, after the ejection of a proton, the nucleus is left with sufficient excitation energy to emit a neutron. The cross sections were obtained by numerical integration of eqns. (6) and (10) between these limits.

In addition we have calculated the total cross sections for the emission of protons, and compared these values with those obtained by Allan and

Table 4.

Element	Q mev	$\sigma(n,p\gamma)$ mb.					$\sigma(n,p\gamma) + \sigma(n,pn)$ mb.			
		σ_p (comp.)	σ_p (dir.)	σ_p (comp.) + σ_p (dir.)	Paul and Clarke	Forbes	σ_p (comp)	σ_p (dir.)	σ_p (comp.) + σ_p (dir.)	Experi- ment.
O ¹⁶	-9.4	15	5	20	49±25		25	15	40	
F ¹⁹	-3.7	15	25	40	135±45		45	75	120	
Na ²³	-3.4	15	30	45	34±15		40	90	130	
Mg ²⁴	-4.7	160	45	205	190±20		160	50	210	
Mg ²⁵	-2.9	60	60	120	45±18		60	75	135	
Al ²⁷	-1.9	25	40	65	52±10	80±5	75	100	175	140*
Si ²⁸	-3.8	215	45	260	220±50		230	50	280	
Si ²⁹	-3.0	45	55	100	100±30		45	60	105	
P ³¹	-0.7	30	35	65	64±10	90±10	105	105	210	
S ³²	-0.9	170	50	220	370±50		340	85	425	
S ³⁴	-4.3	70	30	100	85±45		110	45	155	
Cl ³⁷	-3.5	10	30	40	33±6		20	55	75	
K ⁴¹	-1.8	10	35	45	80±30		40	75	115	
Ti ⁴⁸	-3.1	100	30	130	93±30		115	35	150	
V ⁵¹	-1.4	10	30	40	27±4		30	55	85	
Cr ⁵²	-3.0	75	30	105	78±11		100	35	135	
Fe ⁵⁴	+0.3						540	55	595	580*
Fe ⁵⁶	-2.9	60	30	90	97±12	124±12	80	30	110	190*
Ni ⁵⁸	+0.6						470	60	530	530*
Ni ⁶⁰	-2.0						115	30	145	300*
Ni ⁶¹	-0.5	30	45	75	182±30		30	45	75	
Cu ⁶³	+0.7						80	65	145	250*
Cu ⁶⁵	-1.3	5	30	35		19±4	15	45	60	<80*
Zn ⁶⁴	+0.2	110	45	155	386±60		360	55	415	590†
Zn ⁶⁶	-1.9	45	30	75	100±17		95	35	130	
Ga ⁶⁹	-0.1	5	25	30	24±18		30	55	85	
Ge ⁷⁰	-1.0	60	30	90	130±65		135	35	170	
Ge ⁷²	-3.2	10	20	30	65±30		20	20	40	
Ge ⁷³	-0.6	6	30	36	137±68		20	40	60	
As ⁷⁵	-0.4	3	30	33	12±2		15	45	60	
Se ⁷⁷	0.0	5	20	25	45±23		25	25	50	
Sr ⁸⁸	-4.4	2	9	11	18±3		3	9	12	
Zr ⁹⁰	-1.4	20	20	40	250±100		30	25	55	
Zr ⁹⁴	-4.6	0.3	6	6	10±5		1	9	10	
Mo ⁹⁷	-1.3	2	20	22	108±54		3	21	24	
Ru ¹⁰¹	-0.7	3	22	25	2±1		4	21	25	
Pd ¹⁰⁴	-1.5	6	17	23	132±66		10	20	30	
Pd ¹⁰⁶	+0.2	4	25	29	740±520		6	24	30	10†
I ¹²⁷	0.0	1	16	17	230±140		2	16	18	
Ba ¹³⁸	-4.1	0	3	3	6±2		0	3	3	
La ¹³⁹	-1.5	0	9	9	6±2.5		0	9	9	
Tl ²⁰⁵	-1.0	0	3	3	3±1.5		0	3	3	
Pb ²⁰⁸	-4.2	0	0.3	0.3	1±1		0	0.3	0.3	

* Allan. † Armstrong and Rosen

The symbol (n,pn) indicates the emission of a proton followed by a neutron at a later period. The measurements of Allan and of Armstrong and Rosen cover the cross sections $\sigma(n,p\gamma)$, $\sigma(n,pn)$, $\sigma(n,pp)$ and $\sigma(n,np)$.

by Armstrong and Rosen (private communications), using nuclear emulsions. The results for these calculations are shown in table 4.

It is seen from the table that our calculations follow the trend of the experimental results. The large fluctuations in the calculated cross sections are produced by variations in both the Q -values and the level densities of excited nuclei. It should be noted that, in addition to the

fluctuations resulting from the even-even, even-odd and odd-odd characteristics of nuclei, deviations from the formula of Lang and Le Couteur would be expected to arise from the detailed structure of an individual nucleus. These fluctuations will affect the magnitude of $\sigma_p(\text{comp.})$.

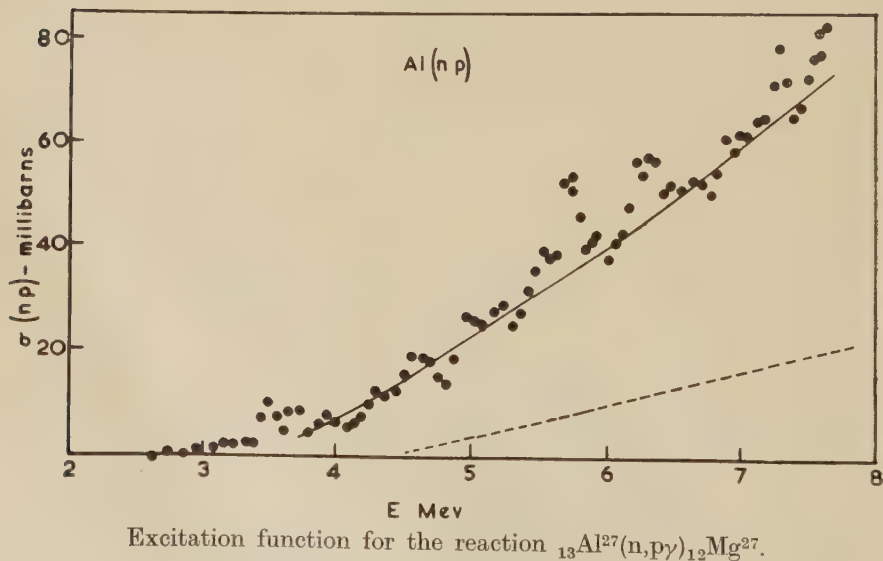
It can be seen that calculated cross sections for the heaviest nuclei are due almost entirely to the emission of protons by direct collisions. In particular, the cross section predicted for lead by the decay of the compound nucleus is too small by a factor 10^4 when compared with the experimental value.

5.2. *The Excitation Functions for the Reactions ${}_{12}\text{Mg}^{24}(\text{n}, \text{p}\gamma){}_{11}\text{Na}^{24}$, ${}_{13}\text{Al}^{27}(\text{n}, \text{p}\gamma){}_{12}\text{Mg}^{27}$, ${}_{14}\text{Si}^{28}(\text{n}, \text{p}\gamma){}_{13}\text{Al}^{28}$, ${}_{17}\text{Cl}^{37}(\text{n}, \text{p}\gamma){}_{16}\text{S}^{37}$ and ${}_{38}\text{Sr}^{88}(\text{n}, \text{p}\gamma){}_{37}\text{Rb}^{88}$*

The excitation functions for ${}_{12}\text{Mg}^{24}$, ${}_{14}\text{Si}^{28}$, ${}_{17}\text{Cl}^{37}$ and ${}_{38}\text{Sr}^{88}$ have been measured by Cohen and White (1956), and that for ${}_{13}\text{Al}^{27}$ has been measured by workers at Los Alamos (Hughes and Harvey 1955) by using activation techniques. We have calculated the cross section for the emission of a proton with energy lying between the limits (E_1+Q) and (E_1+q) by direct collisions and by the decay of a compound nucleus. Since the cross section for interaction of a neutron with the target nucleus does not vary appreciably with energy in the range 10–15 mev (Taylor *et al.* 1955) we have used the values of σ_i measured at 14 mev in calculating the excitation functions of ${}_{12}\text{Mg}^{24}$, ${}_{14}\text{Si}^{28}$, ${}_{17}\text{Cl}^{37}$ and ${}_{38}\text{Sr}^{88}$. The value of σ_i used in the calculation of the excitation function for ${}_{13}\text{Al}^{27}$ was 0.8 barns.

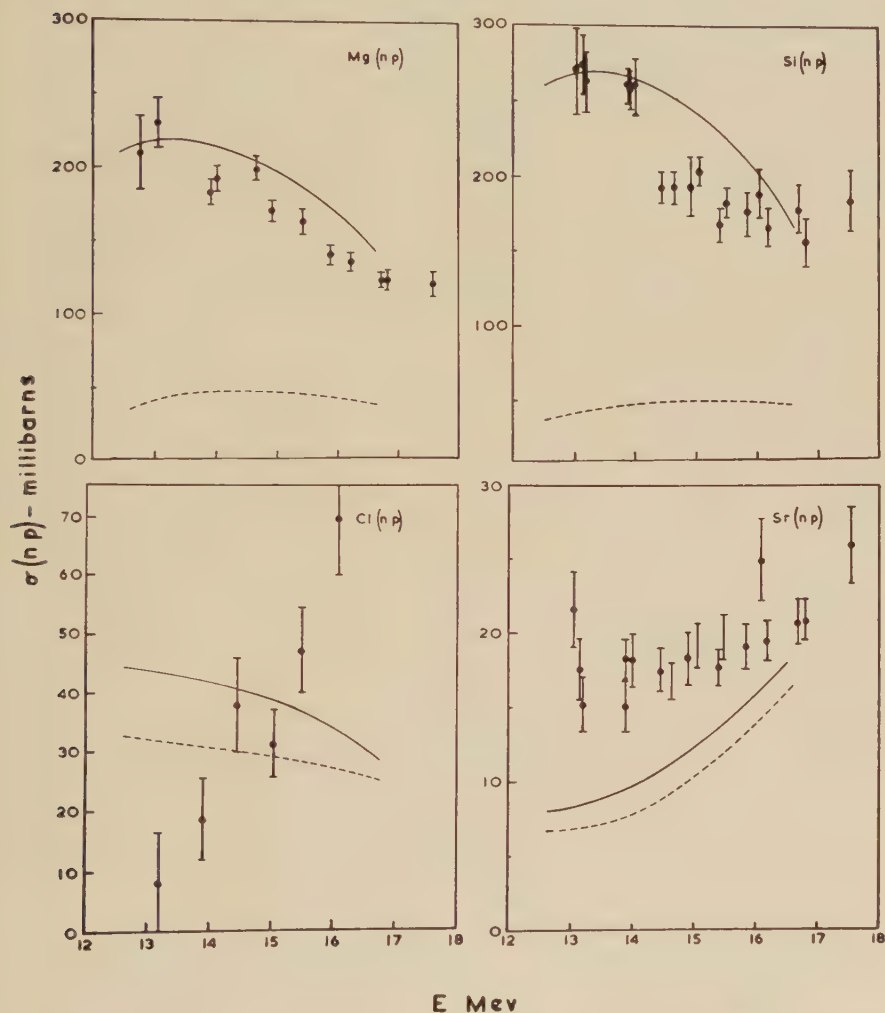
The excitation functions are shown in figs. 1 and 2.

Fig. 1



The agreement between the calculated and experimental values of the cross sections is satisfactory except for Cl^{37} ; we are unable to explain why the cross section for this nucleus should rise with increasing neutron energy.

Fig. 2



Excitation functions for the reactions $^{12}\text{Mg}^{24}(n, p\gamma)^{11}\text{Na}^{24}$; $^{14}\text{Si}^{28}(n, p\gamma)^{13}\text{Al}^{28}$; $^{17}\text{Cl}^{37}(n, p\gamma)^{16}\text{S}^{37}$ and $^{38}\text{Sr}^{88}(n, p\gamma)^{37}\text{Rb}^{88}$.
 — $\sigma_p(\text{comp.}) + \sigma_p(\text{dir.})$ - - - $\sigma_p(\text{dir.})$.

5.3. The Angular Distribution of the Neutrons Emitted with Energies between 4 and 12 MeV, following the Interaction of Neutrons of 14 MeV with Bismuth

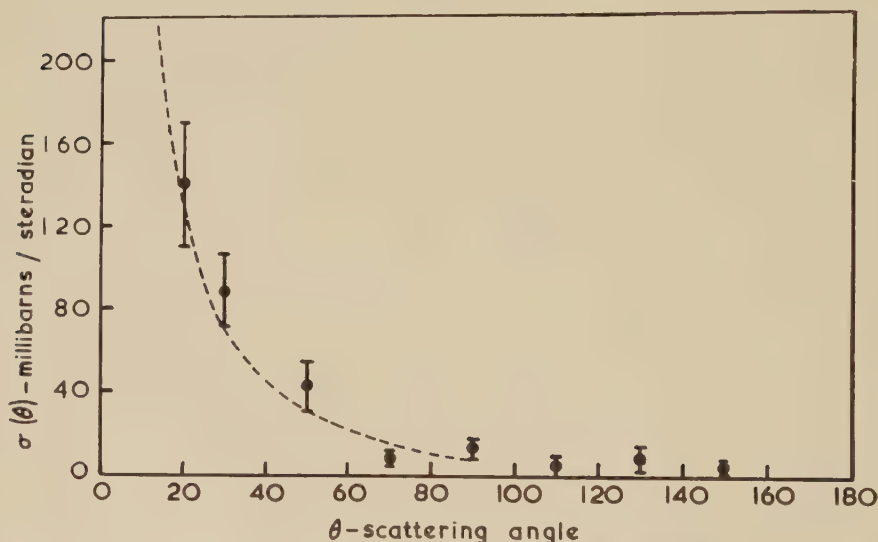
The experimental data with which we have made a comparison is that of Rosen and Stewart (1955).

The differential cross section for the production of a neutron, at different angles, with an energy ϵ by direct collisions has been calculated from eqn. (8) with suitable alteration of subscripts. For simplicity of calculation the parameters used were $\epsilon_F = \epsilon_f = 30$ mev and $V_0 = 36$ mev. It has been assumed (Appendix) that the differential cross section $(d^2\sigma/dE d\omega)_{nn}^0$, for emission of a neutron of energy E at an angle θ to the direction of the incident neutron is given by

$$\left(\frac{d^2\sigma}{dE d\omega}\right)_{nn}^0 = \left(\frac{d^2\sigma}{d\epsilon d\omega}\right)_N^0 \exp - \left[\frac{0.75R}{\lambda(\epsilon)} \right] \quad . \quad . \quad . \quad (14)$$

where $\lambda(\epsilon)$ = the mean free path of a neutron of energy in nuclear matter, and R = the nuclear radius.

Fig. 3



Angular distribution of the neutrons emitted from bismuth with energies between 4 and 12 mev.

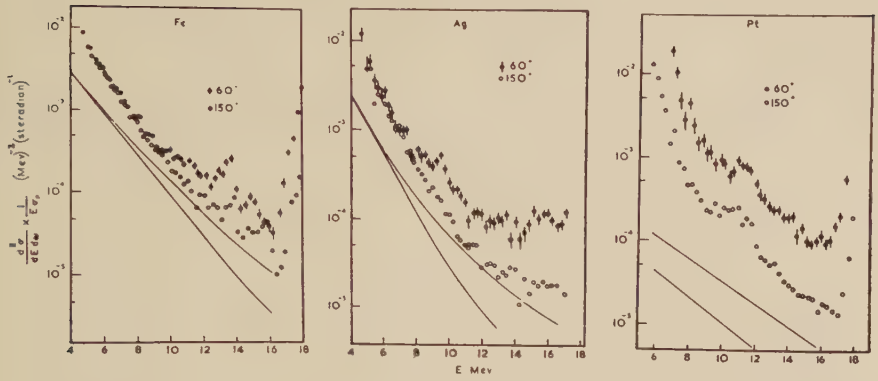
The angular distribution of the neutrons with energies between 4 and 12 mev was obtained by the numerical integration of eqn. 14. The cross section for the emission of neutrons with an energy greater than 4 mev by the decay of a compound nucleus was found to be negligible.

In fig. 3 a comparison is made between the calculated and experimental data.

5.4. *The Energy Spectrum of the Protons emitted at 60° and 150° from Iron, Silver and Platinum when Bombarded by 18 Mev Protons*

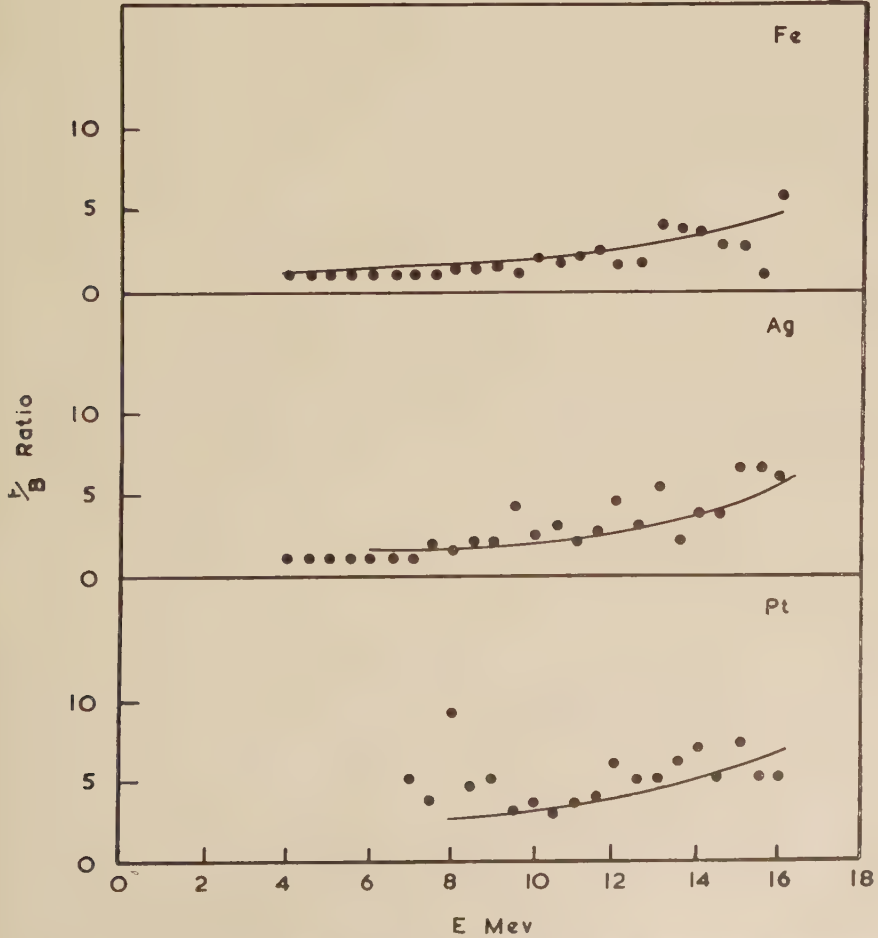
The magnitude of the term σ_1 appearing in eqn. (8) is not satisfactorily known for protons with an energy of 18 mev. We have employed values

Fig. 4



Energy spectra of the protons inelastically scattered at 60° and 150° , from iron, silver and platinum.

Fig. 5



Ratio of the cross sections at 60° and 150° for protons inelastically scattered from iron, silver and platinum.

extrapolated from the tables of Shapiro (1953). For simplicity of calculation the Fermi gas parameters used were $\epsilon_F = \epsilon_f = 30$ mev and $V_0 = 38$ mev. Rough allowance was made for the effects of multiple reflection by the Coulomb barrier.

The differential cross section for the emission of a proton of energy E by the decay of a compound nucleus has also been calculated. The sum of this cross section and that for emission of protons produced by direct collisions is shown for iron, silver and platinum in fig. 4. For platinum σ_p (comp.) is virtually zero.

It can be seen that the comparison becomes progressively worse with increasing atomic weight; this might be due in part to uncertainties in the magnitude of the penetrabilities of the coulomb barrier, but it should be pointed out that, because of this barrier, surface interactions could be more important for reactions with protons than for those involving only neutrons. The ratio of the cross sections for emission of protons at 60° and 150° is less sensitive to the penetrability: these ratios are displayed in fig. 5.

§ 6. DISCUSSION

It has been found that the nuclear reactions induced in heavy nuclei, by nucleons with energies greater than 100 mev, may be successfully described by a mechanical model which assumes the production of a nucleon cascade followed by the decay of an excited residual nucleus (Bernadini *et al.* 1952, Goldberger 1948, Morrison *et al.* 1953). The work described in this paper employs a basically similar method, and yields surprisingly satisfactory results at an energy, for the primary nucleon, at which a more formal theoretical treatment might be expected to be necessary.

It would be of interest to examine the region of validity of this model. In particular an inspection of the results quoted in table 4 would indicate that the angular distributions are strongly dependent on the nature of the target nucleus for the protons emitted in (n,p) reactions, since they will be determined by that relative strengths of the direct and compound processes; whilst for nuclei with atomic weight greater than 100 the angular distributions of high energy neutrons from (n,n) reactions should always be of the form shown in fig. 3.

ACKNOWLEDGMENTS

The authors wish to express their thanks to Professors P. I. Dee, F.R.S. and J. C. Gunn for their interest and encouragement during the course of this work; they also wish to express their gratitude to Professor K. J. Le Couteur, Drs. E. Laing, and G. Moorhouse for helpful and stimulating discussions. We are indebted to Drs. D. L. Allan, L. Armstrong and L. Rosen, and H. G. Blosser for communicating their results prior to publication, and to Dr. P. C. Gugelot for additional information.

APPENDIX

The Probability of Escape from a Nucleus, for Particles Produced in Direct Collisions

Assuming that the initial collision can occur throughout the nuclear volume, it can be shown that the average distance a particle must travel to reach the surface is about $0.75R$, in a nucleus of radius R .

Thus the probability that a nucleon, of energy ϵ , may reach the surface of the nucleus and escape is given by the expression

$$p = P \exp - \left[\frac{0.75R}{\lambda(\epsilon)} \right]$$

where $\lambda(\epsilon)$ = mean free path of a nucleon of energy ϵ in the nucleus, and P = the probability that the particle crosses the nuclear boundary. We have assumed that $P=1$ for neutrons, $=\sigma_p/\sigma_n$ for protons, where σ_p and σ_n represent the cross sections for the interaction of protons and neutrons respectively with nuclei. Values of σ_p were taken from the tables of Shapiro (1953). Since the values of σ_n change very slowly with energy in the region relevant to the present calculations, we have used the data obtained by Beyster *et al.* (1955) for neutrons with an energy of 4 mev.

Since P is less than unity and the mean free path, $\lambda(\epsilon)$, of the proton in nuclear matter is comparable with the dimensions of the nucleus, protons may emerge after more than one traversal of the nucleus following reflection at the nuclear boundary. Thus we may write the total probability for the escape of the protons as

$$\begin{aligned} \phi(E) &\sim p + px + px^2 + px^3 + \dots \\ &= \frac{p}{1-x} \end{aligned}$$

where $x = (1-P) \exp - [1.33R/\lambda(\epsilon)]$.

The term $1.33R$ represents the average distance the proton traverses in crossing the nucleus. The term x has negligible effect at high energies but can increase the emission of protons by about 40% at energies of about 5 mev for nuclei of $A \sim 50$.

REFERENCES

- AMALDI, E., BOCCIARELLI, D., CACCIAPUTO, C., and TRABACCHI, G., 1946, *Nuovo Cimento*, **3**, 203.
 BERNADINI, G., BOOTH, E. T., and LINDENBAUM, S. J., 1952, *Phys. Rev.*, **88**, 1017.
 BEYSTER, J. R., HENKEL, R. L., and NOBLES, R. A., 1955, *Phys. Rev.*, **97**, 563.
 BUECHNER, W. W., MAZURI, M., and SPERDUTO, A., 1956, *Phys. Rev.*, **101**, 188.
 COHEN, B. L., NEWMAN, E., CHARPIE, R. A., and HANDLEY, T. H., 1954, *Phys. Rev.*, **94**, 620.
 COHEN, A. V., and WHITE, P. H., 1956, *Nuclear Physics*, **1**, 73.
 CLEMENTEL, E., and VILLI, C., 1955, *Nuovo Cimento*, **11**, 176.
 CULLER, G., FERNBACH, S., and SHERMAN, N., 1956, *Phys. Rev.*, **101**, 1047.
 ENDT, P. M., and KLUYVER, J. C., 1954, *Rev. Mod. Phys.*, **26**, 95.

- FEATHER, N., 1953, *Advance Phys.*, **2**, 141.
FESHBACH, H., PORTER, C., and WEISSKOPF, V. F., 1953, *Phys. Rev.*, **90**, 166.
FORBES, S. G., 1952, *Phys. Rev.*, **88**, 1309.
GOLDBERGER, M. L., 1948, *Phys. Rev.*, **74**, 1269.
GRAVES, E. R., and ROSEN, L., 1953, *Phys. Rev.*, **89**, 343.
GUGELOT, P. C., 1954, *Phys. Rev.*, **93**, 425.
HARVEY, J. A., HUGHES, D. J., CARTER, R. S., and PILCHER, V. E., 1955, *Phys. Rev.*, **99**, 10.
HAYAKAWA, S., KAWAI, M., and KIKUCHI, K., 1955, *Prog. of Theor. Phys.*, **13**, 415.
HUGHES, D. J., and HARVEY, J. A., 1955, *Neutron Cross-Sections* (New York : McGraw-Hill).
LANE, A. M., and WANDEL, C. F., 1955, *Phys. Rev.*, **98**, 1524.
LANG, J. M. B., and LE COUTEUR, K. J., 1954, *Proc. Phys. Soc. A*, **67**, 586.
LE COUTEUR, K. J., 1950, *Proc. Phys. Soc. A*, **63**, 259.
MORRISON, G. C., MUIRHEAD, H., and MURDOCH, P. A. B., 1955, *Phil. Mag.*, **46**, 795.
MORRISON, G. C., MUIRHEAD, H., and ROSSER, W. G. V., 1953, *Phil. Mag.*, **44**, 1326.
PARIS, C. H., BUECHNER, W. W., and ENDT, P. M., 1955, *Phys. Rev.*, **100**, 1317.
PAUL, E. B., and CLARKE, R. L., 1953, *Canad. J. Phys.*, **31**, 267.
PAUL, E. B., BARTHOLEMEW, G. A., GOVE, H. E., and LITHERLAND, A. E., 1956, *Bull. Amer. Phys. Soc.*, **1**, 39.
PHILLIPS, D. D., DAVIS, R. W., and GRAVES, E. R., 1952, *Phys. Rev.*, **88**, 600.
ROSEN, L., and STEWART, L., 1955, *Phys. Rev.*, **99**, 1052.
SHAPIRO, M. M., 1953, *Phys. Rev.*, **90**, 171.
TAYLOR, H. L., LÖNSJÖ, O., and BONNER, T. W., 1955, *Phys. Rev.*, **100**, 174.
WEISSKOPF, V. F., and EWING, D. H., 1940, *Phys. Rev.*, **57**, 472.
WOODS, R. D., and SAXON, D. S., 1954, *Phys. Rev.*, **95**, 577.

The Electronic Structure of Palladium-Uranium Alloys

By J. A. CATTERALL

(Communication from the National Physical Laboratory)

[Received November 14, 1956]

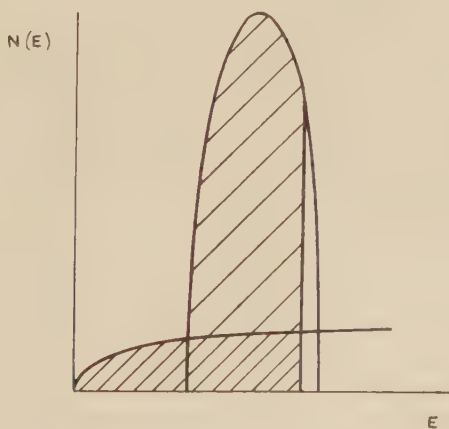
SUMMARY

The measured effects of uranium upon the paramagnetic susceptibility, electrical resistivity, thermoelectric power, and lattice parameter of palladium are discussed, and an interpretation of the results in terms of a solvent and solute band is suggested.

§ 1. INTRODUCTION

IN a recent paper dealing with the constitution of uranium-palladium alloys (Catterall *et al.* 1956) a considerable solid solubility of uranium in palladium is reported. Measurement of the effect of dissolved uranium upon certain of the physical properties of palladium suggested a means of

Fig. 1



Density of states of palladium.

estimating the valency of uranium in the alloys, and the variation with composition of the lattice parameter, paramagnetic susceptibility, electrical resistivity, and thermoelectric power of the solid solution alloys are dealt with here. A comparison is also made, where possible, between the effects of uranium and silver on these physical properties, and an interpretation in terms of a solvent and solute band is suggested.

In the solid state the electronic structure of palladium is considered to resemble that of nickel, but with 4d and 5s levels instead of 3d and 4s. In this model a long, low parabolic band contains the electrons of mainly 5s-type, while a high, narrow inverted band, also parabolic, contains the electrons of mainly 4d-type. The relative position of these two bands is shown in fig. 1. From a consideration of the paramagnetic susceptibility of palladium, and that of its alloys with the noble metals, hydrogen and nickel, Wohlfarth (1948) concludes that there are 0.6 holes per atom remaining in the 4d band, and this figure is confirmed by Hoare *et al.* (1953) from the determination of the susceptibility and electronic specific heat of palladium-silver alloys. The latter workers also deduce a form for the shape of the head of the band. The relatively high susceptibility, electronic specific heat and electrical resistance of palladium are attributed to the unfilled d-band, while the s-band is considered to be responsible for conduction and cohesion.

The band structure of uranium is not yet known, but in the free atom the outer electrons exist either in the states $(7s)^2(6d)^1(5f)^3$ (Seaborg 1949) or in the states $(7s)^2(6d)^4$ (Dawson 1952).

§ 2. EXPERIMENTAL METHODS

In this section the methods are described for the determination of the lattice parameter, electrical resistance and thermoelectric power. The paramagnetic susceptibilities discussed later are the values obtained by Leach (1955).

The materials and methods used in the preparation of the alloys were the same as those of the constitutional investigation. The lattice parameters were determined at room temperature on quenched alloys by the powder method using a 9 cm Unicam camera and $\text{CoK}\alpha$ radiation. The filings were prepared from ingots homogenized at 970°C , and they were stress-relieved at the same temperature. The accuracy of the measurements, except for one point, is about $\pm 0.0004 \text{ \AA}$.

The difficulty of preparing the alloys in the form of wire necessitated a somewhat crude method for the determination of the thermoelectric power, and no great accuracy is claimed for these measurements, the error being of the order of ± 0.5 microvolts/degree. A copper tube was soldered at right angles to each end of an annealed specimen of approximate dimensions $3 \times 0.5 \times 0.5 \text{ cm}$, and steam was passed through one tube and water through the other. A platinum/platinum-rhodium thermocouple was attached to each end of the specimen in order to measure the temperatures, and the platinum wires were then used to measure the e.m.f. of the alloy against platinum. The whole assembly was enclosed in a heavily lagged wooden box. The equipment was calibrated against nickel, which also served to check the signs of the e.m.f.s.

The electrical resistances of annealed specimens in the form of strip approximately $8 \times 0.5 \times 0.1 \text{ cm}$ were measured at 20°C in the Electricity Division, National Physical Laboratory, and they are considered to be accurate to within $\pm 0.5\%$.

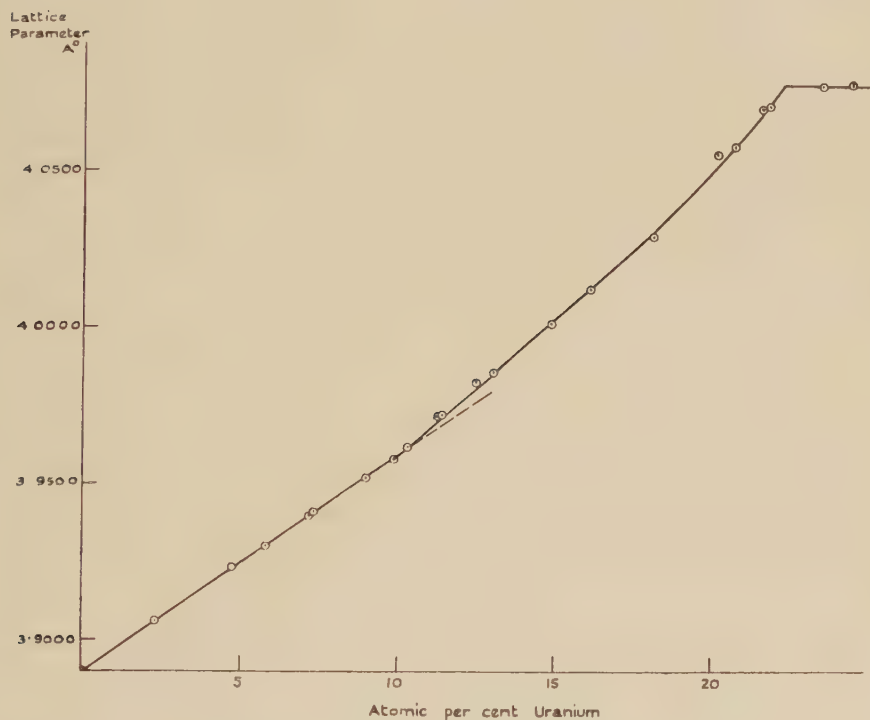
The chemical analysis of all the specimens was performed in the Metallurgy Division, N.P.L. All compositions are reported in atomic per cent.

§ 3. EXPERIMENTAL RESULTS

3.1. The Lattice-Parameter Composition Curve

The variation of lattice-parameter with composition is shown in fig. 2. Solution of the larger uranium atom expands the palladium lattice, whilst

Fig. 2



The lattice parameter-composition curve.

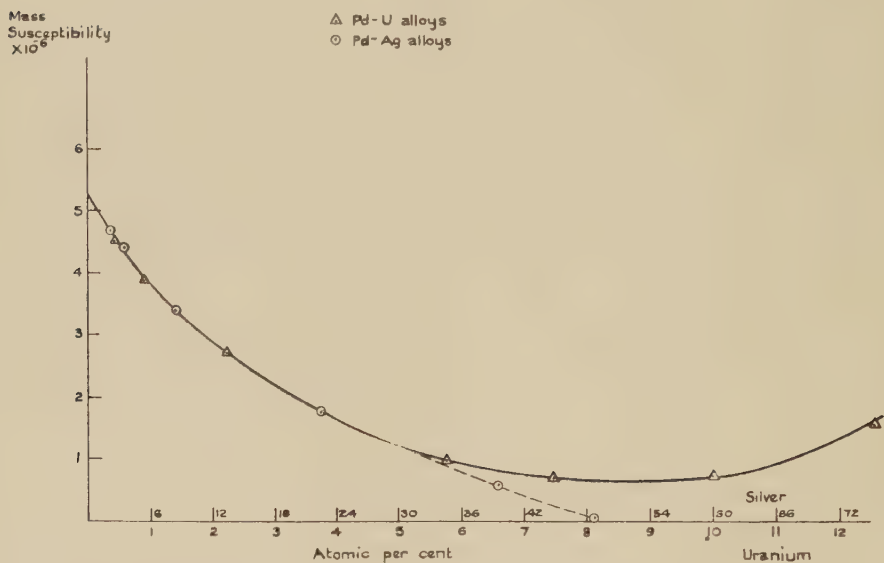
a marked change of slope in the direction of an additional expansion occurs at a composition between 10 and 10.5% uranium. The curve has been determined up to the solubility limit at 970°C of 22.3% uranium.

3.2. The Paramagnetic-Susceptibility Composition Curve

Leach's values at room temperature are shown in fig. 3, together with those of Hoare *et al.* for palladium-silver. In this figure, and also in figs. 4 and 5, the axis representing the percentage of uranium has been drawn six times the scale of the axis representing the percentage of silver. In this way if uranium were to dissolve with a valency of six and the changes in physical properties were attributable primarily to the influence

of the valency electrons of the added element the curves corresponding to the uranium and silver alloys of figs. 3, 4 and 5 should be superimposed. It is evident that at compositions up to 5% of uranium, uranium is six times as effective as silver in reducing the paramagnetism of palladium. At higher concentrations it becomes less effective, and the paramagnetism rises in alloys containing more than 9% uranium.

Fig. 3.



Paramagnetic susceptibility-composition curve at 20°C.

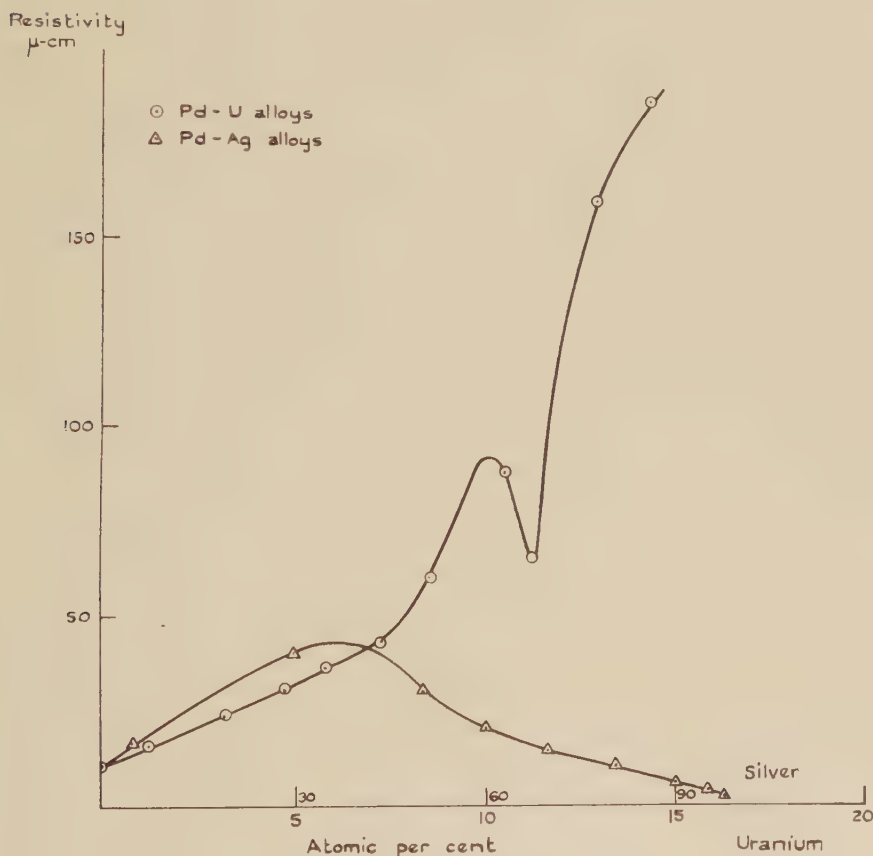
3.3. The Electrical-Resistivity Composition Curve

The variation of resistivity with composition is shown in fig. 4. A maximum occurs at 10% uranium and a minimum at 11.3%. Beyond this point the curve rises extremely steeply. The resistivity of palladium-silver alloys at 20°C determined by Kemp *et al.* (1956) is also shown in fig. 4. The shape of the uranium curve in the region 8–12% of solute depends upon only three alloys, and in order to avoid the possibility of a mistake the compositions of these three alloys (which contained 8.5, 10.5 and 11.3% uranium) were checked; and their resistances redetermined. In addition although the constitutional investigation has shown the absence of order-disorder transformations at temperatures down to 700°C, the alloy containing 10.5% uranium was re-annealed for 24 hours at 500°C. The resistance was unaltered after this treatment, and it may be concluded that such transformations have no influence on the shape of the resistivity curve.

3.4. The Thermoelectric-Power Composition Curve

The variation of the thermoelectric power against platinum with composition is shown in fig. 5. The values for palladium-silver alloys obtained by Giebel (1911), which are qualitatively confirmed by Taylor and Coles (1956), are also shown in this figure.

Fig. 4.

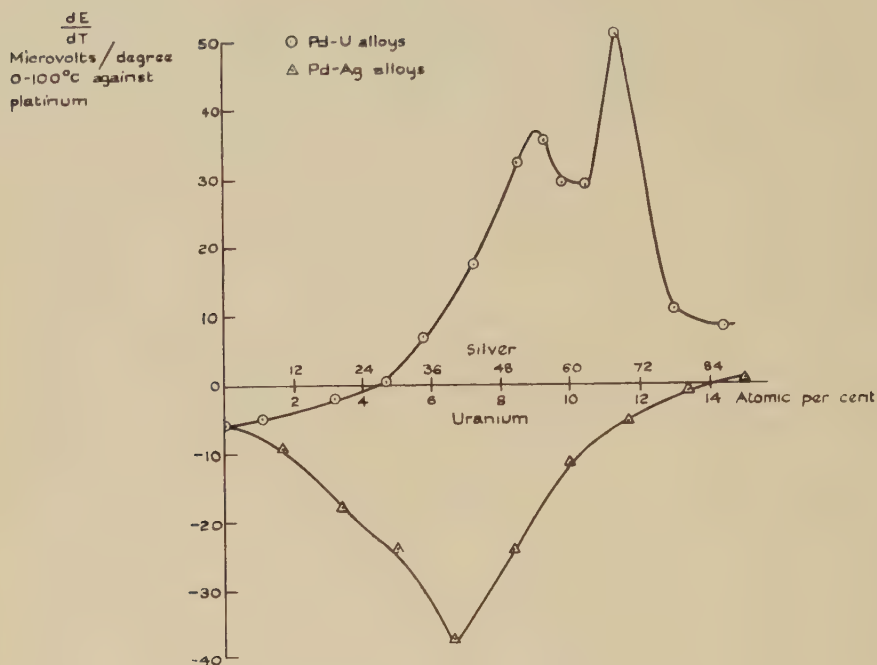


The resistivity-composition curve at 20°C.

§ 4. DISCUSSION

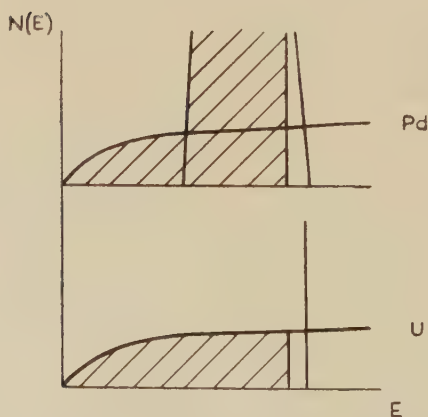
In calculating the heats of formation of binary alloys Varley (1954) has proposed a two-band model for the distribution of the energies of the electrons in a disordered solid solution. In this model the energies of the electrons in cells surrounding the solute and solvent atoms resemble those of the pure solute and solvent metals respectively. The energy of the system is then lowered by electron transfer between the cells if the electrons in one type of cell have higher energies than electrons in the other type. Varley has used this model to interpret the magnetic

Fig. 5



The thermoelectric power-composition curve.

Fig. 6



properties of copper-nickel alloys, in which he assumes that electrons are transferred from the copper cells to the nickel cells.

A similar model may be used to account for the behaviour of palladium-uranium alloys. The distribution of the energy levels in palladium metal is shown in fig. 1. The distribution of the levels in uranium metal is not yet known, but the x-ray absorption spectra obtained by Cauchois (1952)

indicate a high density of d- and f-states at the Fermi surface. It is not unreasonable therefore to assume that the energy band in uranium metal is derived from the 7s, 6d and 5f levels of the free atom, with the d- and f-levels forming a high narrow band overlapping a low band of mainly 7s character†.

From an examination of the susceptibility curves it is evident that at low concentrations uranium dissolves in palladium with a valency of six, since the paramagnetic susceptibility is reduced at six times the rate for silver. This shows that initial additions of uranium to palladium cause a large electron transfer from the uranium cells to the palladium cells, the electrons occupying the empty 4d-levels of palladium and consequently decreasing the paramagnetism. A continuation of this process with alloys of progressively increasing uranium content, however, will not explain the subsequent rise in paramagnetism. It is suggested, therefore, that the relative position of the solvent and solute bands shown in fig. 6 accounts for the observed effects. The occupied states shown as shaded areas in this figure correspond to the conditions existing in very dilute alloys. Further additions of uranium cause further electron transfer and also raise the Fermi surface. The system will eventually arrive at a stage where two opposing effects are taking place. These effects are (a) the occupation of the remaining empty d-levels in the palladium cells, which will cause the paramagnetism to fall, and (b) the occupation of the empty d- and f-levels in the uranium cells which will cause the paramagnetism to rise. A minimum in the curve of susceptibility against composition will therefore be expected.

The two-band model may also be used to interpret the resistivity against composition curve shown in fig. 4. The high electrical resistance of palladium has been shown (Mott and Jones 1936) to arise from the scattering of the conduction electrons into empty d-levels, which occurs in addition to the contribution from $s \rightarrow s$ scattering. The probability of scattering is proportional to the density of states at the Fermi surface. Initial additions of uranium to palladium cause the resistance of the alloys to rise as the foreign atoms introduce perturbations. This effect is opposed with increasing uranium content by a tendency for the resistance to fall as the empty d-levels of the palladium are filled, and a maximum similar to that found in palladium-silver alloys appears. The resistance then rises again as the alloys become still richer in the solute because of the presence of the empty d- and f-levels of the uranium in the neighbourhood of the Fermi surface.

The change of slope of the curve of lattice-parameter against composition which occurs at 10 atomic% uranium suggests a weakening of the cohesive forces existing in the alloy at the point where the palladium d-band is completely occupied. Until fairly recently the cohesion in the end members of the First Long Period was regarded as arising from the conduction electrons, but Friedel (1952) deduced a large Van der Waals

† Note added in proof.—See Friedel (1956).

force between the 3d-shells in copper, amounting to one-third of the binding energy. Mott (1953) has suggested that in nickel the Van der Waals contribution may exceed that from the conduction electrons and that its presence may account for the low number (0.6) of conduction electrons in both nickel and palladium. Friedel (1954) does not now consider the description of the d-shell interaction as a Van der Waals force to be reliable. However the change of slope in the palladium-uranium alloys appears to be connected with a variation in the rate of decrease of some form of d-shell interaction between the palladium atoms.

If the relative band positions shown in fig. 6 are correct they provide an explanation for the extensive solubility of uranium in palladium. The Fermi energy must rise relatively slowly per substituted solute atom in order that the structure should remain stable, and for this to occur a high $N(E)$ curve is necessary. For dilute alloys this condition is provided by the 4d-levels in the palladium cells, and for richer alloys by the d- and f-levels in the uranium cells.

ACKNOWLEDGMENTS

The work described above has been carried out in the Metallurgy Division of the National Physical Laboratory, and this paper is published by permission of the Atomic Energy Research Establishment and the Director of the National Physical Laboratory.

REFERENCES

- CATTERALL, J. A., GROGAN, J. D., and PLEASANCE, R. J., 1956, *J. Inst. Metals*, **1956**, **85**, 63.
 CAUCHOIS, Y., 1952, *J. Phys. Radium*, **13**, 113.
 DAWSON, J. K., 1952, *Nucleonics*, **10**, 39.
 FRIEDEL, J., 1952, *Proc. Phys. Soc. B*, **65**, 769; 1954, *Advances in Physics*, **3**, 446; 1956, *J. Phys. Chem. Solids*, **1**, 175.
 GIEBEL, W., 1911, *Z. anorg. Chem.*, **70**, 240.
 HOARE, F. E., MATTHEWS, J. C., and WALLING, J. C., 1953, *Proc. Roy. Soc. A*, **216**, 502.
 KEMP, W. R. G., KLEMENS, P. G., SREEDHAR, A. K., and WHITE, G. K., 1956, *Proc. Roy. Soc. A*, **233**, 480.
 LEACH, S. J., 1955, *Thesis*, Nottingham University.
 MOTT, N. F., 1953, *Phil. Mag.*, **44**, 187.
 MOTT, N. F., and JONES, H., 1936, *The Theory of the Properties of Metals and Alloys* (Oxford: University Press).
 SEABORG, G. T., 1949, *Nucleonics*, **5**, 16.
 TAYLOR, J. C., and COLES, B. R., 1956, *Phys. Rev.*, **102**, 27.
 VARLEY, J. H. O., 1954, *Phil. Mag.*, **45**, 887.
 WOHLFARTH, E. P., 1948, *Proc. Leeds Phil. Soc.*, **5**, 89.

The γ -Rays from the 8.06 MeV Level in $^{14}\text{N}^\dagger$

By C. BROUDE, L. L. GREEN, J. J. SINGH and J. C. WILLMOTT

Nuclear Physics Research Laboratory, University of Liverpool

[Received November 9, 1956]

§ 1. INTRODUCTION

THE γ -rays from the 8.06 mev level in ^{14}N which is formed when 550 kev protons are captured by ^{13}C have been examined by several workers and are of considerable interest. The resonance is an s-wave resonance of width 32.5 kev which is 12% of the Wigner s-wave limit, indicating that the level may be a single particle level (Clegg and Wilkinson 1953). The main E1 transitions from this level have been discussed by Lane and Radicati (1954) and by Wilkinson (1956). The level is known to be $1^-, T=1$ and the E1 transition to the 2.31 mev $0^+ T=1$ level is isotopic spin forbidden. Attempts to observe this transition by Clegg and Wilkinson (1953) resulted in an upper limit of 0.7% of the 8.06 mev transition. Wilkinson (1956) has recently pointed out that the 8.06 mev level may be one for which the isotopic spin impurity is particularly high. It is the purpose of this paper to report a measurement of the intensity of this unfavoured E1 transition and also other weak transitions. Similar measurements have recently been carried out at Saclay by Lehman *et al.* (1956) who obtained very similar experimental results.

§ 2. EXPERIMENTAL RESULTS

A thin target of ^{13}C was bombarded with 550 kev protons and the γ -rays observed at 0° and 90° to the proton beam. The γ -rays were observed in a 5 in. diameter by 6 in. thick NaI crystal mounted on a 5 in. diameter E.M.I. photomultiplier and the pulses recorded by a pulse height analyser. The irradiation of the crystal was restricted to the central 2 in. of the face by a lead collimator 4 in. thick. The methods for

γ -ray energy in mev	8.06	5.73	4.91	4.11	3.38	3.13	2.30	1.61
Relative Intensity	100	3.6	1.8	13.1	2.5	2.0	19.0	12.8

obtaining γ -ray intensities from complex spectra have been described in earlier papers. The spectra obtained at this resonance are shown in figs. 1 and 2. The γ -ray energies and relative intensities observed at this resonance are shown in the table. The relevant levels in ^{14}N and the transitions to which these γ -rays are ascribed are shown in fig. 3. The

† Communicated by Professor H. W. B. Skinner, F.R.S.

Fig. 1

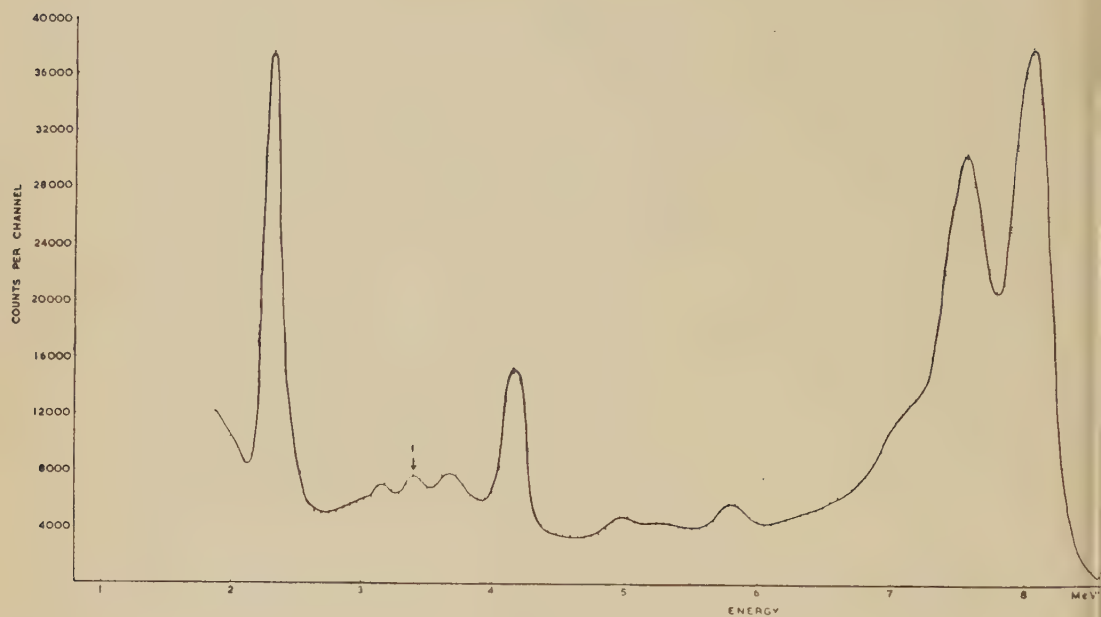
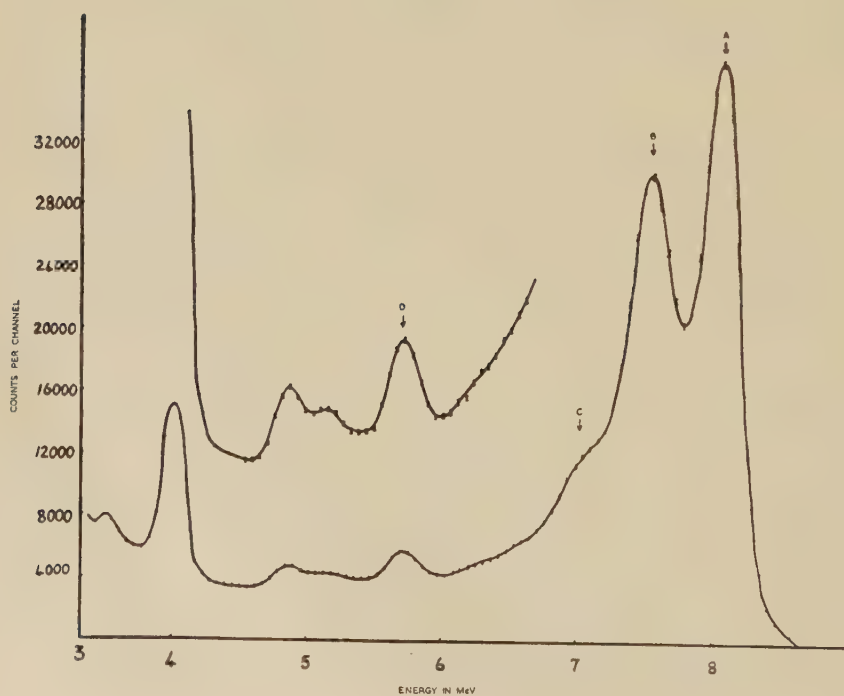


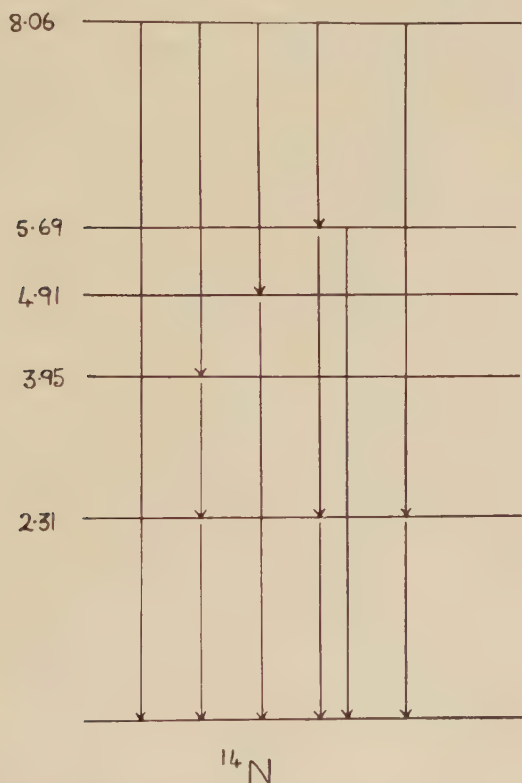
Fig. 2



intensities are in excellent agreement with this scheme except for an excess of the 2.30 mev γ -ray which is due to a contribution from the $^{12}\text{C}(\text{p}, \gamma)$ reaction.

The region above 4 mev is shown in detail in fig. 2. The peaks A, B and C are the three peaks due to the 8.06 mev ground state transition. The peak D is of energy 5.73 mev and is of the correct energy for the isotopic spin forbidden transition to the 2.31 mev level. Unfortunately there is also a level at 5.69 mev which could also give rise to a γ -ray of very nearly this energy. The decay of this state has been reported by Bent *et al.* (1955), and

Fig. 3



by Thomas and Lauritsen (1953). Both groups report that the 5.69 mev level branches to the ground state and the 2.31 mev state in the ratio of 30 to 70, the latter transition giving a γ -ray of 3.38 mev. Peak number 1 of fig. 1 is the total capture peak of a γ -ray of this energy and it has an intensity of 2.5% of the ground state transition. The corresponding intensity of the 5.69 mev γ -ray, using the above branching ratio, should thus be 1.1% of the ground state transition, whereas peak D of fig. 2 corresponds to a γ -ray of 3.6% of the intensity of the ground state transition. Hence if the previously reported branching ratio is correct,

Fig. 4

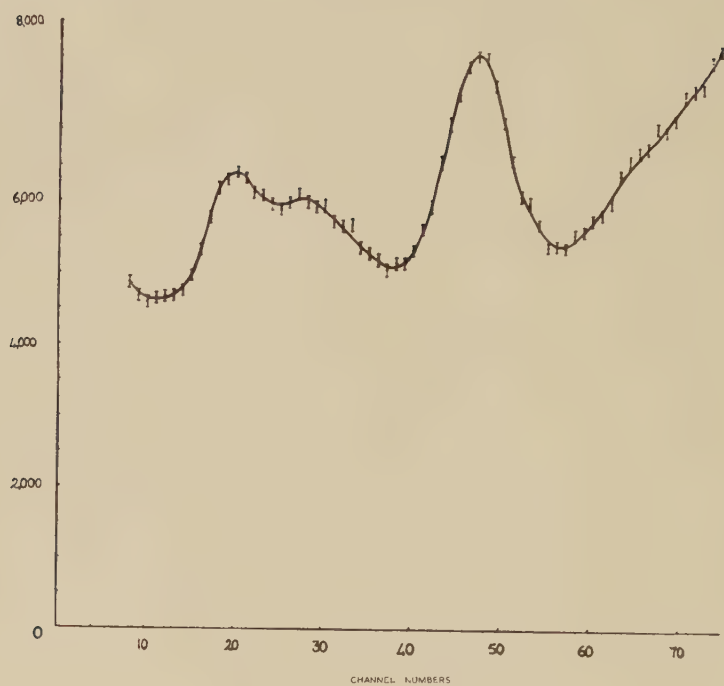
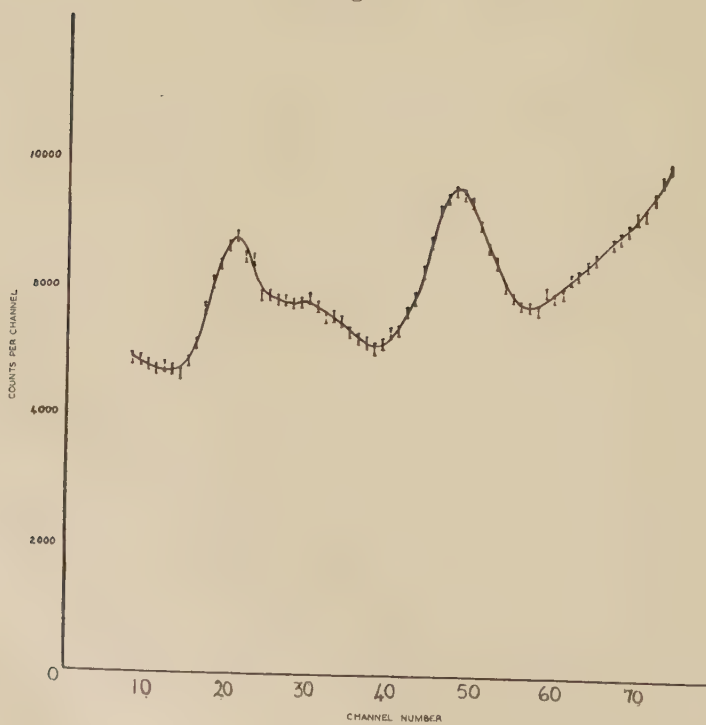


Fig. 5



two-thirds of the 5.73 mev peak is due to the isotopic spin forbidden transition to the 2.31 mev level. The broad width of this resonance enables us to check this interpretation. The 5.75 mev γ -ray is a primary γ -ray whose energy should change with bombarding energy, while the 5.69 mev γ -ray should be of constant energy. The region of the spectrum containing peak D of fig. 2 was observed under large energy expansion with the proton bombarding energy at 30 kv below the 550 kev resonant energy and again at 30 kv above. In the first case the γ -rays should be of energies 5.69 and 5.72 mev and in the latter case 5.69 mev and 5.78 mev. The two spectra are shown in figs. 4 and 5. The shift of the mean energy of the single escape peak leaves the 4.91 mev γ -ray more clearly resolved. The pulse height curves of γ -rays of 5.69 mev energy have been carefully determined. We have constructed the expected shapes for a composite peak of γ -rays of energy 5.69 and 5.72 mev and in the intensity ratios to be expected from the measured intensity of the 3.39 mev γ -ray and the branching ratio of Bent *et al.* (1955). This enables us to determine from fig. 4 the exact shape of the tail from the 8.06 mev γ -ray. If a tail of the same shape is subtracted from the pulse height distribution shown in fig. 5 the peak remaining is both broader and at a slightly higher energy, thus confirming that the 5.73 mev peak does contain a high proportion of a primary γ -ray.

§ 3. DISCUSSION

The intensity of the isotopic spin unfavoured transition to the 2.31 mev state is approximately four times the limit set by Clegg and Wilkinson on this transition and corresponds to a contamination of the 8.06 mev $T=1$ state with 8% of a $T=0$ state in intensity; in the notation of Radicatti (1954) $\alpha_1^2(0) \sim 0.08$. This assumes that the 2.31 mev state is a pure isotopic spin state: MacDonald (1956) has calculated that the impurity of the ^{14}N ground state should not be greater than 3×10^{-3} and the 2.31 mev state should not be very different from this. The 8% impurity is rather a high contamination for a state of this excitation and a possible reason for this has already been pointed out by Wilkinson. The width of the 8.06 mev level indicates that this state probably has a unique parent in the ground state of ^{13}C . The interaction between the 1p and 2s orbits is weak, as has been pointed out by Lane (1954). Thus the four states $0^-, T=1$; $1^-, T=1$; $0^-, T=0$; $1^-, T=0$, of which the 8.06 mev level is the $1^- T=1$ state, should not be far separated in energy. The $1^- T=0$ state should be very favourably situated for contaminating the 8.06 mev $1^- T=1$ state. The large impurity measured here lends some further support for Wilkinson's suggestion.

The 3.13 mev γ -ray corresponds to a transition from the resonance to the 4.91 mev state. This is known to be 0^- or 1^- , of which the 0^- is to be strongly favoured for reasons given by Ajzenberg and Lauritsen (1955). The matrix element $|M|^2$ for this transition is 0.3 Weisskopf M.I. units, indicating that it is probably M.I. in agreement with the 0^- assignment. As no change of configuration is allowed for an M.I. transition, this means

that the 4.91 mev level is probably the 0^- , $T=0$ member of the quartet of states based on the ground state of ^{13}C with an odd 2s particle. On this assumption we have calculated the transition probability for the 3.13 mev γ -ray, following Lane and Radicatti (1954), in jj-coupling, including the contributions from the 2s particle and the $p_{1/2}$ particle. In terms of their parameter A the results are as follows :

$$\begin{array}{cc} A_{\text{expt.}} & A_{\text{jj}} \\ 2.36 & 2.66 \end{array}$$

This M.I. transition probability is thus consistent with assumption that the 4.91 mev level is the 0^- , $T=0$ member of the quartet mentioned above. It may be noted that the 8.70 mev state in ^{14}N is also formed by s-wave proton capture in ^{13}C and has a large width. This state is known to be 0^- , $T=1$ and is probably a third member of this quartet and indicates a spacing between similar levels of different isotopic spin of this quartet of about 4 mev which is of the order of magnitude required to produce the measured isotopic spin impurity.

The other level fed from the 8.06 mev level is the 5.69 mev which is fed with about the same intensity as the 4.91 mev state. The spin and parity of this state are not known but the intensity of this γ -ray is correct for an M.I. transition which would be the case if this level were the fourth member of the quartet and 1^- , $T=0$. It may be noted that the decay of the 5.69 mev level is to the ground and first excited state and the intensities of these transitions are just those to be expected for a 1^- , $T=0$ state to the ground and first excited state with the $T=0$, 1^- state contaminated with 8% of $T=1$ in intensity.

ACKNOWLEDGMENTS

We should like to thank Professor H. W. B. Skinner for helpful discussions and Dr. R. Huby for some helpful comments on the paper of Lane and Radicatti (1954). One of us (J.J.S.) is indebted to the Punjab Government for leave of absence and another (C.B.) to D.S.I.R. for financial assistance. Our thanks are due to A.E.R.E. for preparing the separated ^{13}C target.

REFERENCES

- AJZENBERG, F., and LAURITSEN, T., 1955, *Rev. Mod. Phys.*, **27**, 77.
 BENT, R. D., BONNER, T. W., and SIPPEL, R. F., 1955, *Phys. Rev.*, **98**, 1237.
 CLEGG, A. B., and WILKINSON, D. H., 1953, *Phil. Mag.*, **44**, 1269.
 LANE, A. M., 1954, *A.E.R.E. Document*, T/R 1289.
 LANE, A. M., and RADICATTI, L. A., 1954, *Proc. Phys. Soc. A*, **67**, 167.
 LEHMAN, P., LEVEQUE, P., and PICK, R., 1956, *C.R. Acad. Sci.*, **243**, 743.
 MACDONALD, W. M., 1956, *Phys. Rev.*, **101**, 272.
 RADICATTI, L. A., 1954, *Proc. Phys. Soc. A*, **66**, 139.
 THOMAS, R. G., and LAURITSEN, T., 1953, *Phys. Rev.*, **88**, 969.
 WILKINSON, D. H., 1956, *Phil. Mag.*, **1**, 291.

The Effect of Added Titanium and Aluminium on the Magnetic Behaviour of α Ferric Oxide†

By G. HAIGH

Department of Physics, Imperial College of Science and Technology, London

[Received November 24, 1956]

ABSTRACT

An examination is made of the magnetic behaviour of hematite, α Fe_2O_3 , in the region of the antiferromagnetic transition temperature (-15°C) when titanium and aluminium are added in small amounts as an impurity. Contrary to an earlier observation by Morin, the transition is still observed in the synthesized material for relatively large impurity contents ($\sim 10\%$). The magnetic properties and behaviour of some naturally occurring hematites are compared with the synthesized materials, and are shown to be very structure sensitive. Thus the fact that this antiferromagnetic transition is not observed in natural hematite-bearing sandstones is thus probably not due to the presence of impurities but to some effect of crystal structure.

§ 1.1

IN 1952–53 a series of measurements were made by Clegg *et al.* (1954) of the remanent magnetization of Triassic sediments in England. Red rocks, characteristic of this geological period, were collected from widely separated sites and were found to have consistent polarizations, being magnetized in an approximately north-east to south-west direction with dips significantly less than that of the present earth's field, and with about half the specimens showing reverse polarization. The important palaeomagnetic implications of these results, both to continental movement and to the history of the earth's magnetic field, made it desirable to investigate the origin of the natural magnetism of these rocks.

An examination of the thermal properties of these rocks by Leng (1955) has revealed that the magnetic constituent is hematite, α Fe_2O_3 , but that it exists in two different forms. One is a detrital form consisting of black specks of material which x-ray powder photography revealed to be hematite, but which gave a Curie point in the region of 550 to 580°C , significantly lower than the Curie temperature of pure hematite, which is 685°C . The second is a red form appearing as a coating or surface deposit on the siliceous grains, or as a cement between these grains. The latter was found to be much less magnetic than the former, but with

† Communicated by Professor P. M. S. Blackett, F.R.S.

a much higher coercive force. It has been shown by Leng that it is this latter form which gives the sandstones their natural remanent magnetization. The Curie point of this second form is observed to be closely that of pure hematite.

Leng found no detectable difference between the magnetic properties of the normal and reversely magnetized specimens, thus strengthening the evidence for, but by no means finally proving the reality of repeated reversals of the earth's magnetic field. A general discussion of the argument has recently been given by Blackett (1956).

§ 1.2

For a further study of the possible origin of magnetic reversals in such rocks, a further knowledge of the magnetic properties of hematite is required, not only at normal temperatures, but throughout the possible range of terrestrial temperature.

Morin (1950) has observed the effects of cooling on the susceptibility of powder specimens of α Fe_2O_3 and, in particular, of specimens of α Fe_2O_3 with small quantities of titanium added. Morin found that the susceptibility of α Fe_2O_3 , and α Fe_2O_3 with small percentages of titanium added (up to 0.2% Ti) exhibited a marked transition at -15°C when cooled: the susceptibility decreasing rapidly at this temperature, to be about one-ninth of the room temperature susceptibility. This transition, however, was not observed when titanium was present to the extent of 1%.

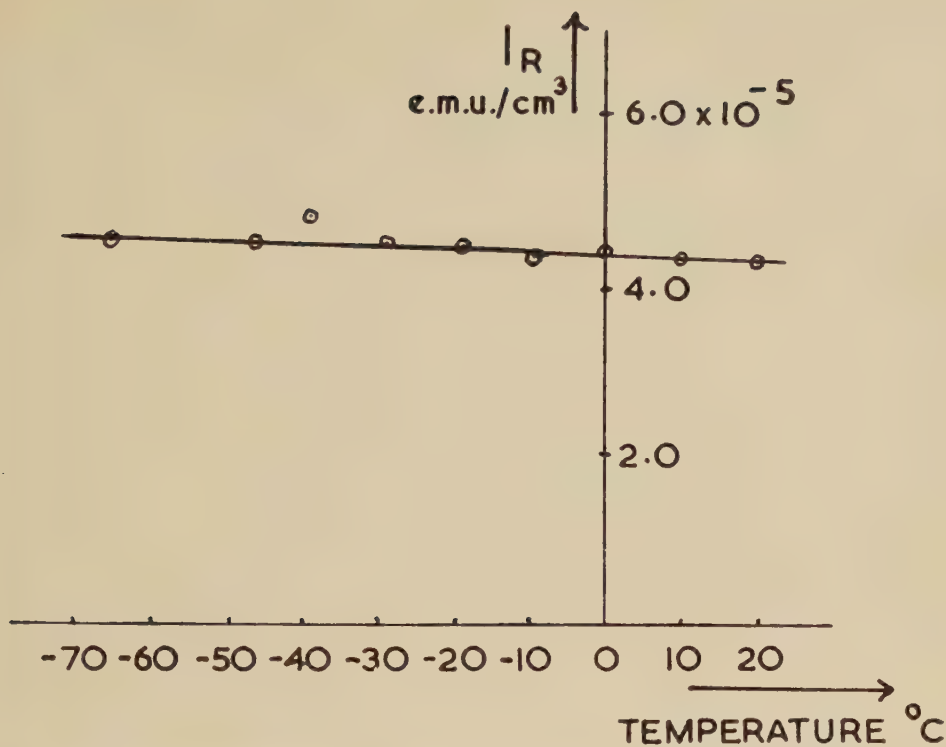
Similar observations were made by Pauthenet (1952, 1953) on a single crystal of natural rhombohedral α Fe_2O_3 from Elba; he also observed the transition occurring in the remanent magnetization, that is, when measured in zero field.

This phenomenon has been described theoretically by Neel (1952), wherein he attributes the transition to one of two parasitic ferromagnetisms which are present in hematite together with the fundamental antiferromagnetism. One of the parasitic ferromagnetisms he assumes to be closely tied to the direction of antiferromagnetism, which at room temperature and above is in the basal plane at right angles to the trigonal axis. On cooling below -15°C , the direction of antiferromagnetism turns into the trigonal axis taking a component of ferromagnetism with it. This change produces the decrease in remanent magnetization observed at this temperature.

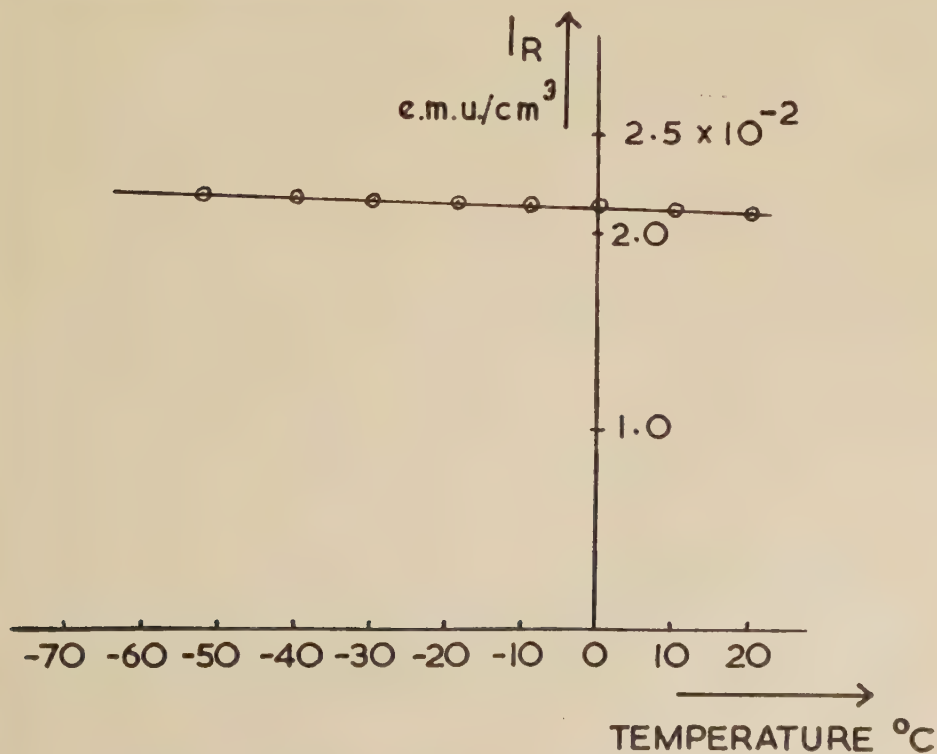
§ 2.1

In view of these results, it seemed likely that by observing the remanent magnetization of a natural or saturated British Triassic sandstone (a typical specimen contains some 5% of hematite (Blackett, p. 55)), as a function of temperature, a similar transition at or about -15°C should be found. Figures 1 (a) and 1 (b) show the remanent magnetization of rock specimens as measured by an astatic magnetometer, which

Fig. 1



(a) Natural magnetization of Triassic sandstone while being cooled to -70°C .

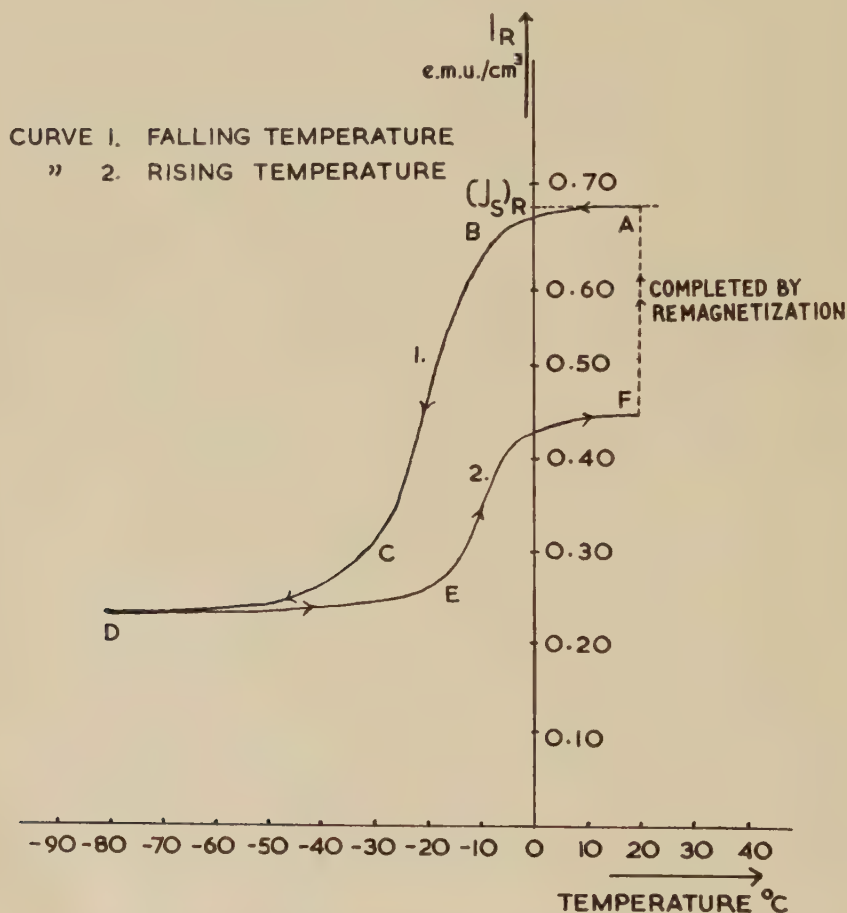


(b) Saturation magnetization of Triassic sandstone while being cooled.
(Saturating field 6000 oersted.)

were cooled to -80°C . It will be seen that no transition is observed, either from the natural or the saturation magnetization.

Spectroscopic analysis has since shown that for detrital particles at least, about 5% of titanium is usually to be found in the hematite in the Triassic rocks. This, according to Morin's results, would account for the transition not being observed in these rocks.

Fig. 2



Variation of the saturation remanence of hematite with temperature (measured in zero magnetic field).

§ 2.2

By way of comparison, fig. 2 shows the behaviour of the remanent magnetization of a specimen of chemically pure hematite when cooled to -80°C . It is interesting to note that the reheating curve does not follow the cooling curve, but by replacing the specimen in the same magnetizing field as initially, the portion F to A is completed and the

cycle can then be retraced. This cyclic hysteresis effect, involving both temperature change and remagnetization, will be further described in a later paper.

§ 2.3

The present paper describes experiments to elucidate more fully the manner in which titanium, and also aluminium impurities, influenced the Morin transition at -15°C .

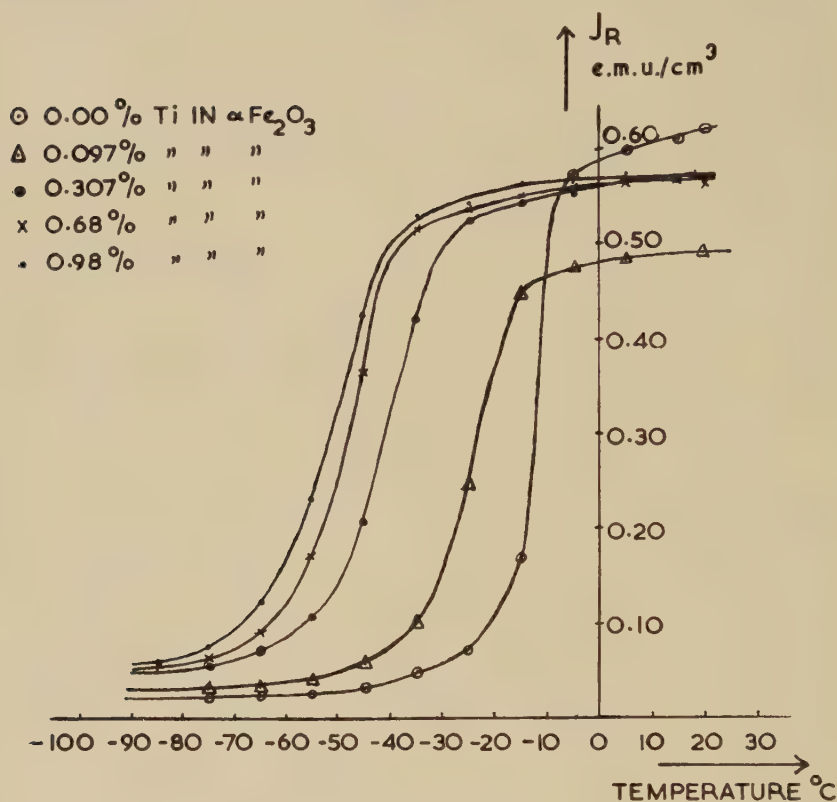
I am indebted to Mr. D. E. Cox of the Chemistry Department of Imperial College, for making up a series of samples in which varying amounts of titanium were added to pure α Fe_2O_3 . The method of preparation was as follows: powders of high purity (at least 99.9%), α Fe_2O_3 and TiO_2 , were weighed, mixed and ground in an agate mortar. Compositions in which titanium (expressed as a percentage of the total metal atoms in the mixture) was 0.1, 0.3, 0.5, 0.7, 0.85 and 1.0 were made up. The mixtures were pressed into pellets under a pressure of about 18 000 p.s.i., and fired for about 16 hours at 1100°C in an atmosphere of oxygen. The fired pellets (grey in colour) were ground to a fine powder in an agate mortar. Small discs, ~ 21 mm diameter and 4 mm thick, were then made, using 0.5 gm of the magnetic material and 2.0 gm of plaster of Paris. These discs, magnetized diametrically in a field of just over 6000 oersted, were then examined individually in a cooling chamber situated in zero field beneath an astatic magnetometer. The variations of the remanent moment of the specimen could then be followed during the cooling, measurements of the magnetization being made at 10° intervals from $+15^\circ\text{C}$ down to -95°C . Because of the hysteresis effect observed during such a temperature cycle, measurements of the magnetization were always made during the cooling.

A measure of the temperature at which this transition occurs can be more easily obtained by taking from the cooling curve, the temperature T_R , at which the magnetization has fallen to a value given by $J_{R,T_R} = \frac{1}{2}(J_{R,\text{init.}} + J_{R,T_L})$, where J_{R,T_L} is the magnetization at the temperature T_L : this being the temperature corresponding to the magnetic state in the low temperature region D of fig. 2, the decrease in magnetization being assumed to be complete at T_L . It is the variation of the 'characteristic temperature' T_R , with titanium content, which is examined here.

A selection of cooling-curves for specimens of this series is shown in fig. 3: the heating portions of the curves being omitted for clarity. These curves may be compared with curves obtained by cooling a natural, and a magnetically saturated, Wirral sandstone (figs. 1 (a) and 1 (b)).

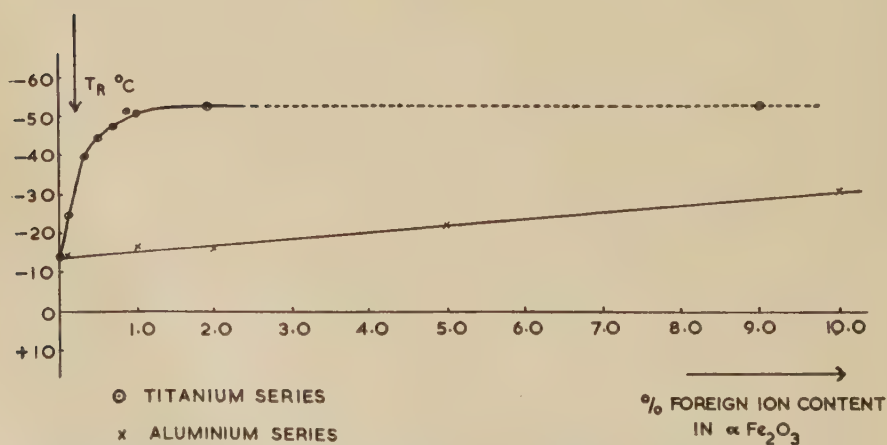
It was found that as the titanium content was increased from 0% to 0.98%, the characteristic temperature varied in a continuous manner from -14.0°C to -51.0°C . Even for a titanium content of 1.92% the transition was still observed. A curve showing the variation of T_R with percentage Ti content is given in fig. 4. From this curve it appears

Fig. 3



Variation of saturation remanence with temperature of $\alpha\text{Fe}_2\text{O}_3$ with different amounts of TiO_2 .

Fig. 4



Curve showing variation of transition temperature with percentage foreign ion content.

that T_R reaches a lower limit of about -52.0°C as the percentage of titanium is increased. This non-disappearance of the transition with increased titanium content conflicts with the work of Morin.

An attempt was made to increase still further the titanium content in $\alpha\text{-Fe}_2\text{O}_3$ by the method described, but on examination of the resulting powder by means of x-ray powder photography, lines other than those of $\alpha\text{-Fe}_2\text{O}_3$ were found. As these only occurred when more than 5% titanium was present, it must be assumed that for these samples the $\alpha\text{-Fe}_2\text{O}_3$ lattice had not accommodated all the Ti atoms present.

Although other compounds were found in the samples containing 5% and 10% Ti, a specimen was made up from the 10% sample and examined in the low temperature region. Here again the transition was still observed, but with a T_R -value of -53°C .

§ 2.4

From these observations it would seem that titanium is not the cause of the disappearance or suppression of the transition in $\alpha\text{-Fe}_2\text{O}_3$ at low temperatures. Consequently, it would appear that the suppression of the transition in the natural rock must be due to some factor other than the titanium impurity. It was, therefore, useful to investigate if the second most common impurity associated with the magnetic fraction of the natural rock, aluminium, was the cause of the suppression, or if it be due to some other entirely different mechanism which has not so far been considered.

§ 3.1

The first of these possibilities has been examined in some detail. A further series of samples was made by Mr. D. E. Cox, in which varying amounts of aluminium were introduced as an impurity into $\alpha\text{-Fe}_2\text{O}_3$. The amount of Al present being expressed as a percentage of the total metal ions in the sample and the method of preparation was identical with that for the Ti series: the Al ions being introduced in the form of Al_2O_3 . Samples were made with the following percentages of Al: 0.099, 1.005, 1.99, 4.986, 9.996. As with the Ti series, the samples were examined by means of x-ray powder photographs for other phases present. The general result indicated a higher solubility of Al in $\alpha\text{-Fe}_2\text{O}_3$ than with the Ti: only a few weak lines appeared in the 5% and 10% samples, indicating the presence of small amounts of a second phase.

As with the Ti series, a value of T_R was determined for each sample: and fig. 4, the curve of T_R plotted against the percentage of Al content in $\alpha\text{-Fe}_2\text{O}_3$, shows that the decrease in T_R with increase in Al is linear within the limits of Al concentration considered here: the transition again being found with high percentages of impurity. A comparison of the curves of fig. 4 would also seem to indicate a greater solubility of Al_2O_3 in $\alpha\text{-Fe}_2\text{O}_3$ than of TiO_2 in $\alpha\text{-Fe}_2\text{O}_3$: in the latter one gets a 'saturation' effect for impurity percentages greater than 1%. Comparing

T_R -values of the two series, those for the aluminium series are much higher than those for the titanium series for corresponding impurity concentrations: 0.17% Ti being as effective as 10% Al in lowering the T_R -value.

From these two experiments it can be concluded that foreign ions of Ti and Al, when introduced into α -Fe₂O₃ by the method described, do not cause a suppression of the transition just below room temperature.

§ 3.2

There is the possibility, particularly in the case of the titanium impurity, that Ti ions introduced in amounts in excess of 1% are not taken up by the α -Fe₂O₃ lattice, but remain in the form of a titanium oxide as a simple mixture with the α -Fe₂O₃. If this were the case, the x-ray picture of the 2% Ti in α -Fe₂O₃ sample would be expected to show lines other than those of α -Fe₂O₃; this is not found to be so. It is only with the 4.8% Ti in α -Fe₂O₃ sample that extra lines begin to appear, though very faintly: these lines being the stronger lines of the compounds ferric titanate (Fe₂O₃·TiO₂), and cubic iron-titanium oxide (FeO·Ti₂O₃). From this it may be concluded that the amount of Ti wholly accommodated by the α -Fe₂O₃ lattice, by the method of preparation used here, is certainly greater than 1% and probably very nearly 4.8%.

These conclusions on the miscibility of the foreign ions Ti and Al in α -Fe₂O₃ seem to be in fairly good agreement with the general results found by other workers (see review by Nicholls (1955)). In general it has been found that Fe⁺⁺⁺ ions in hematite may be replaced by larger amounts of Al ions than by Ti ions; replacement by Ti ions seems to be $\sim 10\%$, whilst the corresponding figure for Al ions is variously quoted as $\sim 10\%$ (Nicholls 1955) to $\sim 36\%$ (Yoshimura 1935). By the method of preparation of the samples described here, nearly 5% of either Ti or Al ions could be introduced into the α -Fe₂O₃ before compounds began to be formed. In no case, however, was the transition suppressed, even though higher percentages were used here than were used by Morin.

§ 3.3

As a consequence of these results it is evident that two outstanding problems arise. In the first place, the results do not agree with Morin's observations on the suppression of the transition, and secondly, they fail to explain the suppression of the transition in the case of the Triassic sandstones.

It is significant to note here that whilst the introduction of foreign ions to hematite produces a lowering of the transition temperature, on no occasion, as a result of any treatment of the hematite, has the transition been observed to occur above -13°C .

§ 4.1

Whilst we have not observed the transition in any natural sandstones we have observed it in a sample of massive hematite, just as Pauthenet

observed it in natural rhombohedral hematite. Common massive hematite, known geologically by the name 'red-hematite', is brownish red in colour, generally possessing a fibrous structure which is cut transversely by a curvilinear banding, and with a surface which is often botryoidal or reniform. The botryoidal masses with radial-fibrous structure, common for instance in Cumberland, break up into conical forms known there as pencil ore.

On the other hand, as will be shown later, specimens of specular hematite studied do not show an appreciable transition effect. These crystals of specular hematite are brilliant steely plates with modified edges, and are usually opaque, but very thin plates when viewed in transmitted light appear a blood-red colour.

§ 4.2

The direction of magnetization, with respect to the fibre-structure in the case of massive hematite, has been found to have an appreciable effect on the shape of the curves in the temperature cycle. Figure 5 (*a*) shows the temperature hysteresis of a specimen magnetized in about 1000 oersted in a direction parallel to the fibre-lines, and fig. 5 (*b*) shows the complementary curves for a similar specimen magnetized in a direction perpendicular to the fibre-lines. The most significant feature common to both these curves is the relatively low temperature at which the transition effects are observed. Following the procedure in § 2.3, the effective transition temperatures in these curves are of the order of -60°C or -70°C , which is somewhat lower than any previously observed value. The low temperature at which the transition takes place is further emphasized in the reheating portions of these curves, where the magnetization attains a maximum at a temperature as low as -20°C , after which thermal demagnetization causes a decrease in intensity as the specimen regains room temperature.

When a sample of massive hematite was ground into a powder, made up into a specimen in the way previously described, and subjected to the usual temperature cycle, the main features of the cooling curves of figs. 5 (*a*) and 5 (*b*) were again observed: the reheating curve, however, was somewhat different in that the amount of recovery was much greater than in either of figs. 5 (*a*) or 5 (*b*), the final intensity being about 70% of the intensity before cooling.

§ 4.3

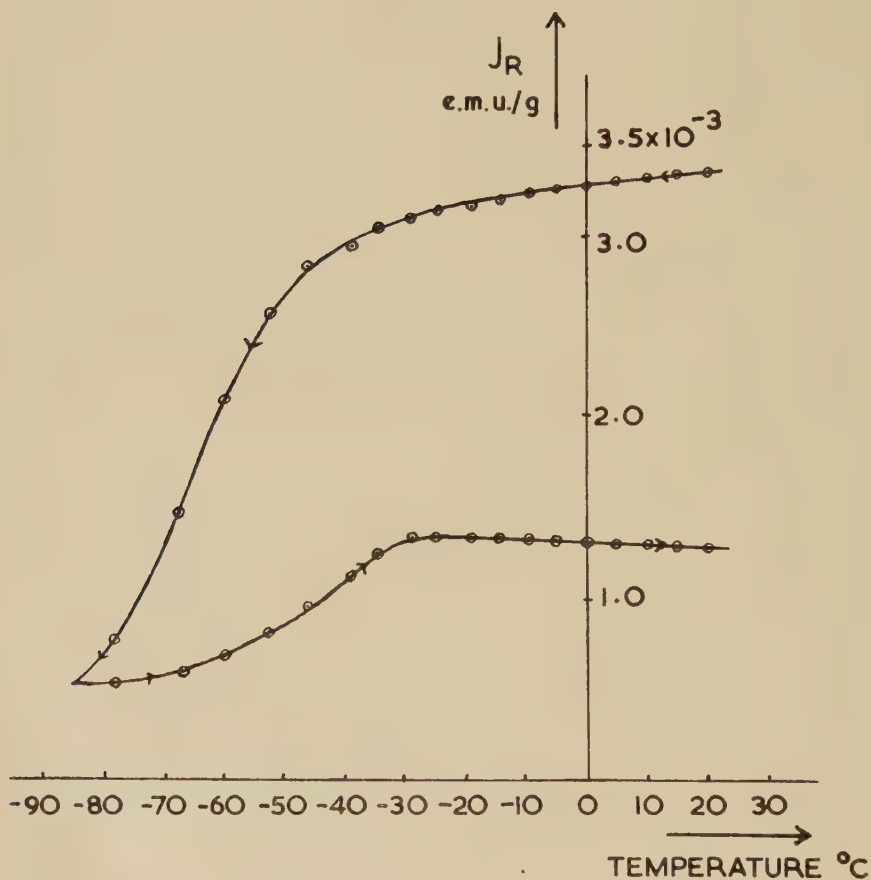
Specular hematite was also examined in the low temperature in both bulk and powdered forms. With the bulk specimens magnetized in about 1000 oersted, the cooling produced a change of less than 7% of the initial intensity. In the coarsely-powdered state, the specimen magnetized in a field ~ 6300 oersted showed a decrease in intensity of only about 10% at -75°C . So we conclude that specular hematite,

both in the bulk and ground-up form, shows almost no sign of the Morin transition.

§ 4.4

The results of the preceding sections indicate that whilst the two naturally occurring forms of hematite examined, that is, the massive and specular types, both have a rhombohedral structure, their magnetic

Fig. 5 (a)



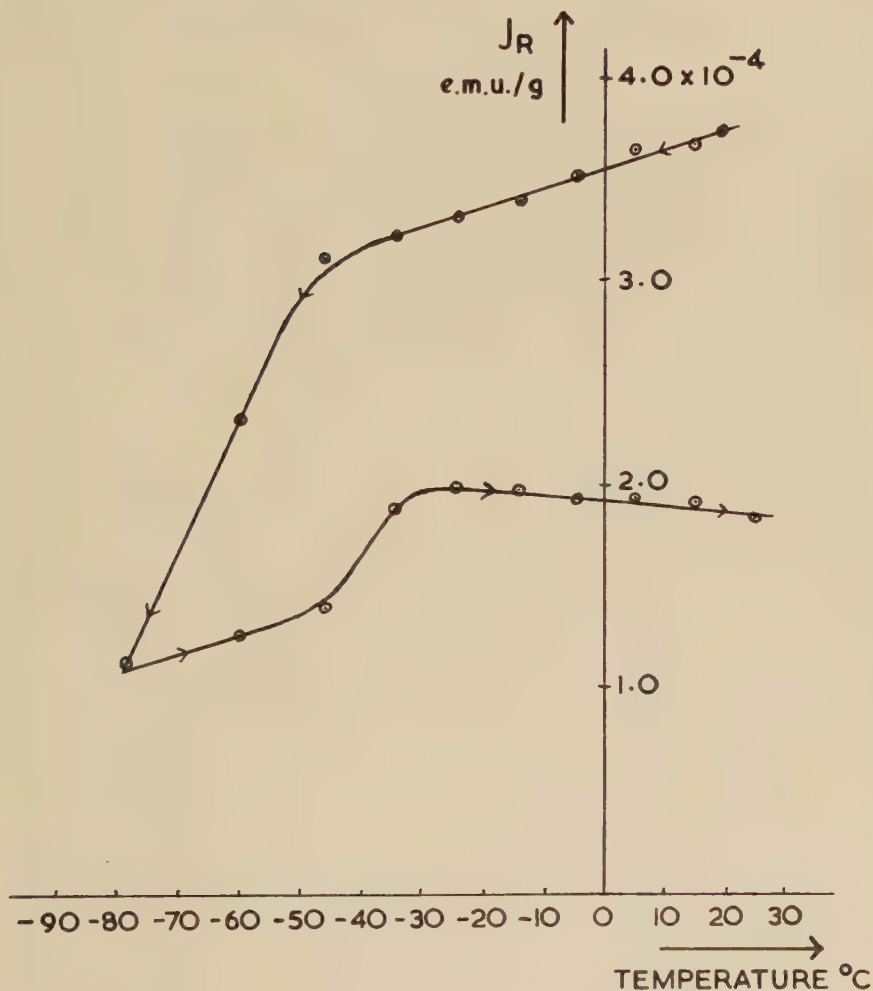
Specimen of massive hematite magnetized in a direction parallel to the fibre-lines.

behaviour is quite different in the low temperature region. Specular hematite shows almost no transition effect, while the massive hematite shows a marked effect, which is, in fact, not very different from that found by Pauthenet for a single rhombohedral crystal from Elba. The Triassic red sandstones behaved in a similar way to the specular hematite

in that little or no transition effect was observed: however, the cause of the suppression of the transition effect may not be the same in both cases.

In general, one must conclude from these results that the Morin transition must be very sensitive to the conditions of growth of the crystals.

Fig. 5 (b)



Specimen of massive hematite magnetized in a direction perpendicular to the fibre-lines.

§ 5.1

To elucidate this fact, the order of magnitude of the size of the crystallites of massive and specular hematite was determined by x-ray photographs. It was found that the massive form of hematite consists

of very fine crystallites, probably less than 1μ in size, whilst single crystallites of specular hematite have been found up to about 1 mm in size, that is, a thousand times as large. It has been suggested that massive hematite occurs in regions where growth is partially inhibited by the pressure of surrounding material, thus restricting the size of crystals formed; whereas specular hematite forms in rock cavities, etc., where growth is relatively free. This, however, is probably an oversimplified picture of the situation. The natural growth of crystals, and crystal habit, is a subject about which little is definitely known.

§ 5.2

The possibility that the observed difference in magnetic properties was simply due to a difference in crystallite size was examined. A sample of specular hematite was wet-ground in an agate mortar until the particle size was less than 1μ . A specimen of this material was then examined in the region of the transition, but no appreciable transition effect was observed. From this we may conclude that whilst a difference in crystallite size does exist between these two materials, it does not appear to be this difference alone which so markedly affects the transition.

§ 5.3

Spectroscopic analysis of the specular and massive hematite samples yielded little new information. Both samples were found to contain 0.7% Si and 0.1% Al. Whilst the massive hematite contained less than 0.01% of either vanadium or titanium, the specular hematite contained 0.06% V and 1.0% Ti. No other elements were detected in either sample. In view of our findings that quite large impurities of titanium do not suppress the transition materials in synthetic materials, it is unlikely that the difference between the magnetic properties of the two forms of natural hematite studied are due to chemical impurities.

§ 6.1

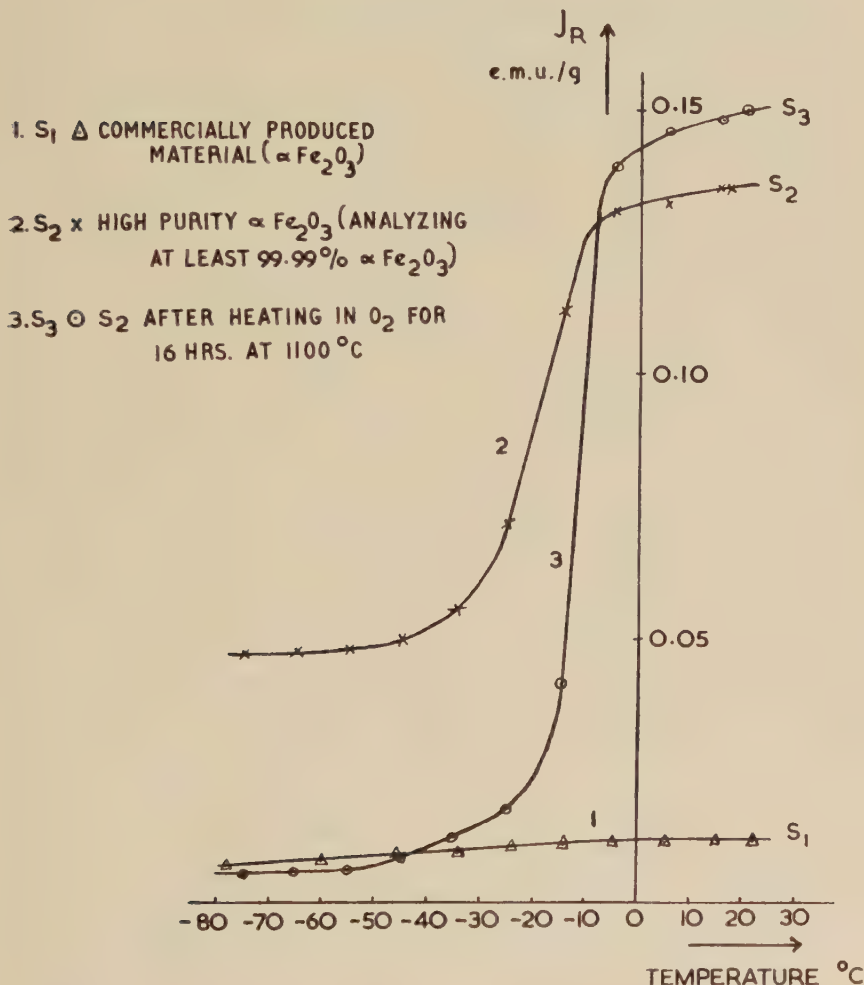
Throughout the course of these experiments it has become increasingly evident that the magnetic properties of hematite are extremely variable, being dependent not only upon the method of preparation of the sample, but also upon the past magnetic and thermal history of the sample. A further study was therefore made of the properties of various samples of synthetic hematite powder. The three curves of figs. 6 and 7 show how the remanent magnetization of various samples decreases as the temperature is lowered. Curve 1 is for sample S_1 , which is a relatively poorly crystalline, commercial preparation of hematite of a brown-red colour; curve 2 is for sample S_2 , a high purity hematite rather purple in colour; whilst curve 3 is for sample S_3 , a dark grey powder formed by heating S_2 in oxygen for 16 hours at 1100°C : this treatment normally increases the homogeneity as well as the crystal size of such a powder.

Whilst all the samples have been shown by x-ray powder photography to be pure α Fe_2O_3 , they exhibit widely different magnetic properties.

§ 6.2

For magnetizing fields $\sim 17\,000$ oersted, the intensities of magnetization of S_1 and S_2 are ~ 0.012 e.m.u./g and 0.135 e.m.u./g respectively :

Fig. 6



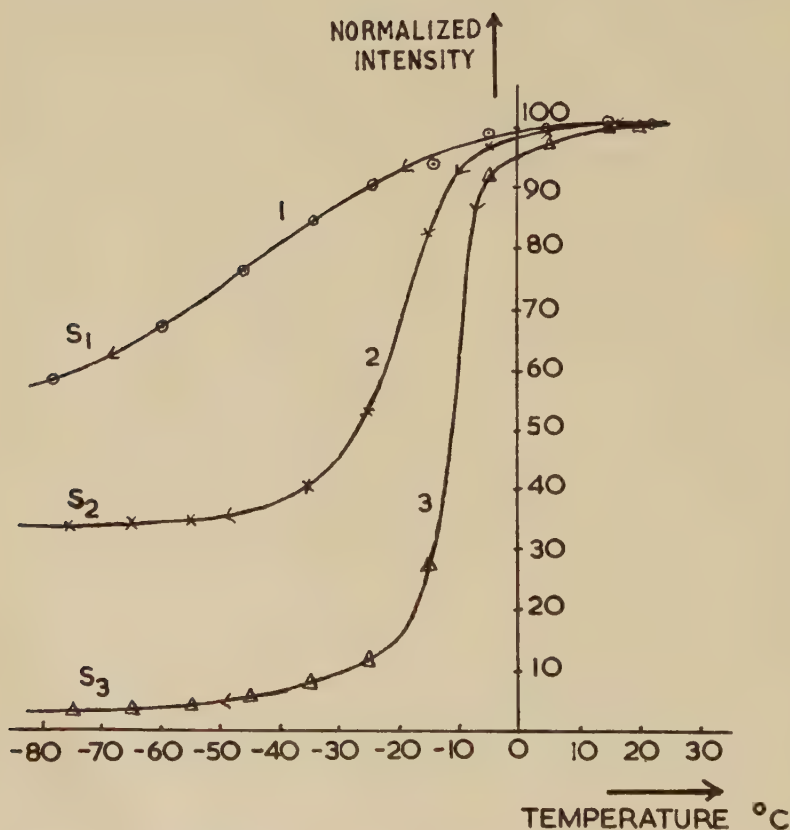
Variation with temperature of remanent magnetization of three different samples of hematite ($\alpha \text{Fe}_2\text{O}_3$).

a difference of more than ten times. In spite of this large difference in saturation magnetization, the remanence coercivities at room temperature for the two samples are nearly the same, viz. ~ 4100 oersted and ~ 4650 oersted for the above saturating field. For specimen S_3 the

corresponding values for saturation magnetization and remanence coercivity are 0.15 e.m.u./g and 2400 oersted. Thus, in the heat treatment of S_2 to form S_3 , the coercivity has decreased by a factor of 2, whilst the saturation magnetization has remained practically unaltered. It would seem that heating samples S_2 at high temperature for any

Fig. 7

1. \circ , S_1 —COMMERCIAL PRODUCED MATERIAL ($\alpha\text{Fe}_2\text{O}_3$)
2. \times , S_2 —HIGH PURITY $\alpha\text{Fe}_2\text{O}_3$ (ANALYZING AT LEAST 99.99% $\alpha\text{Fe}_2\text{O}_3$)
3. Δ , S_3 — S_2 AFTER HEATING IN O_2 FOR 16 HRS. AT 1100°C



Normalized cooling curves for three different samples of hematite ($\alpha\text{Fe}_2\text{O}_3$).

length of time tends to decrease the coercivity of the material without significantly altering the saturation remanence. Apart from the large difference of saturation magnetization at room temperature, the striking feature of the curves of fig. 6 is the large difference in the magnitude of the decrease in intensity as the specimens are cooled. The commercial

hematite, curve 1, fig. 7, shows a decrease to about one-half while the heat-treated pure specimen, curve 3, shows a decrease to one-thirtieth of the value at room temperature.

§ 7.1

The experiments described in the present paper bring out several important facts concerning the magnetic properties and behaviour of hematite. Firstly, naturally occurring hematites can be divided into two groups: those which show the Morrin transition on cooling, and those which do not. Of the samples examined in the present work, the greater proportion fall in the latter group—these being the crystalline specular hematite, and both the detrital and cement forms of hematite found in the natural sandstones. The only sample we have studied falling in the first group is the massive hematite; however, Pauthenet showed that a single rhombohedral crystal from Elba shows the same effect.

Whilst there is a difference in the crystallite size of our two samples, *all* the samples show the normal hematite lattice spacing when examined by x-ray powder methods.

From the spectroscopic analyses of the specular and massive hematite, the only noticeable ion present in some and not in the other is the 1.0% of titanium in the specular material. Whilst this is one of the samples not showing the transition at -15°C , it is in marked opposition to the results of the chemically synthesized series of Ti in α Fe_2O_3 . There is the possibility that the Ti ions in the natural material are more closely linked with the Fe ions, that is, in a more highly ordered state, than in the synthesized material, but the method of synthesis makes this unlikely. However, this does not explain the failure to reproduce Morin's observations, particularly when the samples examined here contained higher percentages of titanium than those used by Morin.

Throughout this work the variability of the properties of hematite and the dependence of the samples on past history has been most noticeable, thus making any generalized statement of the expected properties of any hematite sample almost impossible. Hematite thus lends itself to phenomenological description, but not to a precise quantitative estimate of its properties.

ACKNOWLEDGMENTS

The author wishes to express his indebtedness to Professor P. M. S. Blackett for his constant interest and advice throughout the course of this work.

He also wishes to convey his sincere thanks to Mr. D. E. Cox of the Chemistry Department of this College, who prepared the magnetic samples without which this work could not have been undertaken.

He further wishes to place on record his grateful thanks to the late Dr. H. S. Simons of Birkbeck College for the taking and interpretation of the x-ray powder photographs.

Finally, the author wishes to thank the Lancashire County Education Authority and the Department of Scientific and Industrial Research for grants enabling this research to be undertaken.

REFERENCES

- BLACKETT, P. M. S., 1956, *Lectures on Rock Magnetism* (Weizmann Science Press of Israel).
CLEGG, J. A., ALMOND, M., and STUBBS, P. H. S., 1954, *Phil. Mag.*, **45**, 583.
LENG, J. H., 1955, *Thesis*, University of London.
MORIN, J., 1950, *Phys. Rev.*, **78**, 819.
NICHOLLS, G. D., 1955, *Advanc. in Physics*, **4**, 113.
PAUTHENET, R., in Néel, L., and Pauthenet, R., 1952, *C.R. Acad. Sci., Paris*, **234**, 2172; 1953, *Rev. Mod. Phys.*, **25**, 58.
YOSIMURA, R., 1935, *J. Soc. Chem. Ind., Japan*, **38**, 22.

The Thermal and Magnetic Properties of Neodymium Ethylsulphate at Low Temperatures†

By HORST MEYER
The Clarendon Laboratory, Oxford

[Received December 20, 1956]

ABSTRACT

The entropy, the specific heat and the absolute temperature have been determined as a function of the magnetic temperature for a single crystal of neodymium ethylsulphate in the temperature range between 0.015 and 1°K by adiabatic demagnetization experiments. The specific heat values were confirmed by determination of the magnetic specific heat between 1°K and 2°K by the paramagnetic relaxation method. The results are compared with those expected from paramagnetic resonance data and from Daniels' extension of Van Vleck's theory of dipolar interaction effects. Good agreement is found down to temperatures of about 0.05°K.

§ 1. INTRODUCTION

IN this paper an account is given of demagnetization experiments with a single crystal of neodymium ethylsulphate and the establishment of the absolute temperature scale down to 0.015°K. Results are also given of specific heat measurements by the paramagnetic relaxation method between 2°K and 1°K. This is part of a programme of investigation by different workers in this laboratory of the properties of several ethylsulphates at low temperatures. Unpublished measurements of the thermal and magnetic properties have so far been carried out on cerium, dysprosium and ytterbium salts above and below 1°K and on lanthanum, praseodymium, terbium and erbium salts above 1°K.

The rare earth ethylsulphates are interesting for several reasons: first, since all these salts form isomorphous hexagonal crystals, a systematic investigation of the magnetic and thermal properties of the complete series from lanthanum to ytterbium is possible. This is not the case with the rare earth double nitrates, where only the salts of the elements from lanthanum to gadolinium crystallize. Secondly, extensive use has been made in this laboratory of several of the ethylsulphates as cooling agents for the experiments on nuclear alignment (Cacho *et al.* 1955, Bishop *et al.* 1957). For these experiments it is important to know the absolute temperature scale of the salts. Finally, it is of interest to compare the experimental results with those expected from paramagnetic resonance experiments (Cooke 1955) and from the theory of magnetic interactions of

† Communicated by the Author.

Van Vleck extended by Daniels (1953). This comparison is done in the present paper for the case of neodymium ethylsulphate. It is shown in particular that the agreement with Daniels' calculations of the susceptibility is satisfactory down to about 0.04°K and that the measured specific heat from demagnetization and relaxation experiments also agrees well with the predicted one down to about 0.05°K .

§ 2. GENERAL PROPERTIES OF NEODYMIUM ETHYLSULPHATE

Neodymium ethylsulphate has been the object of several investigations. Its crystal structure, together with that of several other ethylsulphates, has been determined by Ketelaar (1937). The chemical formula is $\text{Nd}(\text{C}_2\text{H}_5\text{SO}_4)_3 \cdot 9\text{H}_2\text{O}$. The salt crystallizes in hexagonal prisms and has a trigonal axis of symmetry. All the paramagnetic ions are equivalent, and there is only one neodymium ion per unit cell. The natural concentration of ^{143}Nd and ^{145}Nd , each having a nuclear spin, is respectively 12.2% and 8.3%, the remaining 79.5% being made up by even isotopes. The ground state of Nd^{3+} is $^4I_{9/2}$ and at temperatures below say 30°K , only the lowest doublet of this state is populated, the next one having an energy of 130 cm^{-1} (Elliott and Stevens 1953). The experiments of Van den Handel and Hupse (1942) showed that at helium temperatures the magnetization of the Nd^{3+} ion in the ethylsulphate both parallel and perpendicular to the crystalline axis is represented exactly by the Brillouin function. This substance behaves therefore in this respect like an ideal paramagnetic. The results of paramagnetic resonance measurements with the field parallel and perpendicular to the crystal axis (Bleaney *et al.* 1954) showed that the spin Hamiltonian \mathcal{H} of the neodymium ion can be written

$$\mathcal{H} = g_{\parallel}\beta S_z H_z + g_{\perp}\beta(S_x H_x + S_y H_y) + \mathcal{H}_{\text{nuc}} \quad . \quad . \quad . \quad (1)$$

where \mathcal{H}_{nuc} is the Hamiltonian for the nuclear splitting of the ground state

$$\mathcal{H}_{\text{nuc}} = AS_z I_z + B(S_x H_x + S_y H_y). \quad . \quad . \quad . \quad . \quad (2)$$

Here $g_{\parallel} = 3.54$ and $g_{\perp} = 2.07$. $S = \frac{1}{2}$ and $I = \frac{7}{2}$ for both odd isotopes. A and B have the values, expressed in cm^{-1} , $^{143}\text{A} = 0.0380$, $^{143}\text{B} = 0.0199$, $^{145}\text{A} = 0.0236$, $^{145}\text{B} = 0.0124$.

Roberts *et al.* (1953) measured above 1°K the paramagnetic susceptibility and the 'magnetic' specific heat by the paramagnetic relaxation method (Casimir and du Pré 1938). Their measurements were carried out on spherical powdered samples of different isotopic compositions. They were thus able to separate the specific heat into its nuclear and electronic constituents. They found good agreement with the values calculated from paramagnetic resonance data for the nuclear specific heat while the electronic term was wholly accounted for by magnetic dipole interaction showing that exchange effects were negligible. For the sample of natural abundance the specific heat they obtained was given by $CT^2/R = 1.09 \times 10^{-3}$.

Daniels (1953) extended Van Vleck's treatment of the magnetic dipole interaction to the anisotropic crystals. He expressed the susceptibility and the entropy as a power series in $1/T$ and calculated the coefficients of the series as far as the term in $1/T^4$ for ions with magnetic dipole interaction in presence or absence of nuclear hyperfine structure (h.f.s.) interaction. He showed in particular that (1) the contributions to the susceptibility χ and the entropy S from h.f.s. and dipolar interactions are additive as far as the term in $1/T^3$, (2) that for the susceptibility the effect of the h.f.s. does not appear in the term in $1/T^2$, i.e. does not affect the Curie-Weiss Δ and that (3) Δ for a powder is not zero in general. Daniels gives detailed expressions for Δ in the case of spherical specimens for several salts, among them the ethylsulphates and a general formula for the higher terms. For a spherical specimen one has per gramme molecule of substance :

$$\chi_{\text{sphere}} = \frac{\lambda}{T} \left(1 + \frac{\Delta}{T} + \frac{E}{T^2} + \dots \right) \quad \dots \quad (3)$$

and for an ellipsoid the susceptibility is

$$\chi_{\text{ellipsoid}} = \frac{\lambda [1 + (\Delta/T) + (E/T^2) + \dots]}{T - \delta [1 + (\Delta/T) + (E/T^2) + \dots]} \quad \dots \quad (4)$$

where

$$\delta = \frac{\lambda}{V} \left(\frac{4\pi}{3} - \alpha \right);$$

λ is the Curie constant of the substance, V the volume of one gramme molecule and α is the demagnetization coefficient of the ellipsoid. It is customary to express the magnetic properties below 1°K by the magnetic temperature T^* defined as the ratio λ/χ for a spherical specimen (Kurti and Simon 1938). One has therefore in the case of an ellipsoid

$$T^* = \frac{\lambda}{\chi_{\text{ellipsoid}}} + \delta. \quad \dots \quad (5)$$

At sufficiently high temperatures the susceptibility is

$$\chi_{\text{ellipsoid}} = \frac{\lambda}{T} \left(1 + \frac{(\Delta + \delta)}{T} \right) \simeq \frac{\lambda}{T - (\Delta + \delta)}. \quad \dots \quad (6)$$

In the case of neodymium ethylsulphate, Daniels calculated for the parallel direction $\Delta_{\parallel} = 13 \times 10^{-3}^\circ\text{K}$ and for the perpendicular direction $\Delta_{\perp} = -2 \times 10^{-3}^\circ\text{K}$. In Appendix 1 of the present paper, the term E is calculated for the case of crystals with axial symmetry, in particular for neodymium ethylsulphate.

§ 3. THE SPECIMEN

Neodymium ethylsulphate was prepared from Johnson Matthey 'Specpure' Nd_2O_3 and 'Analar' materials. An almost transparent single crystal was grown, which was then shaped to an ellipsoid weighing about 2.6 g. and having a length of 1.6 cm and a diameter of 1.3 cm, with

the large axis parallel to the crystalline one. There were probably some water inclusions in the crystal, as the density was only 1.80 compared to the expected value of 1.84 (Ketelaar 1937).

§ 4. THE APPARATUS FOR DEMAGNETIZATION EXPERIMENTS

The specimen was suspended on eight cotton threads in a double walled brass demagnetization cryostat with its crystalline axis either parallel or perpendicular to the cryostat axis. The outer vacuum jacket surrounding the cryostat was made of pyrex and supported a mutual inductance coil with compensated secondaries to measure the susceptibility of the specimen. This unit was immersed in liquid helium and surrounded by a metal dewar of the type described by Henry and Dolocek (1950), using liquid air as external cooling agent. 1.5 litres of liquid helium were sufficient to cool the apparatus and to maintain the bath at 4.2°K and the cryostat at temperatures between 4.2 and 0.85°K for 17 hours. It was not found possible to measure the paramagnetic susceptibility of the specimen with a conventional audio-frequency a.c. bridge because the large amount of metal around the cryostat gave rise to a.c. losses and drifts in the mutual inductance of the coil, and the set-up had to be somewhat modified. Through an automatic contactor, pulses of current were sent through the primaries of the coil and a five decade standard compensating mutual inductance. The signal from the secondary circuit was amplified by a system of galvanometers and photocells (MacDonald 1947) and displayed by a luminous spot on a graduated screen. When the compensation was not exact, the spot moved across the screen at every change of the primary current by an amount proportional to the error in balance. The period of switching the primary current on and off was tuned to that of the amplifier, about 1.5 sec, so that the whole system was in resonance, thus reducing the irregular effects of thermal e.m.f.'s. The measuring field in the primary of the measuring coil was 23 gauss during the calibration and 2.3 gauss when the temperature of the specimen was below about 0.5°K. The sensitivity of the amplification system was sufficient to allow the detection of signal corresponding to a change of mutual inductance of 1.5×10^{-8} henrys or a difference of susceptibility of 5.8×10^{-6} e.m.u./g. The magnetic field for the adiabatic demagnetization was provided by an iron-free solenoid of the type described by Daniels (1950). The maximum field was 24 kilogauss corresponding to a power input of 200 kw to the solenoid.

§ 5. GENERAL DESCRIPTION OF THE METHOD

After the cryostat was cooled down to the temperature of liquid helium, the mutual inductance M of the measuring coil surrounding the specimen was determined at different temperatures between 4.2 and 1.2°K. This calibration gave the relation between T^* and the susceptibility. A series of isentropic demagnetizations was then carried out from known temperatures between 0.85 and 2.0°K and magnetic fields up

to 24 kilogauss. These experiments gave the entropies as a function of the magnetic temperature T^* . The measurement of the specific heat ($C^* = dQ/dT^*$ against T^* was made by heating the specimen with γ -rays (e.g. Kurti and Simon 1935). The relation between the absolute and magnetic temperature was then obtained using the well-known expression

$$T = \frac{C^*}{(\partial S / \partial T^*)_{H=0}} \quad . \quad . \quad . \quad . \quad . \quad . \quad (7)$$

and from this relation, the entropy and the specific heat were calculated as a function of the absolute temperature.

§ 6. THE CALIBRATION OF THE MAGNETIC THERMOMETER

Over the whole series of experiments four calibration curves, each with about 20 points, were taken with the crystal axis of the specimen parallel to the magnetic field and one with the axis perpendicular to the magnetic field. The demagnetization correction was calculated to be $\delta_{\parallel} = 2.2 \times 10^{-3}$ and $\delta_{\perp} = -0.7 \pm 10^{-3}$ in the parallel and in the perpendicular direction respectively. The temperature of the helium in the cryostat was determined from the 1955 helium vapour pressure scale, account being taken of the hydrostatic pressure effect and the thermomolecular pressure correction. In this temperature range, $(M - M_0)$, which is proportional to the susceptibility of the salt, was found to follow a Curie-Weiss law as predicted by eqn. (6) with $\Delta_{\parallel} = (14 \pm 7) \times 10^{-3}$ in the parallel direction and $\Delta_{\perp} = (0 \pm 7) \times 10^{-3}$ in the perpendicular direction, in agreement with the values predicted by Daniels. M_0 is the mutual inductance of the coil in absence of the specimen. The experimental splitting factors were found to be $g_{\parallel} = 3.51 \pm 0.05$ and $g_{\perp} = 2.05 \pm 0.04$, in agreement with the paramagnetic resonance data.

§ 7. THE DETERMINATION OF THE ENTROPY AGAINST T^*

The isentropic demagnetizations from known fields H and temperatures T_i were carried out in the usual way. The temperature T_i was measured with the magnetic thermometer and its constancy during the magnetization was checked by measuring the vapour pressure of the helium in the cryostat with a McLeod gauge via a special manometer line. After the demagnetization, readings of the mutual inductance were started as soon as possible (15 seconds after the demagnetization) and continued every 10 seconds for about 2 minutes. The mutual inductance as plotted against time gave a straight line which was extrapolated back to the time of demagnetization. From eqn. (5), T^* was obtained. From the values of H and T_i the entropy of a gramme molecule of an ideal paramagnetic salt S_{ideal} could be obtained using the tables of Hull and Hull (1941). To obtain the actual entropy, S , of the salt, S_{ideal} had however to be corrected for the effects of the lattice as well as of the dipole and h.f.s. interaction, these being to a good approximation respectively $FT^3/3$ and $D - (G/2T^2)$ between about 0.25 and 4°K. Here F and G are

constants to be determined by experiment. D is the entropy of the degenerate system of the nuclear spins. As the total concentration of the odd isotopes is 20.5%, one has $D=0.205 \times \log (2I+1)=0.426$. A term $\phi(H/T)$, which is calculated in Appendix 2, has also to be added to take account of the additional magnetic field in the crystal created by the magnetic dipoles. It follows that :

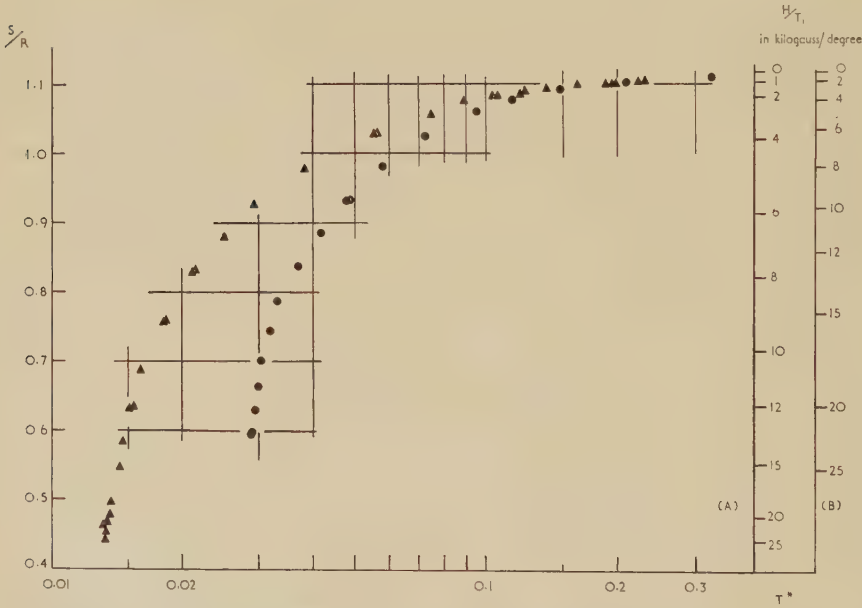
$$\frac{S}{R} = \frac{S_{\text{ideal}}}{R} + \frac{FT^3}{3} - \frac{G}{2T^2} + 0.426 + \phi. \quad (8)$$

The specific heat in zero field is then

$$\frac{C}{R} = FT^3 + \frac{G}{T^2}. \quad (9)$$

With the crystal axis parallel to the field, 10 isentropic demagnetizations from low fields and different temperatures were carried out in the temperature region between 2° and 0.25° to determine F and G . Using the method

Fig. 1



The entropy S/R as a function of the magnetic temperature. \blacktriangle Crystal axis parallel to the field H . \bullet Crystal axis perpendicular to the field H . Columns on the right-hand side : H/T_i for the crystal axis (A) parallel to the field (B) perpendicular to the field.

of least squares, and assuming Curie Weiss's law $T=T^*+14 \times 10^{-3}$ to be valid down to 0.25° (see Appendix 1) these constants were found to be

$$F=(2.1 \pm 0.4) \times 10^{-3} ; G=(1.16 \pm 0.04) \times 10^{-3}.$$

Figure 1 shows the experimental points of the entropy against the magnetic temperature for demagnetizations of the crystal with the axis parallel

and perpendicular to the field and the first three columns of table 1 give smoothed values. It can be seen that the susceptibility in the parallel direction reaches a constant value for an entropy $S/R=0.45$ corresponding to $T_{\parallel}^*=0.0132$. At temperatures below about 0.1°K , relaxation effects of the spin system, already described in detail by De Klerk (1951) and Beun *et al.* (1955) were observed.

§ 8. THE DETERMINATION OF THE SPECIFIC HEAT AND OF THE ABSOLUTE TEMPERATURE SCALE

The determination of the specific heat C^* below 1°K was done with the crystal axis parallel to the field. The experiment gave C^* in arbitrary

Table 1. Neodymium ethylsulphate

$\frac{S}{R}$	T_{\parallel}^*	T_{\perp}^*	$\frac{C^*}{R}$	T	$\frac{C_{\text{exp}}}{R}$	$\int_{T=1^{\circ}\text{K}}^T \frac{C}{R} dT$	$\frac{C_{\text{magn. calc.}}}{R}$
1.115	0.478	0.490	0.50×10^{-2}	0.492	0.50×10^{-2}	1.63×10^{-3}	0.46×10^{-3}
1.110	0.285	0.300	1.25	0.300	1.25	3.15	1.23
1.105	0.211	0.228	2.13	0.225	2.13	4.35	2.11
1.100	0.169	0.188	3.03	0.183	3.03	5.46	3.03
1.090	0.123	0.139	4.95	0.136	4.95	7.20	4.95
1.070	0.0845	0.102	8.50	0.0965	8.50	9.60	8.50
1.050	0.0685	0.085	10.5	0.0795	10.5	11.2	11.0
1.025	0.0540	0.070	14.2	0.0645	14.0	13.0	14.2
1.000	0.0450	0.0625	17.2	0.0550	16.7	14.5	17.0
0.950	0.0330	0.0500	26.3	0.0426	25.0	17.2	20.5
0.900	0.0267	0.0433	35.5	0.0370	31.5	18.5	23.0
0.850	0.0228	0.0380	48.0	0.0318	41.0	20.5	26.0
0.800	0.0200	0.0341	63.0	0.0283	46.5	21.9	—
0.750	0.0181	0.0320	79.0	0.0260	51.0	22.9	—
0.700	0.0165	0.0305	96.0	0.0226	52.5	24.7	—
0.650	0.0154	0.0298	113	0.0208	53.0	26.0	—
0.600	0.0148	0.0289	125	0.0195	54.0	26.8	—
0.550	0.0143	—	134	0.0185	55.0	—	—
0.500	0.0137	—	150	0.0167	—	—	—
0.450	0.0133	—	165	0.0160	—	—	—

Remarks

1. At 'infinite' temperatures, the entropy of the magnetic effects in zero field is $S/R=1.119$

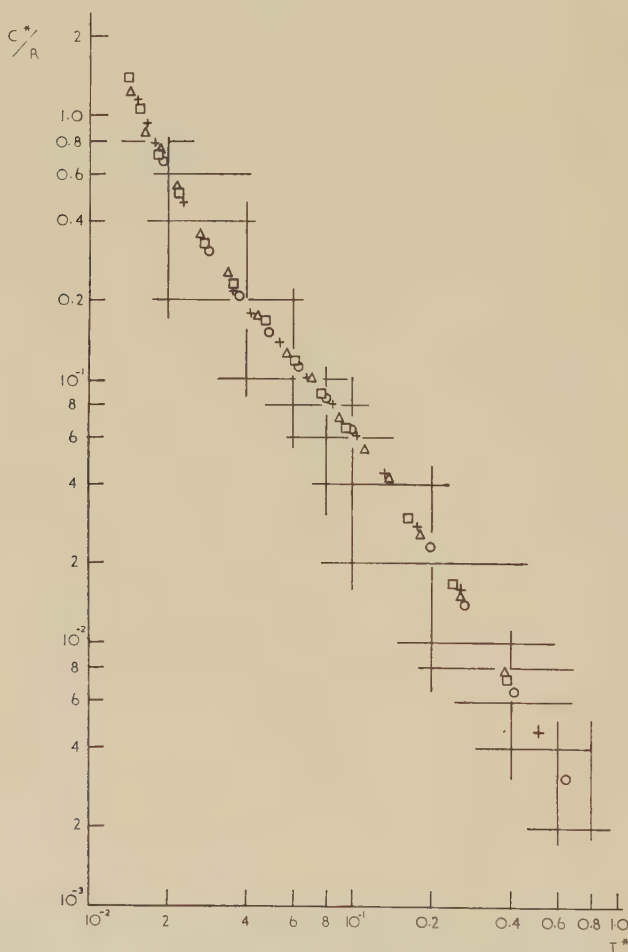
2. In column 7, the energy E/R is given, which has to be extracted if the salt is to be cooled from 1°K to the temperature T .

units as a function of T_{\parallel}^* . From eqn. (7) the relation between T and T_{\parallel}^* was obtained in arbitrary units of T . By fitting this curve at 0.5°K to the Curie-Weiss law $T=T_{\parallel}^*+14 \times 10^{-3}$, T was obtained in degrees as a function of T_{\parallel}^* between 0.015 and 0.5° . Smoothed values are given in table 1 which shows that the Curie-Weiss law extends down to about

$T=0.15^\circ\text{K}$. In this region C^* is therefore equal to $C=dQ/dT$. Again, using eqn. (7), C^* could be obtained in absolute units.

Above 0.24°K , C obeyed eqn. (9) with $G=(1.14\pm 0.04)\times 10^{-3}$ and $F=(2\pm 1)\times 10^{-3}$ in good agreement with the results obtained in § 7. This shows that the use of the Curie-Weiss law makes the results consistent. The experimental points of C^*/R are given in fig. 2. Combining

Fig. 2



The magnetic specific heat C^*/R as a function of T^* .

the different experimental data obtained with the crystal axis parallel and perpendicular to the magnetic field, the relationship between S/R , C^*/R , C/R , T , $T_{||}^*$ and T_{\perp}^* was obtained. The smoothed results are given in table 1 in the first six columns. The enthalpy derived from the measurements is given in column 7. Table 2 gives the absolute

temperatures reached after adiabatic demagnetization as a function of H/T_i .

An independent check of the specific heat values below 1 K was made by carrying out measurements of the magnetic specific heat between 1°K and 2°K with the paramagnetic relaxation method (Casimir and du Pré 1938) using the same crystal as before. The experiments were made at a frequency of 900 c.p.s. and in magnetic fields up to 380 gauss on an apparatus kindly lent by Dr. A. H. Cooke. The results can be seen in table 3.

Table 2. Absolute temperature reached after demagnetization as a function of the ratio H/T_i in kilogauss/degree

(1) Crystal axis parallel to the field H .

(2) Crystal axis perpendicular to the field H .

H/T_i	0	1	2	3	4	5	8	10	15	20	25
$T(1)$	0.900	0.304	0.144	0.089	0.062	0.037	0.029	0.024	0.0180	0.0165	0.015*
$T(2)$	0.900	0.428	0.248	0.160	0.118	0.063	0.052	0.040	0.0265	0.0210	0.018*

* By extrapolation.

Table 3. Magnetic specific heat of neodymium ethylsulphate above 1°K

T	CT^2/R
2.27°K	$(1.13_3 \pm 0.015) \times 10^{-3}$
2.01	1.13 ₀
1.59	1.14 ₀
1.32	1.13 ₀
1.06	1.13 ₅

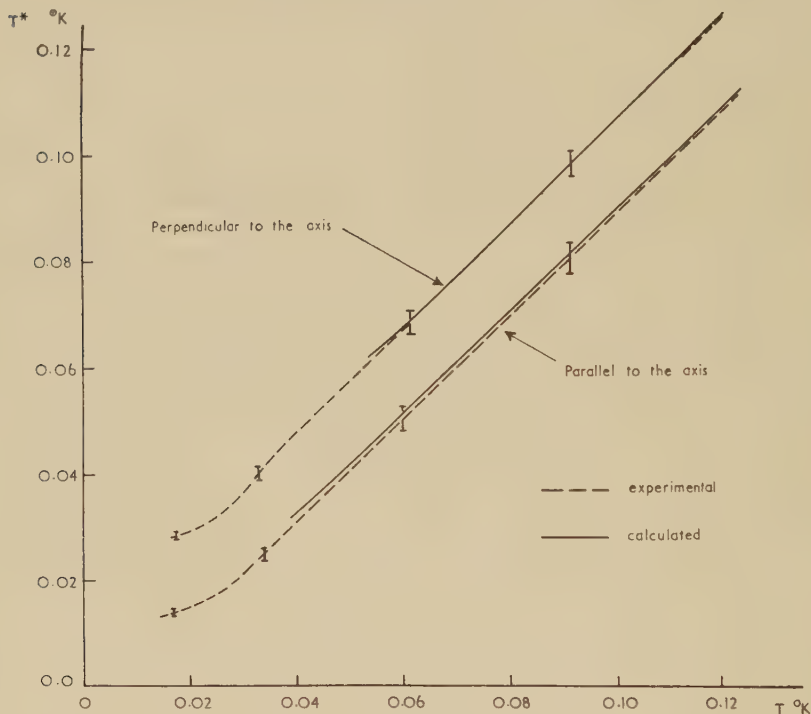
§ 9. DISCUSSION

The measured specific heat of neodymium ethylsulphate may be compared with the value obtained from the paramagnetic resonance data of Bleaney *et al.* (1954). The magnetic specific heat at temperatures above about 0.25 K, which is the sum of the h.f.s. and the dipole interaction contributions, is calculated from a series expansion of the partition function (Bleaney 1950) to be $CT^2/R = 1.11_6 \times 10^{-3}$, in good agreement with all our experimental results, which therefore confirm Roberts's findings and conclusions.

At lower temperatures, the nuclear specific heat has to be calculated from the exact partition function $Z = \sum_j \exp(-W_j/kT)$. The energies of

the levels W_j are to be found in the paper by Bleaney *et al.* We then assume that the relation for the dipole interaction (Daniels *loc. cit.*) is valid down to 0.05°K . The total magnetic specific heat is given in table 1, column 8. The agreement with the experimental values is good down to about 0.05°K .

Fig. 3



The magnetic temperature as a function of the absolute temperature in the parallel and in the perpendicular direction to the axis.

In fig. 3, the experimental relations between magnetic and absolute temperatures in both directions are compared with the calculated ones (see Appendix 1). Over the whole temperature range where the power series converge, the agreement is within the experimental error, $\pm 6\%$. Thus for the parallel direction the comparison extends down to 0.04°K .

In conclusion it may be said that neodymium ethylsulphate is a suitable substance for demagnetization work and for testing the theories for the thermal and magnetic properties. It would be interesting to demagnetize samples of this salt with greatly enriched even neodymium isotopes as one would then be able to reach lower temperatures and study the cooperative phenomena due to pure magnetic dipole interaction. Lower temperatures could also be reached by demagnetizing crystals of neodymium ethylsulphate of natural isotopic composition, magnetically

diluted with lanthanum ethylsulphate. From the above calculations and experiments, it is easy to estimate fairly well the lowest temperature attainable with a certain concentration of neodymium ions in the crystal and to calculate the approximate relation between T and T^* . Thus one can expect to reach a temperature of about $8 \times 10^{-3}^\circ\text{K}$ for a concentration of 20% Nd^{3+} and a temperature of $6 \times 10^{-3}^\circ\text{K}$ for a concentration of 10% Nd^{3+} starting from an $H/T_i = 25$ kilogauss/degree.

ACKNOWLEDGMENTS

The author wishes to thank very much the late Professor Sir Francis Simon, Dr. N. Kurti and Dr. A. H. Cooke for their interest in this work. He is very indebted to Dr. C. E. Johnson and Mr. F. R. McKim for assistance in the experiments and for helpful suggestions. He also thanks Mr. Hopkins for constructing the standard mutual inductance. These experiments were done during the tenure of a Nuffield Fellowship.

APPENDIX 1

The Evaluation of E in the Susceptibility Expansion Series

As shown by Daniels

$$E = E_0 + E^1$$

where E_0 is the effect of the pure dipole interaction and E^1 is the effect of the h.f.s.

Calculation of E_0

The general expression for this calculation, too long to be reproduced here, is derived from the formulae 3, 8 and 10 in Daniels' paper. For a crystal with the symmetry axis parallel to the z -axis of the reference system, one obtains :

parallel direction :

$$E_{0\parallel} = \frac{g_{\parallel}^4 \beta^4}{16k^2} \left[\left\{ \sum_j \left(\frac{1}{r_{ij}^3} - \frac{3z^2}{r_{ij}^5} \right) \right\}^2 - \sum_j \frac{1}{r_{ij}^6} - \frac{6z^2}{r_{ij}^8} + \frac{9z^4}{r_{ij}^{10}} \right] + \frac{g_{\parallel}^2 g_{\perp}^2 \beta^4}{16k^2} \cdot 9 \left[\sum_j \frac{z^4}{r_{ij}^{10}} - \frac{z^2}{r_{ij}^8} \right],$$

perpendicular direction :

$$E_{0\perp} = \frac{g_{\perp}^4 \beta^4}{16k^2} \left[\frac{1}{4} \left\{ \sum_j \left(\frac{1}{r_{ij}^3} - \frac{3z^2}{r_{ij}^5} \right) \right\}^2 - \frac{1}{2} \sum_j \frac{5r_{ij}^4 - 12r_{ij}^2 z^2 + 9z^4}{r_{ij}^{10}} \right] + \frac{g_{\parallel}^2 g_{\perp}^2 \beta^4}{16k^2} \cdot \frac{9}{2} \left[\sum_j \frac{z^4}{r_{ij}^{10}} - \frac{z^2}{r_{ij}^8} \right]$$

where r_{ij} is the distance between the ions i and j , and z is its component along the z -axis. The lattice sums $\sum_j 1/r_{ij}^6$, $\sum_j z^2/r_{ij}^8$. . . have been

evaluated by Daniels for the case of the ethylsulphates. These are :

$$\left. \begin{aligned} \sum_j \frac{1}{r_{ij}^6} &= 245.53 \\ \sum_j \frac{z^2}{r_{ij}^8} &= 144.32 \\ \sum_j \frac{z^4}{r_{ij}^{10}} &= 128.07 \\ \left(\sum_j \frac{3z^2}{r_{ij}^5} - \frac{1}{r_{ij}^3} \right)^2 &= 349.69 \end{aligned} \right\} \times a \text{ \AA}^{-6}$$

where a is a certain dimension in the unit cell of the lattice. Thus for the ethylsulphates one obtains :

$$E_{011} = -a^{-6} \times 10^{-48} [4.42 \times g_{11}^4 + 3.54 \times g_{11}^2 g_{12}^2]$$

$$E_{012} = -a^{-6} \times 10^{-48} [5.72 \times g_{12}^4 + 1.76 \times g_{11}^2 g_{12}^2].$$

Substituting the values $g_{11} = 3.54$, $g_{12} = 2.07$, $a = 13.992 \text{ \AA}$ for neodymium ethylsulphate, one obtains :

$$E_{011} = -1.16 \times 10^{-4}$$

$$E_{012} = -2.64 \times 10^{-5}.$$

Calculation of E^1

In the case of an ion with hyperfine structure, it has been shown (Cooke *et al.* 1956) that

$$E_{11}^1 = -I(I+1) \cdot \frac{2B^2}{36}$$

$$E_{12}^1 = -I(I+1) \cdot \frac{(A^2 + B^2)}{36}.$$

For ^{143}Nd , $E_{11}^1 = -7.00 + 10^{-4}$ $E_{12}^1 = -1.64 + 10^{-3}$

while for ^{145}Nd , $E_{11}^1 = -2.74 + 10^{-4}$ $E_{12}^1 = -6.45 + 10^{-4}$

E^1 is thus comparable to E_0 .

Adding E_0 to E^1 and taking into account the concentration of the isotopes in the natural neodymium one finally obtains for the susceptibility of neodymium ethylsulphate :

$$\chi_{11} = \frac{\lambda_{11}}{T_{11}^*} = \frac{1.172}{T} \left[1 + \frac{1.32 \times 10^{-2}}{T} - \frac{2.24 \times 10^{-4}}{T^2} \dots \right]$$

$$\chi_{12} = \frac{\lambda_{12}}{T_{12}^*} = \frac{0.403}{T} \left[1 - \frac{2.3 \times 10^{-3}}{T} - \frac{2.80 \times 10^{-4}}{T^2} \dots \right].$$

APPENDIX 2

Evaluation of the term $\phi(H/T)$

The treatment is the same for ions with or without h.f.s., since to a good approximation the h.f.s. does not contribute to a change of the entropy in a magnetic field. For the sake of simplicity, we are also not taking

account of the splitting of the energy levels by the dipole interactions in zero field

$$H_{\text{eff}} = H + \epsilon M'$$

where M' is the magnetic moment per cm^3 and ϵ is a constant to be determined. We make the assumption that $\epsilon M' \ll H$, so that it can be treated as a perturbation. As a first approximation, we can put

$$M' = N'(\frac{1}{2}g\beta) \tanh x$$

where N' is the number of ions per cm^3 and $x = g\beta H/2kT$ assuming $S = \frac{1}{2}$. We omit here the indices 'parallel' and 'perpendicular' as this calculation applies to any direction with respect to the crystalline axis.

The partition function of an assembly of N ions is then

$$Z = 2^N \left(\cosh x + \frac{\epsilon N' g^2 \beta^2}{2kT} \tanh x \sinh x \right)^N.$$

From the well known relation $S = (\partial/\partial T)kT \ln Z$ one derives

$$\frac{S}{R} = \ln 2 + \ln \cosh x - x \tanh x - \frac{\epsilon N' g^2 \beta^2}{2kT} x \tanh x \operatorname{sech}^2 x.$$

The sum of the first three terms is the entropy S/R_{ideal} mentioned before, and the fourth term is due to the field of the magnetic dipoles.

For small fields, this equation reduces to the one derived from Daniel's series expansion. One obtains by identification: $\Delta = \epsilon N' g^2 \beta^2 / 2k$. One has finally $S/R = S_{\text{ideal}}/R + \phi(H/T)$ where $\phi(H/T) = (x\Delta/T) \tanh x \operatorname{sech}^2 x$. For the case of Neodymium ethylsulphate the effect of ϕ on the entropy S/R is very small. It can easily be seen that $\phi \leq (\Delta/T)(\ln 2 - S_{\text{ideal}}/R)$.

REFERENCES

- BEUN, J. A., STEENLAND, M. J., DE KLERK, D., and GORTER, C. J., 1955, *Physica*, **21**, 651.
 BISHOP, G. R., GRACE, M. A., JOHNSON, C. E., KURTI, N., LEMMER, H. R., and PEREZ Y JORBA, J., 1957, *Phil. Mag.*, **2**, 534.
 BLEANEY, B., 1950, *Phys. Rev.*, **78**, 214.
 BLEANEY, B., SCOVIL, H. E. D., and TRENAM, R. S., 1954, *Proc. Roy. Soc. A*, **223**, 15.
 CACHO, C. F. H., GRACE, M. A., JOHNSON, C. E., KNIPPER, A. C., SCURLOCK, R. G., and TAYLOR, R. T., 1955, *Phil. Mag.*, **46**, 1287.
 CASIMIR, H. B. G., and DU PRÉ, F. K., 1938, *Physica*, **5**, 507.
 COOKE, A. H., 1955, *Conf. Phys. Basses. Temps.* (Paris), p. 178.
 COOKE, A. H., MEYER, H., and WOLF, W. P., 1956, *Proc. Roy. Soc. A*, **233**, 536.
 DANIELS, J. M., 1950, *Proc. Phys. Soc. B*, **63**, 1028; 1953, *Proc. Phys. Soc. A*, **66**, 673.
 DE KLERK, D., 1931, *Proc. N.B.S. Symposium on Low Temperature Physics*, p. 211.
 ELLIOTT, R., and STEVENS, K. W. H., 1953, *Proc. Roy. Soc. A*, **219**, 387.
 HENRY, W. E., and DOLOCEK, R. L., 1950, *Rev. Sci. Instr.*, **21**, 496.
 HULL, J. R., and HULL, R. A., 1941, *J. Chem. Phys.*, **9**, 465.
 KETELAAR, J. A. A., 1937, *Physica*, **4**, 619.
 KURTI, N., and SIMON, F. E., 1935, *Proc. Roy. Soc. A*, **152**, 21; 1938, *Phil. Mag.*, **26**, 497.
 McDONALD, D. C. K., 1947, *J. Sci. Instr.*, **24**, 232.
 ROBERTS, L. D., SARTAIN, C. C., and BORIE, B., 1953, *Rev. Mod. Phys.*, **25**, 170.
 VAN DEN HANDEL, J. H., and HUPSE, J. C., 1942, *Physica*, **9**, 225.

Nuclear Alignment of $^{147}\text{Nd}^\dagger$

By G. R. BISHOP[‡], M. A. GRACE, C. E. JOHNSON, H. R. LEMMER and
J. PEREZ Y JORBA[‡]

Clarendon Laboratory, Oxford

[Received February 4, 1957]

ABSTRACT

Neodymium 147 has been aligned in a crystal of neodymium ethyl sulphate. The directional distributions and states of polarization of the 90 and 530 kev γ -rays have been measured. It is concluded that both transitions are mixtures of M1 and E2 radiation ($\delta E2/M1 = -0.17 \pm 0.15$ for the 90 kev and $+0.75 \pm 0.25$ for the 530 kev γ -rays) and that the 530 kev state has spin $7/2^+$. From the 530 kev results a value for the nuclear magnetic moment of ^{147}Nd of 0.44 ± 0.06 nuclear magnetons is found.

§ 1. INTRODUCTION

THE nuclide neodymium 147 has been the subject of several investigations, including nuclear alignment experiments by Ambler *et al.* (1955, 1956). They obtained the alignment by cooling crystals of neodymium-cerium magnesium nitrate ($\text{Nd } 1\% \text{ Ce } 99\% \text{)}_2\text{Mg}_3(\text{NO}_3)_{12} \cdot 24 \text{ H}_2\text{O}$ containing some ^{147}Nd , the cerium being included for the purposes of magnetic cooling, and they measured the spatial distribution of γ -radiation emitted in the radioactive decay. The neodymium ion has a large and anisotropic hyperfine structure coupling in this salt and the lowest magnetic state has $I_z = \pm \frac{1}{2}$, hence at low temperatures the nuclear spins precess approximately in the plane perpendicular to the symmetry axis and they are said to be 'aligned' in this plane (see e.g. Bleaney 1951). With this type of orientation the lower nuclear magnetic levels are compressed compared with those of a system where the nuclei are aligned along the axis, i.e. where $I_z = \pm I$ state lies lowest, and for a given hyperfine structure interaction and temperature larger directional effects in the γ -radiation will be observed for axial alignment than for planar 'alignment'. For these reasons we decided to align ^{147}Nd in neodymium ethyl sulphate, in which axial alignment is produced, and measurements were made of both the state of polarization and the directional distribution of the γ -radiation in order to determine the dipole-quadrupole admixture in the γ -ray transitions.

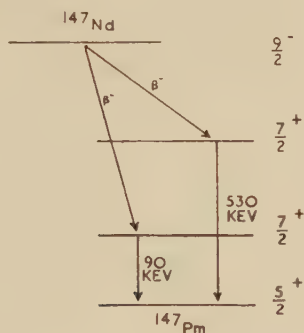
[†] Communicated by the Authors.

[‡] Now at the Ecole Normale Supérieure, Paris.

§ 2. DISINTEGRATION SCHEME

Eleven-day ^{147}Nd decays with the emission of two main β -groups which lead to excited states of 90 and 530 kev in the daughter nuclide ^{147}Pm (see fig. 1). The comparative half-lives ($\log ft=7.4$ and 7.0) of these two groups indentify them as first forbidden with a change in spin of 0 or 1 and a change in parity. The absence of a β -group to the ground state suggests that such a transition would involve a spin change of at least 2. The half-life of the 90 kev state (2.44×10^{-9} sec) led Graham and Bell (1953) to classify the transition of M1. Since both transitions lead to the ground state they must involve the same parity change and hence the 530 γ -ray must be M1, E2 or a mixture of these; higher multipoles are excluded by lifetime measurements ($<10^{-7}$ sec). The internal conversion data are in accord with these assignments. Many weaker γ -rays are also present in the decay of ^{147}Nd but since their multipolarity assignments are uncertain, attention has been concentrated on the prominent γ -rays in the nuclear orientation experiments.

Fig. 1

The decay scheme of ^{147}Nd .

The daughter nucleus ^{147}Pm decays to ^{147}Sm the spin and moment of which identify it as $7/2^-$ (Murakawa 1954). From the first forbidden character of this β -transition an assignment of $5/2^+$ to the ground state of ^{147}Pm may be made and the absence of a β -transition to this state suggests that the ground state of ^{147}Nd is $9/2^-$. This leads to an assignment of $7/2^+$ to the 90 kev state and either $7/2^+$ or $9/2^+$ to the 530 kev state, as shown in fig. 1, and these have been assumed in the interpretation of the nuclear orientation results.

§ 3. EXPERIMENTAL

Bleaney, Scovil and Trenam (1954) have shown that the energies of the states of the Nd^{3+} ion in neodymium ethyl sulphate (diluted with lanthanum ethyl sulphate) can be described by a Spin-Hamiltonian of the form

$$\mathcal{H} = g_{\parallel} \beta H_z S_z + g_{\perp} \beta (H_x S_x + H_y S_y) + A S_z I_z + B (S_x I_x + S_y I_y)$$

where

$$g_{\parallel} = 3.5 \quad g_{\perp} = 352.072 \quad S = 1/2$$

Fig. 2

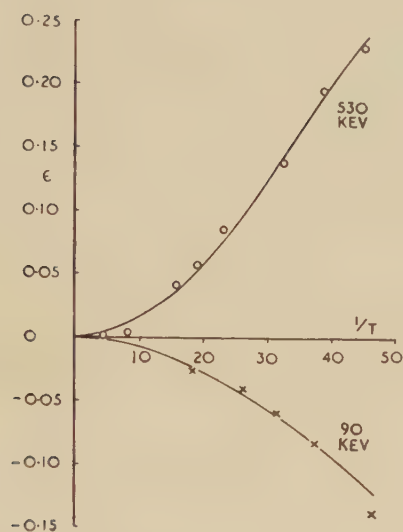
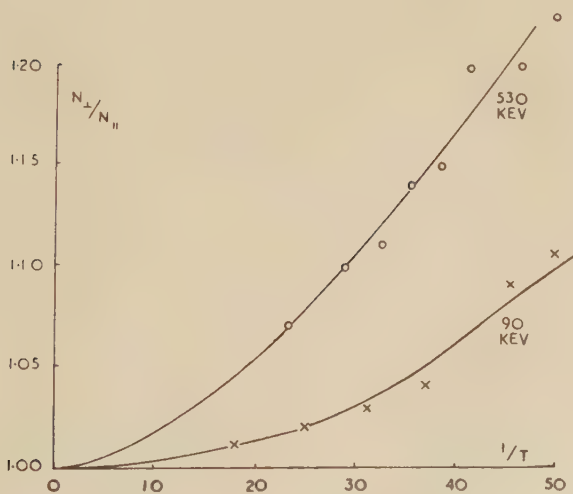
Variation of γ -ray anisotropy ϵ with $1/T$.

Fig. 3

Variation of p' ($=N_{\perp}/N_{\parallel}$) with $1/T$.

emitted at an angle θ to the axis. Figure 2 shows the variation of ϵ with $1/T$ for the 90 and 530 keV γ -rays.

The γ -ray polarimeter described by Bishop and Perez (1955) was set up near the cryostat so that the scatterer received radiation emitted in the equatorial plane where the polarization effect is a maximum. Measurements were made of N_{\parallel} and N_{\perp} , which are the counting rates for radiation scattered parallel to and perpendicular to the alignment axis. The effects of the 90 and 530 keV γ -rays were separated by pulse height selection of the recoil electron pulse in the scattering phosphor. The variation with $1/T$ of $p' = N_{\perp}/N_{\parallel}$ is shown in fig. 3. The degree of polarization p is defined by

$$p = \frac{I(\pi/2, \pi/2) - I(\pi/2, 0)}{I(\pi/2, \pi/2) + I(\pi/2, 0)} \quad (2)$$

where $I(\theta, \phi)$ is the intensity of radiation at an angle θ to the axis with its electric vector inclined at an angle ϕ to the plane containing the axis and the direction of propagation. It is related to the measured p' by the formula

$$p = \frac{1 - p' R + 1}{1 + p' R - 1} \quad (3)$$

where R is the analysing ratio of the polarimeter.

§ 4. RESULTS

For low degrees of alignment ($A/T \ll 1$) the intensity $I(\theta, \phi)$ can be expressed in the form

$$I(\theta, \phi) = 1 + B_2(T) [A_2 P_2(\cos \theta) + A_2' \cos 2\phi P_2^2(\cos \theta)] \quad (4)$$

(see e.g. Cacho *et al.* 1955). $B_2(T)$ describes the orientation as a function of temperature. A_2 and A_2' are parameters determined by the disintegration scheme and involve the spins of the levels and δ , the quadrupole-dipole amplitude mixing ratio. $P_2(\cos \theta)$ and $P_2^2(\cos \theta)$ are Legendre and associated Legendre polynomials.

The advantage of considering low degrees of alignment is that terms in $P_4(\cos \theta)$ and higher do not occur, and eqns. (1), (2) and (4) then give the following simple relation between polarization and anisotropy at any arbitrary temperature: $p/\epsilon = 2A_2'/A_2$. This ratio is a function of δ , and tends to unity for a pure dipole γ -ray ($\delta = 0$). Simultaneous measurements of ϵ and p' therefore enable δ to be determined.

In the table the observed values of ϵ and p' are given for $1/T = 25$. The analysing ratio R for the polarimeter was determined experimentally as 5.0 ± 0.02 and 2.1 ± 0.2 for radiation of 360 and 935 keV energy respectively. By interpolation a value of 3.5 ± 1.0 for 530 keV radiation was found. As it is doubtful how R varies for energies below 360 keV it was assumed to lie between 2 and 10 for the 90 keV radiation. Column 4 gives the polarization p . The results show that a spin of $9/2^+$ for the 530 keV is not possible since this requires the transition to be pure E2, which would

give a positive sign for p whereas a negative sign was observed. The spin must therefore be $7/2$ which fixes A_2 . In column 5 is given δ determined from these values and from δ and ϵ the value of $B_2(T)$ for this temperature was calculated.

In the evaluation of $B_2(T)$ as a function of A/T exact calculation of the ionic level positions and the contributions to them by different nuclear states was made. From our experimental value of $B_2(T)$ at $1/T=25$ the hyperfine structure constant A for ^{147}Nd was determined. Since AI/μ must be a constant for all neodymium isotopes the magnetic moment of ^{147}Nd may be determined and is shown in column 6. The solid curves in fig. 2 and 3 have been derived theoretically using these values for δ and μ .

Summary of results for 530 and 90 kev γ -rays. The observations on ϵ and p' were made at $1/T=25 \text{ deg}^{-1}$.

γ -ray	ϵ	p'	p	δ	μ
530 kev	$+0.200 \pm 0.005$	1.164 ± 0.01	-0.136	$+0.75 \pm 0.25$	$0.44 \pm 0.06 \text{ n.m.}$
90 kev	-0.093 ± 0.005	1.054 ± 0.005	-0.055	-0.17 ± 0.15	$0.27 \pm 0.02 \text{ n.m.}$

§ 5. DISCUSSION

It will be noticed that the moment deduced from 90 kev results is smaller than that from the 530 kev results. This may be attributed to a perturbation of this state through coupling with extranuclear fields during its long lifetime ($2.44 \times 10^{-9} \text{ sec}$). Effectively this reduces $B_2(T)$ for this state relative to that of the 530 kev state by a factor λ where $\lambda=0.5 \pm 0.2$.

Our results may be compared with those of Ambler *et al.* (1955) who found a 40% anisotropy in the 530 kev radiation but no significant anisotropy for the 90 kev γ -ray. This lends support to our hypothesis that the 90 kev state is perturbed. In the light of the present experiments the absence of anisotropy cannot be caused by the E2/M1 admixture which they have suggested as the most likely explanation (Ambler *et al.* 1956). In the results for the 530 kev γ -ray there is also a discrepancy between the two sets of experiments. This can be seen by calculating the theoretical dependence of ϵ on $1/T$ in the double nitrate using the values for μ and δ obtained from the ethyl sulphate results; one finds that the experimental values of ϵ are up to a factor three times smaller at high temperatures giving rise to too low a value for the nuclear moment ($0.22 \pm 0.05 \text{ mm}$). Although the lifetime of the 530 kev state has not been measured, for an M1/E2 transition of this energy it would be expected to be in the region of 10^{-11} second which is too short for a sizeable perturbation to occur. A more probable explanation for the discrepancy lies

therefore in some ionic effect, e.g. dipole-dipole interaction. The existence of this discrepancy does not however influence the conclusion about the mixing ratios for the γ -ray transitions, since these are based upon simultaneous measurements of ϵ and p' and do not depend upon $B_2(T)$.

Since the possibility of reduction of the anisotropy of the 530 kev radiation cannot be excluded 0.44 ± 0.06 nuclear magnetons must be regarded as a lower limit for the magnetic moment of ^{147}Nd .

§ 6. CONCLUSIONS

The 530 kev level of ^{147}Pm has a spin $7/2^+$ and decays to the ground state with the emission of a mixture of M1 and E2 radiations in the proportions given by $\delta(E2/M1) = +0.75 \pm 0.25$. The γ -ray from the 90 kev state ($7/2^+$) is principally M1 with $\delta(E2/M1) = -0.17 \pm 0.05$. Assuming that the spin of ^{147}Nd is $9/2$ the magnetic moment is 0.44 ± 0.06 nuclear magnetons. The 90 kev level appears to be perturbed in both neodymium cerium magnesium nitrate and in neodymium ethyl sulphate. The attenuated angular distribution in the latter salt has $\lambda = 0.5 \pm 0.2$.

ACKNOWLEDGMENTS

We wish to express our thanks to Lord Cherwell and to the late Professor Sir Francis Simon for their interest in this work. We are very grateful to Dr. N. Kurti for his helpful advice and encouragement in these experiments.

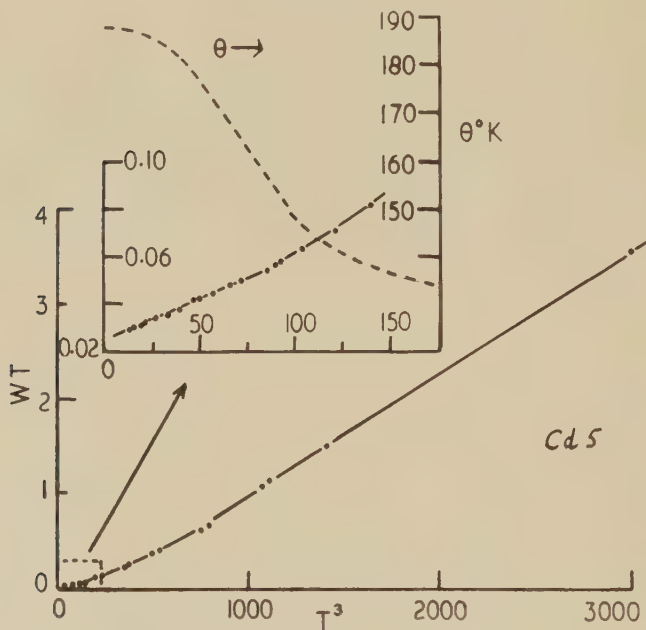
REFERENCES

- AMBLER, E., HUDSON, R. P., and TEMMER, G. M., 1955, *Phys. Rev.*, **97**, 1212 ; 1956, *Ibid.*, **101**, 196.
 BEIDENHARN, L. C., and ROSE, M. E., 1953, *Rev. Mod. Phys.*, **25**, 729.
 BISHOP, G. R., and PEREZ Y JORBA, J. P., 1955, *Phys. Rev.*, **98**, 89.
 BLEANEY, B., 1951, *Phil. Mag.*, **42**, 441.
 BLEANEY, B., 1955, *Proc. Phys. Soc. A*, **68**, 937.
 BLEANEY, B., SCOVIL, H. E. D., and TRENAM, R. S., 1954, *Proc. Roy. Soc. A*, **223**, 15.
 CACHO, C. F. M., GRACE, M. A., JOHNSON, C. E., KNIPPER, A. C., SCRULOCK, R. G., and TAYLOR, R. T., 1955, *Phil. Mag.*, **46**, 1287.
 GRAHAM, R. L. and BELL, R. E., 1953, *Canad. J. Phys.*, **31**, 377.
 MEYER, H., 1957, *Phil. Mag.*, **2**, 521.
 MURAKAWA, K., 1954, *Phys. Rev.*, **93**, 1232.

good representation (e.g. see Rosenberg, 1955). Nevertheless earlier work indicated that in some cases (2) was not very accurate, i.e. α was not constant at low temperatures. Hulm's (1950) results on mercury show this very clearly.

The present work deals with a similar situation in measurements on cadmium and zinc and for these metals, at least, a satisfactory explanation can be presented in terms of the variation of the Debye θ at low temperatures.

Fig. 1



A plot of WT against T^3 for the cadmium crystal showing the breakaway from the straight line at low temperatures. The inset shows the low temperature end of the graph on a larger scale and illustrates the fact that in this range the WT curve becomes linear once more. Also shown in the inset is the variation of the Debye θ with temperature.

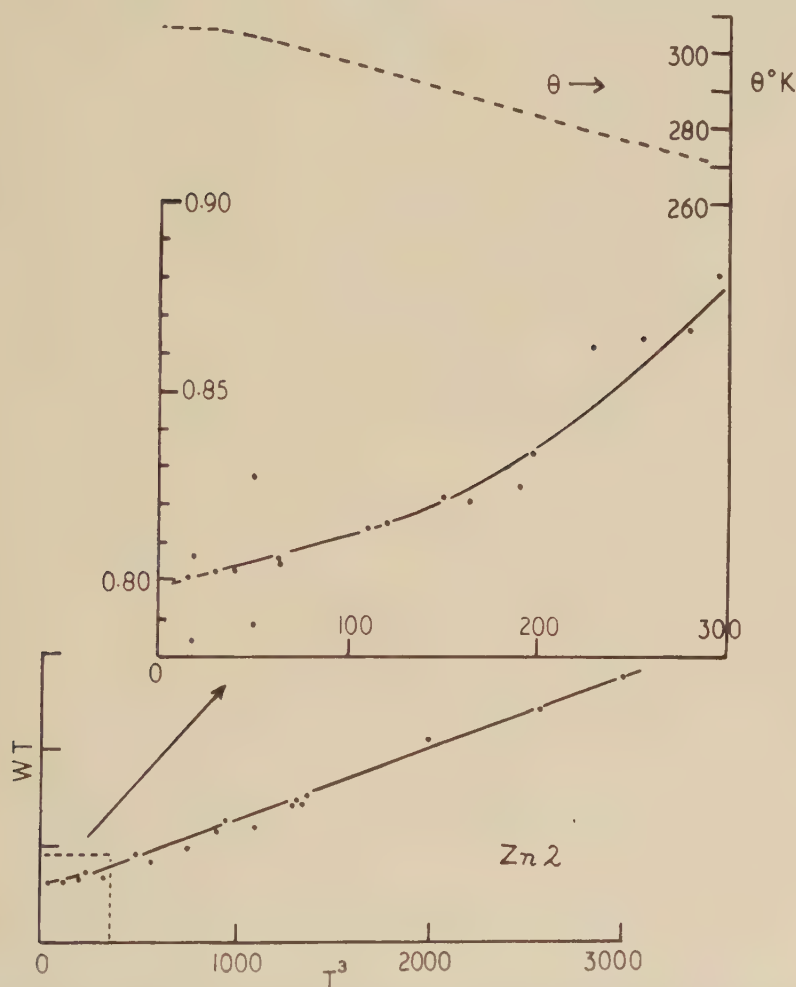
§ 2. EXPERIMENTS AND SPECIMENS

The thermal conductivity was measured between 2 and 20°K. The general technique using gas thermometers to measure the temperature difference has already been published (Rosenberg 1955). All the specimens were single crystals. Several cadmium specimens of different orientations were measured, all made from the same batch of Hilger VPS 8670, with a stated purity of 99.995%. Except for a slight anisotropic effect, they all gave similar results and hence only one set will be presented in detail in this paper. One zinc crystal was measured. This was made from 99.997% purity metal supplied by the Imperial Smelting Corporation, Avonmouth.

§ 3. RESULTS

The results are plotted as curves of WT against T^3 . Those for cadmium (Cd5) are given in fig. 1 which shows that over the higher temperature range the WT curve is linear, but that it tends to decrease in slope at

Fig. 2

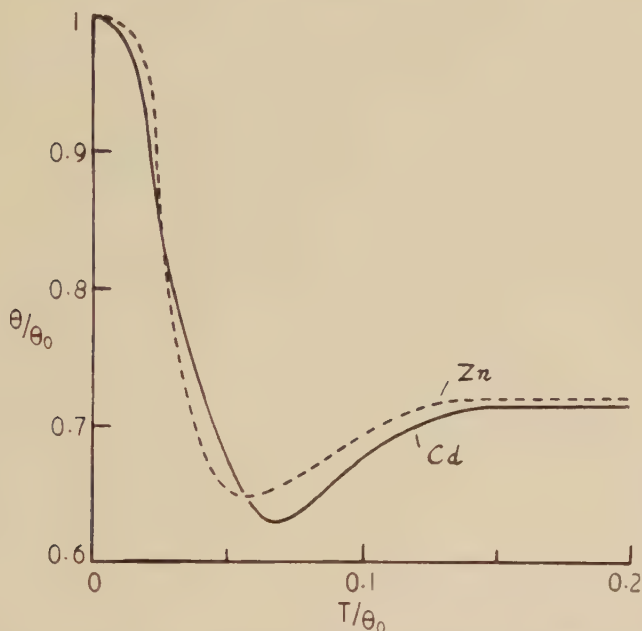


A plot of WT against T^3 for the zinc crystal. The inset shows the low temperature section on a larger scale, together with the variation of the Debye θ over that range.

lower temperatures. The inset to fig. 1 however, shows that up to $T^3=80$ the WT curve is once again linear but its slope is only one quarter of that of the linear section which occurs at the higher temperatures. This means that we have two possible values of α for the high and low temperature ends of the WT curve, which we can designate α_H and α_L respectively.

Debye theory. This will therefore give a higher specific heat than the Debye theory, i.e. the effective θ will be smaller. If eqn. (3) is valid, therefore, it is not surprising that the slope of the WT curve changes and that there is more than one apparent value for α . It is therefore suggested that the increase in slope at the end of the α_L region is a reflection of the rather sharp decrease in θ which occurs at about the same temperature. The values of θ for cadmium (Smith and Wolcott 1956) and zinc (Smith 1955) are plotted on the WT curves of figs. 1 and 2. If one takes as a criterion that a departure from linearity can be detected when the slope

Fig. 3



The dependence of the reduced Debye θ on the reduced temperature for zinc (Smith 1955) and cadmium (Smith and Wolcott 1956). $\theta_0=305^\circ\text{K}$ for zinc and 188°K for cadmium.

of the WT curve (i.e. α) has changed by 10% , then if (3) is correct, this corresponds to a change in θ of about 2.5% †. Such a change from θ_0 has occurred by 3.5°K for cadmium and by 5°K for zinc. These temperatures agree quite well with those at which the WT curves cease to be linear—about 4°K for cadmium and 5°K for zinc.

If one assumes that the low temperature, constant value of θ , θ_0 , should be used for α_L , and that α_H corresponds to the region where θ has ceased to fall rapidly, i.e. around its minimum value, θ_{\min} , then from (3) we have

$$\alpha_H/\alpha_L = (\theta_0/\theta_{\min})^4. \quad (4)$$

† Since K_∞ is proportional to θ^2 , α is proportional to θ^{-1} . I am grateful to Dr. P. G. Klemens for pointing this out.

From the work already quoted $(\theta_0/\theta_{\min})^4$ for both cadmium and zinc is about 5. This value is similar to that for the ratio α_H/α_L given in the table and is probably as good as one could expect because α_H becomes constant over a range where θ is still changing although less rapidly than at lower temperatures.

The above discussion shows quite clearly that the change of slope of the WT curves is bound up with the variation in the Debye θ . Nevertheless it should be emphasized that one must not expect complete agreement between α and θ . In the first place it is still uncertain as to whether one should use the specific heat θ in (3). Blackman (1951) has suggested that one should use a value, θ_L , which is associated with the longitudinal lattice vibrations only, since the Bloch theory only assumes interaction with the longitudinal vibrations. Ziman (1954) also assumes this in his development of the theory. The experiments of Kemp *et al.* (1956) on the other hand indicate that the electrons do, in fact interact with lattice vibrations of all polarizations. However, whichever θ is used, it is probable that it would follow the same trend as the value derived from specific heat measurements.

There is, however, a more important aspect which is sometimes overlooked. The θ , as it appears in the conductivity theory, is not an expression of the specific heat as such. It arises from the calculation of the interaction of the electrons with the lattice vibrations and the averaging of this interaction over all lattice frequencies. The way in which this is done so as to yield a useful solution is to introduce the Debye θ , which is also obtained from an average over all lattice frequencies. The method of averaging used, however, is different in the two cases and it is unlikely that the results of these two types of averaging should give exactly the same solutions. Therefore whilst a change in one average will almost certainly correspond to a change in the other, it is unlikely that there will be exact agreement. Hence, whilst these changes in α which have been described seem to correspond quite well with the observed variation of specific heat θ , it is not surprising that exact agreement is not found for the values of α_H/α_L .

Although this paper has been concerned with cadmium and zinc where the change in θ is quite large, it seems probable that the increase in α should occur to a greater or lesser extent in all metals, depending on how great a variation there is in θ . For many metals this variation is quite small, but there are a few other cases where an effect should be observed. For mercury (Smith and Wolcott 1956) θ changes from 77° at 1°K to 50° at 3°K . This gives a value of $(\theta_0/\theta_{\min})^4$ of 5.7 which indicates that α should change considerably in this region. This is undoubtedly the cause of the non-linearity of the WT versus T^3 curves given by Hulm (1950). Since the constant value of α in this case would be below 1°K he did not find the initial linear part of the curve (corresponding to α_L) and he begins with the curved section. His straight section, however, α_H starts at about 2.5°K which is just where θ stops changing rapidly. Another case is that

of gallium where $(\theta_0/\theta_{\min})^4$ is 10 (Wolcott 1955), and the thermal conductivity results indicate that α_H/α_L is about 2 (see Rosenberg, 1955).

ACKNOWLEDGMENTS

I should like to thank Mr. S. Weintraub of the University of Southampton for supplying the zinc and cadmium single crystals. I am grateful to Dr. M. Blackman, Dr. P. G. Klemens, Dr. P. L. Smith and Dr. J. M. Ziman for valuable discussion.

REFERENCES

- BLACKMAN, M., 1951, *Proc. Phys. Soc. A*, **64**, 681; 1956, *Handbuch der Physik*, vol. 7/1 (Springer: Berlin).
HULM, J. K., 1950, *Proc. Roy. Soc. A*, **204**, 98.
KEMP, W. R. G., KLEMENS, P. G., SREEDHAR, A. K., and WHITE, G. K., 1956, *Proc. Roy. Soc. A*, **233**, 41.
KLEMENS, P. G., 1956, *Handbuch der Physik*, vol. 14 (Springer: Berlin).
OLSEN, J. L., and ROSENBERG, H. M., 1953, *Advanc. Physics*, **2**, 28.
ROSENBERG, H. M., 1955, *Phil. Trans. Roy. Soc. A*, **247**, 441.
SMITH, P. L., 1955, *Phil. Mag.*, **46**, 744.
SMITH, P. L., and WOLCOTT, N. M., 1956, *Phil. Mag.*, **1**, 854.
WILSON, A. H., 1953, *Theory of Metals*, 2nd edition (Cambridge: University Press).
WOLCOTT, N. M., 1955, *Thesis*, Oxford University.
ZIMAN, J. M., 1954, *Proc. Roy. Soc. A*, **226**, 436.

Metallography of a Medium Carbon Steel subjected to Slow and Impact Compression†

By J. D. CAMPBELL, J. DUBY‡
Engineering Laboratory, University of Oxford

and

K. E. PUTTICK,
H. H. Wills Physics Laboratory, University of Bristol

[Received November 29, 1956]

ABSTRACT

Specimens of medium carbon steel subjected to slow and dynamic compression have been examined by optical and electron microscopy. In slow deformation, coarse slip in ferrite occurs in very narrow regions on corrugated surfaces; this behaviour appears to be related to the presence of an ageing precipitate. Coarse slip is absent in rapidly strained steel; the metal deforms by fine slip which occasionally forms deformation bands. Deformation twins were only observed on one specimen of which the microstructure was abnormal.

§ 1. INTRODUCTION

OBSERVATIONS on the mechanism of deformation during slow and impact compression of mild steel have recently been described by Campbell and Duby (1956). It was found that the coarse, wavy slip lines which characterize plastic deformation of the α iron at normal strain rates are absent after dynamic straining, and that impact seems to cause less work hardening than slow compression. Some further metallographic observations on a medium carbon steel, made by both optical and electron microscopy, are here reported.

§ 2. EXPERIMENTAL METHODS AND RESULTS

The steel used was a medium carbon steel (M2185) of the following composition:

	C	Mn	Si	S	P
per cent	0.32	0.62	0.235	0.037	0.025

The steel was supplied in the form of $2\frac{1}{2}$ in. diameter bars. In order to avoid any segregated impurities, specimens $\frac{5}{8}$ in. in diameter were cut from the outer layers of the rod. These were stress-relieved for one hour

† Communicated by the Authors.

‡ Now at University of Alberta, Edmonton.

at 600°C, and then machined and ground to their final dimensions: 0.499 in. diameter, length 0.5 in. They were finally annealed at 850°C for 30 minutes *in vacuo* and slowly cooled. For metallographic examination flats were filed on the sides of specimens; these were ground, electro-polished and etched, before test. The method of deformation was identical with that previously described by Campbell and Duby.

The first series of specimens to be examined consisted of two cylinders which had been strained to about 4%, one in slow compression and one in impact (at an average plastic strain rate of 500 sec⁻¹), and a third which had been twice impacted to a strain of 8%.

The microscopic examination was made optically with a light profile, and carbon replicas of the surface for electron microscopy were prepared by a method previously used by Puttick (1957).

The light profile showed that the coarse slip steps developed on the slowly compressed cylinder varied widely in height, up to a maximum of about 0.5 μ as in fig. 1. (The vertical magnification is about twice the lateral magnification.) As might be expected, little sign of deformation could be seen in pearlitic areas, but large shears were observed at the boundary between pearlite and ferrite, indicating that such areas can be regarded at these strains as elastic inclusions in a matrix of plastic ferrite.

The oblique illumination required for the light profile produces a schlieren effect which shows up, rather more clearly than normal illumination, fine slip lines in the rapidly deformed specimen (though they cannot be separately resolved). It is interesting to note that under these conditions, deformation bands are occasionally formed (fig. 2). If Mott's (1953) suggestion is correct, that deformation bands are only formed by fine slip, the fact that bands are not observed on slowly strained α iron suggests that there is little or no fine slip between the coarse lines characteristic of slip in body-centred cubic metals.

The ferrite had in places a mottled appearance, such as often indicates the presence of a sub-microscopic precipitate. A section was therefore cut from one of the specimens, electrolytically polished, and anodically etched in 10% chromic acid. This preparation has been found by Puttick (1957) to reveal fine cementite particles clearly in steel, and the 'rough-cast' texture of many of the ferrite grains as in fig. 3 confirms that some kind of ageing has occurred in the α iron, probably during the furnace cooling. This section revealed a second feature worth noting, exemplified by the bright vertical line in fig. 3. As the illumination is oblique, this indicates a surface step, which on a deformed surface would naturally be attributed to shear of the ferrite between two adjacent pearlite areas. However, the metal had not been further deformed after polishing, and it is therefore concluded that the electrolytic polishing or etching has revealed some details of the previous deformation, perhaps due to strain-ageing segregation of carbon atoms to dislocations.

The condition of the ferrite and its mechanism of deformation were further elucidated by electron microscopy. Figure 4 shows a replica of

a slowly deformed ferrite grain. The points of interest are :

(i) The surface texture, confirming the existence of small etch-resistant particles.

(ii) The coarse, forked slip lines.

(iii) Slip apparently beginning on a second system, transverse to the large slip lines ; the lines are faint but seem to have a definite and fairly regular spacing.

The nature of the small particles observed in steel has recently been the subject of some controversy ; it has been asserted that they may not be true precipitates, but regions of high carbon concentration round dislocations. Such segregation could certainly lead to unusual chemical effects, as has been suggested above, but we doubt whether it is the true explanation of the surface texture of ferrite in the present case. For one thing, the particles were almost certainly present before deformation, yet their density is in many places 10^{11} – $10^{12}/\text{cm}^2$ (for instance fig. 7). This is very much higher than current estimates of numbers of dislocations in annealed metals. Also, the density of the particles is not markedly higher at grain boundaries, to which carbon atoms must certainly migrate even more readily than to single dislocations. On the whole, the surface appearance is most simply explained by homogeneous precipitation of a second phase, probably cementite, in the ferrite. After all, if such precipitation does not occur the ferrite formed in mild steel during cooling after austenitizing must be heavily supersaturated at room temperature.

The surface texture of ferrite grains makes observation of fine slip in the impacted specimens difficult, except at boundaries between grains, or between ferrite and pearlite, where the requirements of continuity may impose severe local distortion. This is, of course, the explanation of the fact that deformation of rapidly strained metals apparently occurs at grain boundaries rather than within the grains ; fine slip cannot be resolved, and only the discontinuities at grain boundaries are visible. It is quite a different process from 'grain boundary slip' which accommodates deformation at high temperatures and low rates of strain. This point is emphasized by fig. 5 in which slip steps can be seen following the boundaries of a severely deformed grain.

Some interesting characteristics of coarse slip in α iron can be discerned in fig. 6 (also of the slowly compressed specimen). This micrograph is actually one member of a stereoscopic pair, measurement of which shows that the total shear at the large slip step there visible is about 0.4μ . This slip seems to have taken place in a very narrow region ; there is no suggestion of a slip band resolvable into an aggregate of lamellae as in face-centred cubic metals such as aluminium. The step does, however, exhibit a number of striations which may reasonably be taken to indicate the slip direction. It has been suggested (Maddin and Chen 1954) that 'wavy slip' in α iron on apparently irrational planes is really the result

of intimate cross slip on elements of low index planes (such a process must indeed be the explanation of the difference between slip in face-centred cubic and body-centred cubic metals) but such cross slip has never actually been demonstrated. Here, and in similar photographs such as fig. 7, the scale of the cross slip seems to be related to the size of the precipitate particles. This seems a reasonable supposition, since if dislocations are held up by the precipitate particles as in Mott and Nabarro's (1948) model of slip in age-hardened alloys, dislocations in screw orientation would climb out of the plane of their source to surmount the barriers. It need not, of course, be supposed that a single dislocation source is responsible for the large amount of slip in figs. 6 and 7; since slip lines can branch and coalesce, the steps may well represent the total slip from a number of sources.

It is interesting to compare slip in this material with that in α iron which is apparently free from precipitate. Figure 8 is an electron micrograph of deformed free ferrite in a mainly pearlitic carbon steel, the composition, heat treatment, and deformation of which has been described elsewhere by Puttick (1957). The specimen was strained about 3% in tension. The slip lines in this case are rounded and diffuse, in marked contrast to the sharp 'shear cliffs' in figs. 6 and 7. Although the two steels are of somewhat different composition, it does seem possible that the coarse slip in figs. 6 and 7 is associated with the presence of fine cementite particles†.

An attempt was made to prepare specimens of the 0.32% carbon steel which would be completely free of precipitate. Two cylinders were austenitized in argon at 850°C, transformed at approximately 710°C in a lead bath for two hours, and air cooled. Examination of these specimens showed that the attempt was not entirely successful, but revealed some other features of interest. The microstructure of one specimen was similar to those previously examined, except that the pearlite was coarser and the precipitate was less apparent; but the other specimen had apparently suffered some surface decarburization, possibly the result of inadequate flow of argon through the furnace tube. In this specimen the grain size at the surface was much larger than in the other, and the amount of pearlite very small. Some precipitate within the ferrite was visible with the optical microscope, not randomly distributed as in the previous specimens, but in the form of a network. Electron microscopy showed that cementite had precipitated along many grain boundaries in the form of films (fig. 9) and as films or rows of fine particles along lines within the α iron (figs. 10 and 11). Some of these form a continuous network, and presumably delineate dislocation walls forming sub-boundaries; other rows of particles seem, however, to be completely isolated, and may indicate the intersection of single dislocations with the surface.

† The difference in slip behaviour cannot be attributed, as it has been in other cases, to difference in surface preparation; both steels had been electrolytically polished before etching.

Both these specimens were subjected to impact. That with normal microstructure behaved in the expected way, deforming by fine slip in the ferrite. The surface decarburized specimen, however, though showing evidence of fine slip, also exhibited a number of twins (figs. 12 and 13).

The formation of twin lamellae by impact of iron has often been reported (no doubt this is the origin of those first observed by Neumann in meteorites) but in the present tests they were only seen on this one specimen. The microstructural features suggest that the difference in behaviour is to be ascribed either to the heterogeneous precipitation of cementite within and between the ferrite grains, or to the grain size itself. It might be argued, for instance, that precipitation on dislocations has so hindered their movement, and grain boundary cementite so impeded the spread of plastic flow from grain to grain, that the critical shear stress for slip has been raised to a value at which twinning is an alternative possibility. The existence of a grain size effect in twinning has also been reported, however (e.g. Clark and Craig 1952), so that this factor cannot be disregarded. The evidence is rather vague, but does suggest that the critical shear stress for twinning may be a decreasing function of grain size. No explanation of such an effect in terms of current theories of deformation twinning, such as the pole mechanism of Cottrell and Bilby (1951), seems in sight at the moment. Further experiments on the subject are desirable.

§ 3. CONCLUSIONS

Metallographic examination of compressed medium carbon steel specimens has revealed the following points of interest :

1. In slow deformation, large amounts of slip occur in very narrow regions on corrugated surfaces. This behaviour seems to be related to the presence in ferrite of an ageing precipitate, probably cementite.
2. Fine slip in rapidly deformed specimens occasionally forms deformation bands, which have not been observed in slowly compressed specimens.
3. The strain is not homogeneous ; up to the strains of these experiments, pearlitic areas undergo little deformation. The apparent ' grain boundary movement ' previously observed by Campbell and Duby (1956) is a localized shear imposed by the requirements of continuity.
4. Deformation twinning has only been observed in one specimen, of which the microstructure was somewhat abnormal. This behaviour can be attributed either to raising of the critical shear stress for slip by precipitation of cementite on dislocations, or to lowering of the critical stress for twinning by an increase in grain size.

ACKNOWLEDGMENTS

We are grateful to Mr. A. N. Dickson of the Department of Mechanical Engineering, Bristol University, for annealing the specimens.

J. Duby is indebted to the National Research Council of Canada for the award of a Special Scholarship, and K. E. Puttick to the Royal

Society and the Armourers' and Brasiers' Company for the award of their Research Fellowship in Metallurgy.

REFERENCES

- CAMPBELL, J. D., and DUBY, J., 1956, *Proc. Roy. Soc. A*, **236**, 24.
CLARK, R., and CRAIG, G. B., 1952, *Prog. Metal Phys.*, **3**, 115.
COTTRELL, A. H., and BILBY, B., 1951, *Phil. Mag.*, **42**, 573.
MADDIN, R., and CHEN, N. K., 1954, *Prog. Metal Phys.*, **5**, 53.
MOTT, N. F., 1953, *Phil. Mag.*, **44**, 742.
MOTT, N. F., and NABARRO, F., 1948, Phys. Soc. Conference on Strength of Solids.
PUTTICK, K. E., 1957, *J. Iron and Steel Inst.*, **185**, 161.

The Magnetic Properties of Alloys having the Compositions $\text{Mn}_{60}\text{Al}_x\text{Zn}_{20-x}\text{C}_{20}$ and $\text{Mn}_{60}\text{Ga}_x\text{Zn}_{20-x}\text{C}_{20}$ [†]

By L. HOWE[‡] and H. P. MYERS[§]

Department of Mining and Metallurgy, The University of British Columbia, Vancouver, Canada

[Received November 13, 1956]

ABSTRACT

In the alloys $\text{Mn}_{60}\text{Al}_{20}\text{C}_{20}$ and $\text{Mn}_{60}\text{Zn}_{20}\text{C}_{20}$ the Bohr magneton number per manganese atom for the ferromagnetic state differs by 0.32, being greater in the zinc alloy. It was thought that this difference could be accounted for by the difference in valencies between Al and Zn, the extra valency electron of the aluminium atom over that of zinc causing a reduction of one Bohr magneton per unit cell, corresponding to 0.33 Bohr magneton per manganese atom. If this were the case then a simple variation of Bohr magneton number might be expected in the alloy system $\text{Mn}_{60}\text{Al}_x\text{Zn}_{20-x}\text{C}_{20}$.

In addition, since the alloy $\text{Mn}_{60}\text{Zn}_{20}\text{C}_{20}$ possesses a transformation at -42°C (when it becomes an antiferromagnetic substance with a complex magnetic structure) whereas the aluminium alloy shows no such transition, measurements on the quaternary alloys should illustrate how this transition is dependent on the electron concentration of the corner atom in the unit cell.

The results show a complex behaviour which points against any simple valency mechanism controlling the ferromagnetic properties. Although the lattice parameter of the quaternary alloys varies linearly with Zn-Al content, both the ferromagnetic and antiferromagnetic moments are reduced when aluminium partially replaces zinc in $\text{Mn}_{60}\text{Zn}_{20}\text{C}_{20}$. The ferromagnetic-antiferromagnetic transition moves to lower temperatures and attains 0°K for the composition $\text{Mn}_{60}\text{Al}_{5.5}\text{Zn}_{14.5}\text{C}_{20}$. For aluminium contents greater than 5.5% the alloys show only ferromagnetic properties and the saturation moment then increases with increasing Al content. However, at 10% Al the alloys contain two phases and further magnetic measurements are unrewarding.

Similar measurements over a more restricted range of composition were made on alloys of the form $\text{Mn}_{60}\text{Ga}_x\text{Zn}_{20-x}\text{C}_{20}$ and gave results in agreement with those for the Al-Zn alloys.

[†] Communicated by Professor W. Sucksmith, F.R.S.

[‡] Now at Atomic Energy of Canada Ltd., Chalk River, Ontario.

[§] Now at AB Atomenergi, Stockholm, Sweden.

§ 1. INTRODUCTION

THE alloys of composition† $\text{Mn}_{60}\text{Al}_{20}\text{C}_{20}$ and $\text{Mn}_{60}\text{Zn}_{20}\text{C}_{20}$ have many similar features. In particular they are both spontaneously magnetized at room temperature and are isomorphous, the structure being highly ordered face-centred cubic with the manganese atoms at face-centres, carbon atoms at body-centres and the remaining atom type located at the cube corner sites. The properties of these alloys have been described by Butters and Myers (1955 a, b). In spite of many similarities there is one rather striking difference; whereas the alloy $\text{Mn}_{60}\text{Al}_{20}\text{C}_{20}$ is ferromagnetic down to 4°K, the lowest temperature it has been studied (Brockhouse 1956), $\text{Mn}_{60}\text{Zn}_{20}\text{C}_{20}$ has a second order transition at -42°C . Below this temperature the structure becomes tetragonal and the magnetization decreases with decreasing temperature. This transition has been studied in detail, Brockhouse and Myers (1956), and it has been shown that below the transition temperature the alloy is antiferromagnetic possessing a complex magnetic structure. Above -42°C the alloy is a normal ferromagnetic material and extrapolation of the saturation magnetization-temperature curve (σ - T curve) together with neutron diffraction data shows the Bohr magneton number per manganese atom to be 1.58 at 0°K. The σ - T curves for Mn-Al-C alloys show the alloy $\text{Mn}_{60}\text{Al}_{20}\text{C}_{20}$ to have a Bohr magneton number per manganese atom of 1.26. Thus the Bohr magneton numbers of these two alloys differ by 0.32 per manganese atom.

It is to be noted that this difference could be accounted for by a valency effect since the aluminium alloy contains one electron per unit cell more than the zinc alloy. If this extra electron can be effective magnetically then we have a possible reason for the difference in magneton number between the two alloys because it would decrease by one the magneton value per cell, i.e. 0.33 per manganese atom and this is very close to the actual difference observed. If this were the case then we should expect to find a simple variation of Bohr magneton number with composition in the system $\text{Mn}_{60}\text{Al}_x\text{Zn}_{20-x}\text{C}_{20}$.

Such a picture involving a valency conditioned magnetization is suited to a collective electron ferromagnetism for the alloys. The rather small non-integral magneton values favour this, but on the other hand, the highly ordered structure, which is stable at high temperatures and believed to persist up to the melting point, suggests that direct bonding occurs between certain atoms, in particular the manganese and carbon atoms; this is difficult to reconcile with a collective electron model.

A further point is the presence of the transition in the zinc alloy and the antiferromagnetism which involves at least three different types of manganese atom distinguished by different and probably integral magnetic moments. Measurements on alloys having the form $\text{Mn}_{60}\text{Al}_x\text{Zn}_{20-x}\text{C}_{20}$ should illustrate how this transition is dependent upon the valency of the atom at the cube corner site.

† All compositions are referred to atomic percentages.

During the course of this work it was found that Mn-Ga-C alloys, isomorphous with those of the Mn-Al-C and Mn-Zn-C systems, also exist, but have only ferromagnetic properties. Alloys of the form $\text{Mn}_{60}\text{Ga}_x\text{Zn}_{20-x}\text{C}_{20}$ were also studied and their properties are described here.

§ 2. EXPERIMENTAL PROCEDURE

The quaternary alloys containing zinc were produced by mixing zinc fillings with crushed powder from master ternary alloys containing Mn, Al and C or Mn, Ga and C and sintering the mixtures at 600°C in evacuated quartz tubes. The product was repeatedly crushed and resintered until x-ray powder photographs showed sharp diffraction lines.

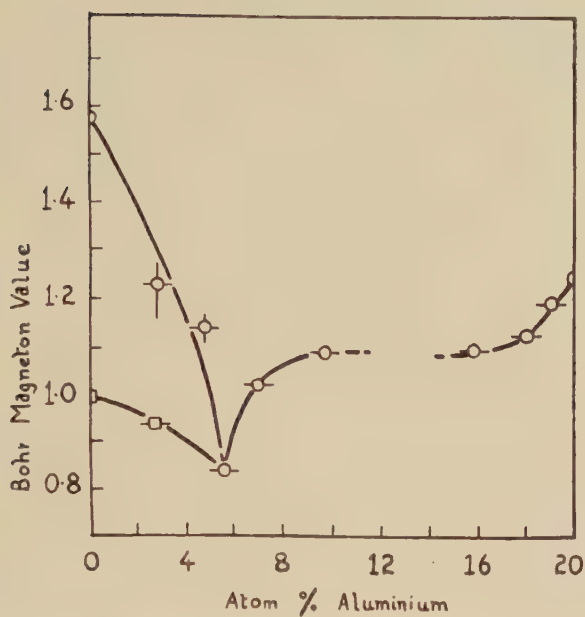
X-ray powder camera photographs were taken as a routine measure. Saturation magnetization values were obtained on coarsely crushed specimens, a magnetic field of 16 200 oersteds and a Sucksmith ring balance being used. It was established that the materials were saturated in this field strength. Measurements were made from liquid nitrogen temperature to the Curie temperatures of the alloys (usually less than 250°C).

§ 3. RESULTS

In both the Al and Ga quaternary alloy systems the highly ordered face-centred cubic structure did not occur for all values of x in the composition formula; in particular, alloys containing between 10 and 15% Al, and alloys containing more than 7% Ga consisted of two phases. Magnetic measurements were made only on single phase alloys and of these those containing more than 16% Zn showed the maximum in the σ - T curve that is characteristic of the alloy $\text{Mn}_{60}\text{Zn}_{20}\text{C}_{20}$. When such a maximum exists, provided it occurs at a temperature somewhat higher than -190°C, two values of Bohr magneton number are calculable. One value of magnetization appropriate to 0°K is obtained from the ferromagnetic range being that part of the curve determined above the transition temperature (the temperature at which the magnetization has its maximum value); this portion of the σ - T curve is extrapolated to 0°K and a value of magnetization and thereby a Bohr magneton number determined. The extrapolation is, on account of the steepness of the curve, somewhat uncertain but definite upper and lower limits to the magnetization can be set. This value we choose to call ordinary. On the other hand at temperatures below that of the transition the magnetization varies more slowly with temperature and a quite accurate extrapolation to 0°K can be made. Since, by analogy with the behaviour of $\text{Mn}_{60}\text{Zn}_{20}\text{C}_{20}$, the material is probably in a complex antiferromagnetic state in this temperature range we choose to call the magneton number so determined the 'extraordinary' value.

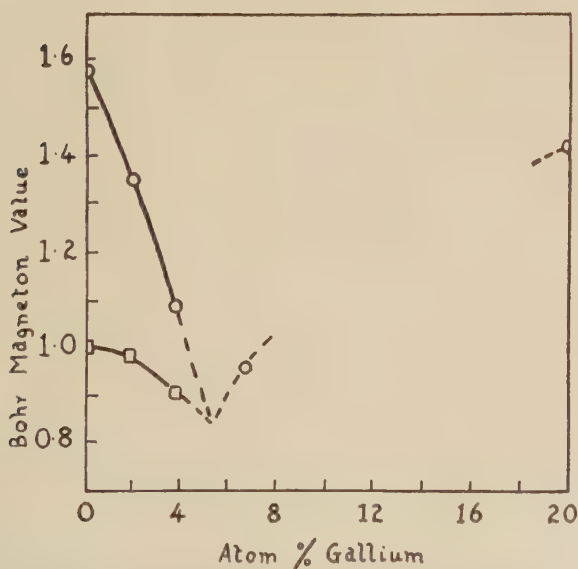
The quaternary alloys were assayed for all components. Occasionally wide departures between assayed and intended compositions were

Fig. 1



Variation of Bohr magneton numbers with composition in Mn-Al-Zn-C alloys.
 ○ ordinary value ; □ extraordinary value.

Fig. 2



Variation of Bohr magneton numbers with composition in Mn-Ga-Zn-C alloys.
 ○ ordinary value ; □ extraordinary value.

found, in such cases the alloys were discarded. Generally the assayed compositions were in good agreement with the intended compositions but, as might be expected with alloys of this kind, the total Al and Zn, and total Ga and Zn were not always exactly 20% of the whole. In these

Fig. 3

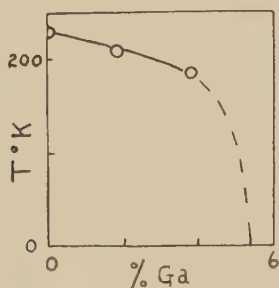
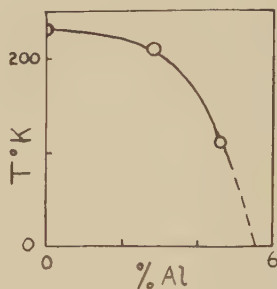
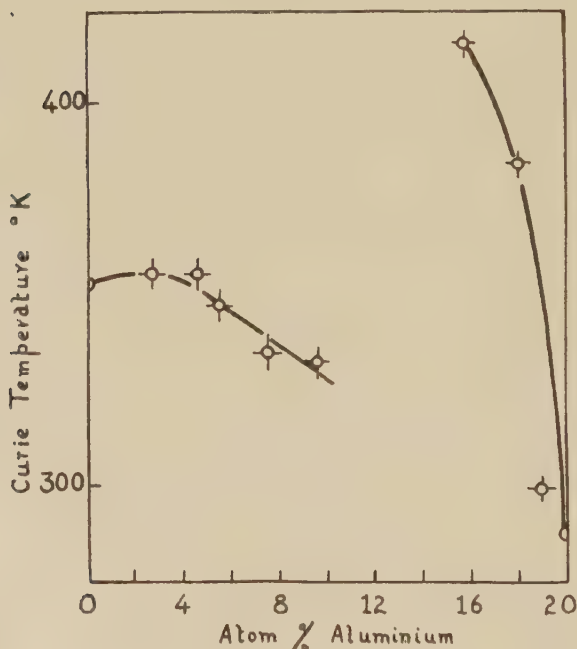


Fig. 4



Variation of transition temperature with Al and Ga content.

Fig. 5



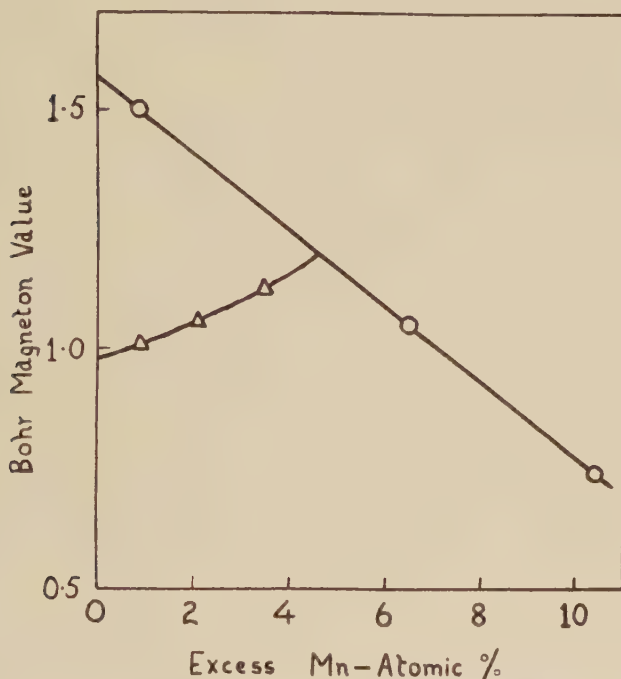
Curie temperature and composition in Mn-Al-Zn-C alloys.

cases the amounts present were scaled to 20% and in the graphs generous tolerances have been allowed as shown by the horizontal lines through the points. On account of the necessity for extrapolation and the difficulties involved in controlling the compositions of these quaternary alloys we

treat our data as semiquantitative but believe that the trend in properties shown by our results is in general correct and to have significance.

The ordinary and extraordinary Bohr magneton values per manganese atom for the two sets of alloys are plotted against composition in figs. 1 and 2. Both systems show very similar results although the data for the Ga series are more restricted than for the Al alloys. The ordinary and extraordinary magneton values are reduced, but the former more rapidly than the latter when Al or Ga replaces Zn in the alloy $\text{Mn}_{60}\text{Zn}_{20}\text{C}_{20}$. The transition temperature moves to lower temperatures as the zinc content is reduced, figs. 3 and 4. The variation of magneton numbers

Fig. 6



Variation of Bohr magneton numbers with Mn content in Mn-Zn-C alloys
 ○ ordinary value; △ extraordinary value.

with composition allows us to determine that composition for which the transition reaches 0°K for in this case both ordinary and extraordinary values are the same. This occurs at about 5.5% Al or Ga.

For aluminium contents greater than 5.5% the alloys are normal ferromagnetic materials, the magneton value then increases with increasing aluminium content until at about 10% Al the alloys contain two phases. At the aluminium rich end of the system single phase alloys are again found and the variation of magneton number seems to match very well the curve in the region of 10% Al. The variation of Curie temperature

for the Al-Zn alloys is shown in fig. 5. Room temperature lattice parameter measurements on these alloys showed the parameter to vary continuously and in a linear fashion. Similar data for the Ga-Zn alloys is limited on account of instability in this system but it is in agreement with that obtained for the Zn-Al alloys.

§ 4. DISCUSSION

It is clear that the magnetic properties of the ternary alloys $\text{Mn}_{60}\text{Al}_{20}\text{C}_{20}$ and $\text{Mn}_{60}\text{Zn}_{20}\text{C}_{20}$ are very dependent upon the electron concentration of the corner atoms in the cell, but this dependence is not due to the simple valency mechanism proposed in the earlier section of this paper.

It has been mentioned that as Al or Ga replaces Zn in $\text{Mn}_{60}\text{Zn}_{20}\text{C}_{20}$ both ordinary and extraordinary magneton numbers are decreased. This result may be compared with the behaviour of alloys of the form $\text{Mn}_{60}\text{Mn}_x\text{Zn}_{20-x}\text{C}_{20}$ where manganese replaces zinc, Butters and Myers (1955 a). In this case the ordinary magneton value is decreased whereas the extraordinary value is increased, fig. 6. The transition temperature moves to lower temperatures as in the other alloys.

These alloys show complex behaviour and we believe that much more data will be required for a proper understanding of their properties. In particular neutron diffraction measurements should prove valuable but the preparation of large homogeneous samples of quaternary alloys containing both highly oxidizable and volatile components offers considerable difficulties.

ACKNOWLEDGMENTS

The authors are grateful for financial assistance provided by the Defence Research Board of Canada and the National Research Council of Canada.

REFERENCES

- BROCKHOUSE, B. N., and MYERS, H. P., 1956, to be published.
BROCKHOUSE, B. N., 1956, unpublished.
BUTTERS, R. G., and MYERS, H. P., 1955 a, *Phil. Mag.*, **46**, 132 ; 1955 b, *Ibid.*, **46**, 895.

Climb Phenomena in Synthetic Fluorite Crystals†

By W. BONTINCK

Laboratorium voor Kristalkunde, Rozier, 6, Gent, Belgium

[Received in revised form December 12, 1956]

SUMMARY

Results of experiments in connection with climb of dislocations in fluorite crystals are given. Peculiarities of helical dislocations are explained.

Observations concerning rows of closed loops and special features are described and discussed.

Double rows of etchpits were identified with the emergence points of the parts of helical dislocations obtained by cleaving through helices.

§ 1. INTRODUCTION

ULTRAMICROSCOPIC examination of natural fluorite crystals, which had been additively coloured with sodium at 700°C, proved that dislocation lines were decorated (W. Bontinck and W. Dekeyser 1956); irregular networks and dislocation walls which resulted from slip or climb were observed. By treating synthetic CaF_2 crystals at much higher temperatures (1200°C) by a method described below, decorated helical dislocations have been found as reported in a previous note (W. Bontinck and S. Amelinckx 1957). Their relation to whisker growth as well as the nature of the colour centres in CaF_2 has been discussed in a paper by S. Amelinckx *et al.* (1957). In this paper, additional observations and properties of helical dislocations are given.

§ 2. EXPERIMENTAL PROCEDURE

The synthetic crystals of CaF_2 (Harshaw) were first coated with a thin silver layer evaporated in a high vacuum, and afterwards heated for several hours in a hydrogen atmosphere at respectively 1200° and 1100°C. The role of the silver is not clear at present and is still under investigation. It turns out that the silver layer prevents a too violent reduction of the crystal by the hydrogen; the underlying mechanism is however not clearly established. The crystals were cooled very slowly in order to enhance colloid formation.

The decorated patterns were observed by ultramicroscopy, after removal of the surface layer which contained large amounts of colloidal specks. The observation plane was the (111) plane, which is also the cleavage plane.

† Communicated by the Author.

§ 3. RESULTS AND DISCUSSION

3.1. *Properties and Peculiarities of Helical Dislocations*

As shown in a previous paper, dislocations with a mixed character can climb into regularly spaced helices with a uniform radius. Many such helices were observed which differed by their radius R and their pitch h . The table gives some measured values of h and R microns and the calculated value of x , when $\tan x = h/2\pi R$. Inspection of these values indicates that they vary between wide limits. The value of the angle x gives a measure of how densely the helices are wound.

	h (microns)	R (microns)	x
1	95	63	$13^{\circ} 30'$
2	108	54	$17^{\circ} 45'$
3	72.8	54	$12^{\circ} 5'$
4	111	55	$17^{\circ} 50'$
5	100	44	$19^{\circ} 55'$
6	44	55	$7^{\circ} 15'$
7	79	78	9°
8	166	55	$25^{\circ} 40'$

The directions of the axes of the helices were found to enclose small angles with the $\langle 110 \rangle$ directions. Next to helices with the expected characteristics, others, very irregular are also rather frequently observed.

This is probably the result of differences in the concentration of vacancies or interstitials in the vicinity of the climbing dislocations. Photograph 1 (*a*) shows a helix where two turns have climbed faster than the others. Photograph 1 (*b*) shows a helix with variable pitch and radius. We suppose that in this case the helix has been frozen in by the decoration in an energetically unfavourable position. Longer heat treatment would probably have produced a regular helix.

3.2. *Formation of Rows of Closed Loops and Special Features*

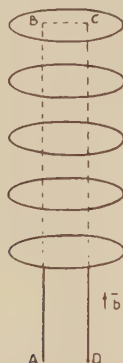
A hairpin shaped dislocation of which the longer sections have mixed (nearly screw) character can climb and produce a sequence of prismatic dislocation rings situated on the surface of a same cylinder. These rings are formed by the interaction of the two helices formed by climb of the dislocations AB and CD (fig. 1) (Amelinckx *et al.* 1957).

Decorated patterns, where only closed loops are observed, can be explained by this mechanism. In most cases, the prismatic dislocations were followed by a helical dislocation (photograph 2 (*a*)). Such patterns can be formed by two different mechanisms.

(*a*) A dislocation ABCDE consists of parts with respectively more Taylor (BC) and more screw character (AB-CE) (fig. 2 (*a*)). When

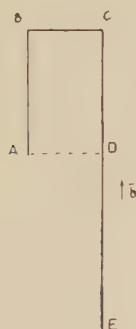
climb occurs, ABCD will act as a source of prismatic dislocations, DE will give rise to a helix, the resulting configuration is shown in fig. 2 (b). The axis of the closed loops will not coincide with the axis of the helix. The dislocation patterns on photograph 2 (b) could be the result of such a mechanism, although it was the only case where such a shift of the axis was observed.

Fig. 1

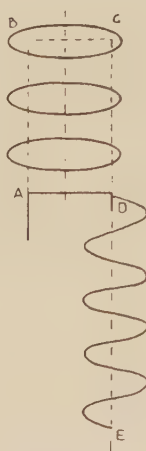


Dislocation model illustrating how a row of closed loops can be generated.

Fig. 2



(a)



(b)

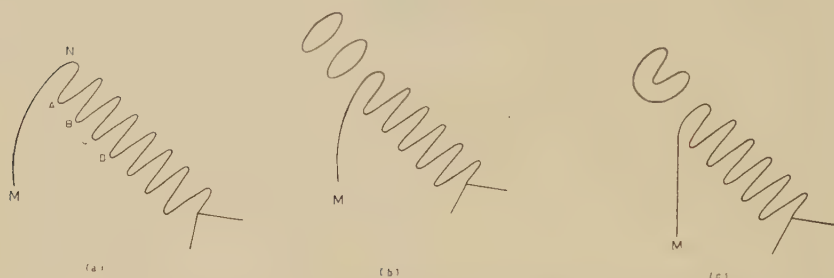
Formation of a helix, followed by a sequence of closed loops. ABCD will climb into two helices, which will interact and form a row of closed loops. DE will become a helix after climb.

(b) We have a dislocation with a *V*-shaped form, where only one part had such a character that it could climb into a helix (fig. 3 (a)). During climb of the helix the part of the dislocation MN may cut the helical dislocation in the points A, B, so that a row of closed loops results (fig. 3 (b)).

MN can however have such a form that it cuts the helix in B instead of A. A dislocation as shown in fig. 3 (c) results. Those Lissajoux like configurations were many times observed, photographs 2 (c), (d) show some examples.

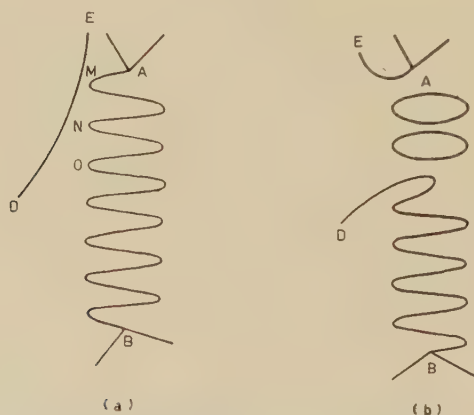
It is evident that the same mechanism can occur with a helix AB which cuts during climb a neighbouring singular dislocation which has the same Burgers vector but of the opposite sign (fig. 4).

Fig. 3



By climb only a part of a dislocation has adopted a helical shape. After intersection with the straight part, closed loops (b) and Lissajoux like configurations (c) are formed.

Fig. 4



Formation of closed loops by intersection of a helix with a singular dislocation line of the same Burgers vector and of suitable sign.

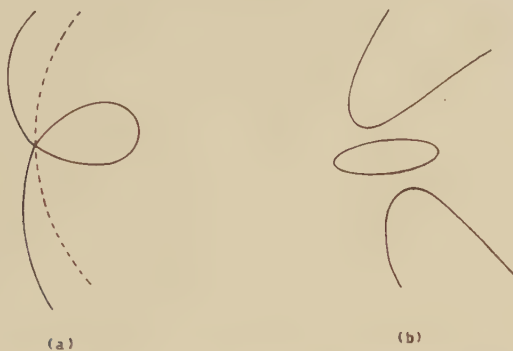
3.3. Formation of Single Loops

In many cases single closed loops were observed, they can be formed by different mechanisms (photographs 1 (a), 2 (c)).

In our crystals, helices which possess only a single winding after climb were observed (photograph 2 (e)). These features were also seen in rocksalt (Amelinckx, unpublished results). Such a dislocation can interact with another dislocation with the same Burgers vector and of

suitable sign, and give rise to a closed loop (fig. 5). A second possibility is the precipitation of vacancies in a certain region. The so formed prismatic dislocation can climb further by enlarging its radius.

Fig. 5



Formation of a single closed dislocation line, by intersection of a helical dislocation with one loop with a singular dislocation with appropriate Burgers vector.

3.4. Features Consisting of Different Helical Dislocations

When only one, two or all three dislocations forming a node are nearly pure screws one or more helices with a common endpoint will result if climb is possible. As the Burgers vectors $\langle 110 \rangle$ in the (111) plane form angles of 120° , the screw dislocations will also form angles of 120° or 60° and this angle will be preserved between the axis of the helices.

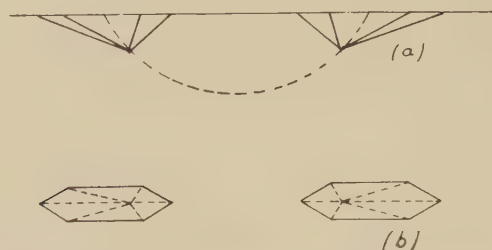
In photograph 3 two sets of helical dislocations are shown. The measured angles are 111° and 78° , which is very acceptable, because the dislocations must have screw character without being pure screw. This is probably the case for the third dislocation for it is not decorated. When the three dislocations are nearly pure screws, three helices will result after climb. This has not yet been observed.

3.5. Relation between the Etch Structure of (111) Cleavage Planes and Helical Dislocations

Fluorite crystals annealed at high temperatures were cleaved and etched. Concentrated H_2SO_4 was used as an etchant. Double rows of etchpits nearly parallel to $\langle 110 \rangle$ were many times observed. From the relative positions of the etchpits, we could deduce if it were the emergence points of a helical dislocation line or of a row of closed loops (photograph 4). The shape of the pits gives already some indication that the dislocation line has helical character. The pits are not perfectly hexagonal inverted pyramids; the bottom points of the pits of the two opposite rows are displaced towards each other (fig. 6). This proves already that the

dislocation lines are oblique to the cleavage plane and are symmetrical to the centre line between the two rows. The definite proof could be given by continued etching. Photographs 5 (a), (b), (c) show three different stages. In (c) nearly all etchpits have disappeared; the successive positions of their centres come closer and closer and finally the centres disappear, as one continues the etching. As the instantaneous position of an etchpit is always centred on the emergence points of the dislocation, this allows the unambiguous conclusion that one has to do with half loops.

Fig. 6



Relation between the shape of the etchpits and the direction of the half loops responsible for their formation.

(a) Cross section of the pits; (b) top view of the pits.

Photograph 6 (a) shows an etch pattern of two helical dislocation lines which make an angle of 115° .

Patterns of double etchpits were also observed (photograph 6 (b)) it is clear that these are the emergence points of single closed loops as after continued etching the pits came closer and closer and disappeared altogether.

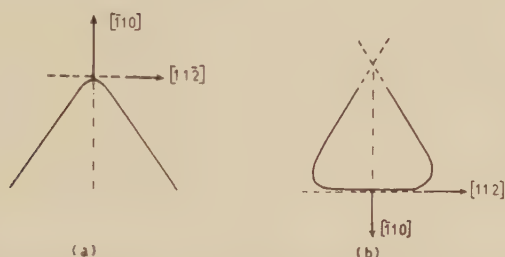
3.6. *Climb at Lower Temperatures*

At lower temperatures climb of what we think to be Taylor like dislocations was observed. We searched our crystals for decorated Bardeen-Herring sources. Photographs 7 (a), (b) show some patterns which were thought to be the first stages of a Bardeen-Herring mechanism. The most remarkable fact of lower temperature treatment was the occurrence of polygonized features. This indicates that climb at lower temperature proceeds in the anisotropic way. Photograph 8 (a), (b) show the most commonly observed feature. Photograph 8 (c) shows the first stage of a polygonized potential Bardeen-Herring source, and photograph 9 a polygonized helix seen on different levels. The bissectrices (fig. 7) of these polygonized patterns have a $\langle 110 \rangle$ direction.

These features show that climb at lower temperatures seems to proceed along preferential directions. This polygonization can be explained in a similar way as the polygonization of growth fronts in crystal growth (Amelinckx 1953). The jogs in the climbing dislocation play the role of

the kinks on a growing step. We have to differentiate between intrinsic jogs which are due to the instantaneous orientation of the line with respect to the closed packed directions and those which are generated thermally. Densely packed directions in fluorite, which are $\langle 110 \rangle$, will contain only thermally generated jogs. At a certain temperature the total number of jogs will be smallest along these directions. The climb rate will be maximum perpendicular to the least densely packed direction. $[11\bar{2}]$ is not a closely packed climb front and will climb fastest in a $[\bar{1}10]$ direction.

Fig. 7



Patterns observed in photograph 8: the preferential climb directions in a (111) plane are indicated.

At higher temperatures, the amount of thermally generated jogs will increase and the differences of climb velocities for different directions will be suppressed.

3.7. Miscellaneous Features

Interaction with other dislocations can also influence the shape of a helical dislocation. Photograph 10 shows some examples. In (a) two turns have come very close, this is normally impossible because of the high repulsion between two successive windings. In photograph 10 (b) we can see some features probably resulting from interaction.

ACKNOWLEDGMENTS

I wish to thank Professor F. Seitz, Professor W. Dekeyser and Dr. S. Amelinckx for their continuous interest and useful discussions.

This work is part of a research programme supported by I.R.S.I.A. (Institut pour l'encouragement de la Recherche Scientifique dans l'Industrie et l'Agriculture : Comité pour l'étude de l'état solide).

REFERENCES

- AMELINCKX, S., BONTINCK, W., DEKEYSER, W., and SEITZ, F., 1957, *Phil. Mag.*, **2**, 355.
- AMELINCKX, S., 1953, *J. Chim. Phys.*, **50**, 45.
- BONTINCK, W., and AMELINCKX, S., 1957, *Phil. Mag.*, **2**, 94.
- BONTINCK, W., and DEKEYSER, W., 1956, *Physica*, **22**, 595.

CORRESPONDENCE

Multipole Order of Lattice Cells of Ionic Crystals

By F. G. FUMI and M. P. TOSI

Cattedra di Fisica Teorica dell'Università, Palermo, Italy

[Received October 12, 1956]

LATTICE cells are neutral and thus act as multipoles. Here we determine the power of the distance with which the electrostatic potential decreases (effective multipole order) for some cubic lattice cells of the most common cubic ionic structures, but the method that we use is of general applicability. The problem of the multipole nature of lattice cells of ionic crystals had already been touched upon by Evjen (1932), but his treatment is not complete nor physically transparent, and his results are improperly quoted in the standard review article by Born and Goeppert-Mayer (1933). In particular, Born and Goeppert-Mayer imply that the effective multipole order of a lattice cell of a given structure depends only on the structure, while we shall see that it depends also on the cell. We shall also see that the results quoted by Born and Goeppert-Mayer are valid for the Evjen cells of the NaCl and CsCl structures (Evjen 1932), but not for the Evjen cell of the Zincblende structure (Evjen 1932).

Let us consider a set of charges e_i with position vectors \mathbf{r}_i with reference to a point C , which compose a neutral lattice cell of an ionic crystal. To analyze the potential that this cell generates in a distant point P we use the multipolar expansion

$$\sum_i \frac{e_i}{R_i} = \sum_x \sum_i e_i x_i \left(\frac{\partial}{\partial x_i} \frac{1}{R_i} \right)_{\mathbf{R}_i = \mathbf{R}} + \frac{1}{2} \sum_{x,y} \sum_i e_i x_i y_i \left(\frac{\partial^2}{\partial x_i \partial y_i} \frac{1}{R_i} \right)_{\mathbf{R}_i = \mathbf{R}} + \dots \quad (1)$$

where \mathbf{R} is the position vector of point C with reference to point P and $\mathbf{R}_i = \mathbf{R} + \mathbf{r}_i$. $\sum_i e_i x_i$, $\sum_i e_i x_i y_i$ and so on are the components of the multipole moments of the cell, which transform as polar tensors of rank 1, 2 and so on. To determine the multipole order of the cell, it is sufficient to consider its multipole moments with reference to its volume centre. The dipole term is not always zero in eqn. (1) (Kittel 1953), as Evjen supposed. It is certainly zero with the other terms of eqn. (1) which contain even powers of $1/R$ if one chooses a cell with an inversion centre, since then the cell cannot have any multipole moment represented by a polar tensor of odd rank. The dipole term vanishes also, with the quadrupole term, if the cell has cubic symmetry: indeed in this case the diagonal

components of the quadrupole moment are equal and the non-diagonal components are zero with the dipole components, while $1/R_i$ satisfies Laplace equation. Thus, for cells of cubic symmetry without an inversion centre the first term in the multipolar expansion of the potential which may be different from zero is the term in $1/R^4$; for cells of cubic symmetry with an inversion centre the first non-vanishing term can be the term in $1/R^5$. A closer analysis is necessary to decide whether these terms, for a given lattice cell, are actually different from zero.

Let us consider, for instance, the Evjen lattice cell of the NaCl structure (Evjen 1932), which has cubic symmetry with an inversion centre (point group $m\bar{3}m$). The direct-inspection method (Fumi 1952) allows one to see at once that for cubic symmetry the only non-vanishing components of the fourth-rank polar tensor which enters the term in $1/R^5$ of eqn. (1) are $x^4=y^4=z^4$ and $x^2y^2=y^2z^2=z^2x^2$. For the cell in question one has $\sum_i e_i x_i^4 = \sum_i e_i x_i^2 y_i^2 = 0$, since its faces and edges are neutral. Thus its electrostatic potential does not go as $1/R^5$: it goes actually as $1/R^7$ since $\sum_i e_i x_i^2 y_i^2 z_i^2 \neq 0$. On the other hand, for the Højendahl lattice cell of the NaCl structure (Højendahl 1938), which does not have an inversion centre (point group $\bar{4}3m$), the electrostatic potential goes as $1/R^4$, since $\sum_i e_i x_i y_i z_i \neq 0$.

Similarly, the electrostatic potential of the Evjen lattice cells for the CsCl (Evjen 1932) and CaF₂ structures (point group $m\bar{3}m$) goes as $1/R^5$ since $\sum_i e_i x_i^4 \neq 0$, and that of the Evjen lattice cells for the Zincblende (Evjen 1932) and cuprite structures (point group $\bar{4}3m$) goes as $1/R^4$ since $\sum_i e_i x_i y_i z_i \neq 0$.

The method that we have used to determine the effective multipole order of lattice cells of ionic crystals can obviously be used also to determine the effective multipole order of the Wigner-Seitz neutral polyhedra which enter Frank's method of lattice summation (Frank 1950). One finds at once that the potential decreases with the fifth power of the distance both for the Wigner-Seitz cubes considered by Frank for the NaCl structure, and for the Wigner-Seitz truncated octahedra that one may consider to extend Frank's method to the CsCl structure (Fumi and Tosi, to appear).

REFERENCES

- BORN, M., and GOEPPERT-MAYER, M., 1933, *Handbuch der Physik*, 24 (2), 713f. (Berlin: Springer).
 EVJEN, H. M., 1932, *Phys. Rev.*, **39**, 675.
 FRANK, F. C., 1950, *Phil. Mag.*, **41**, 1287.
 FUMI, F. G., 1952, *Acta Cryst.*, **5**, 44.
 FUMI, F. G., and TOSI, M. P., *The Theory of Ionic Crystals*, to appear in *Solid State Physics* (New York: Academic Press).
 HÖJENDAHL, K., 1938, *Kgl. Danske Videnskab. Selskab., Math. fys. Medd.*, **16**, (2), 135.
 KITTEL, C., 1953, *Introduction to Solid State Physics* (New York: Wiley), pp. 113, 117.

Quenching Vacancies in Aluminium

By F. J. BRADSHAW and S. PEARSON
Royal Aircraft Establishment, Farnborough

[Received January 2, 1957]

Using the same techniques as for previous work on platinum and gold (Bradshaw and Pearson 1956, 1957) we have quenched 'superpure' (99.995%) aluminium wires of 0.2 mm diameter from temperatures between 360°C and 530°C into water at $\sim 2^\circ\text{C}$. The changes of resistance caused by quenching and annealing were measured in liquid nitrogen and are interpreted as being due to vacancies.

In this work, owing to difficulties in welding aluminium to itself, the potential leads used to determine the resistance of the specimen were of 0.02 mm diameter gold and not aluminium. But the annealed resistance remained virtually constant throughout the experiments and we are satisfied that the contamination of the specimen with gold was quite negligible. For temperatures up to 470°C the relation

$$\Delta\rho_0 = 1240 \exp(-0.76/kT) \mu \text{ ohm cm}$$

could be fitted, where $\Delta\rho_0$ is the increase in resistivity resulting from quenching and T is the absolute temperature (kT expressed in ev). The error in the vacancy formation energy is thought to be about ± 0.04 ev. At temperatures above 470° the quenching was not rapid enough to retain all the vacancies. If in the absence of theoretical calculations for aluminium we assume that the effect of 1% of vacancies will be comparable to that calculated in Cu, Ag or Au ($\sim 1.5 \mu \text{ ohm cm}$), then the vacancy concentration in aluminium was $8 \exp(-0.76/kT)$ giving $\sim 6 \times 10^{-4}$ at the melting point.

The resistivity was annealed out at temperatures between -10° and $+40^\circ\text{C}$ (at 20°C the annealing time constant was ~ 4 min). The annealing curve shapes were similar to those found in gold (i.e. approximately those of second-order reactions) and there were indications of an increase in annealing rate with increasing $\Delta\rho_0$. The activation energy for annealing was found to be 0.444 ± 0.03 ev and the mean value of nB when the resistivity increase had been reduced to $\Delta\rho_0/2$ was 6×10^{-10} where n is the probability per jump that a vacancy is lost and B is the entropy factor for vacancy migration. Since B is thought to be between 1 and 10, the average number of jumps made by a vacancy before it vanished was $\sim 10^{10}$. The grain size of the wire was roughly equal to the wire diameter from which it can quickly be shown that the grain boundaries and surfaces were not important as sinks for vacancies.

From oscillograph camera records the initial quenching rates were found to be $\sim 30^\circ/\text{m sec}$ for all quenching temperatures and the total time to reach 2°C was between 15 and 22 m sec depending on quenching

temperature. As in the previous papers we may calculate from this and the annealing rate the transition temperature above which some vacancies should be lost because of insufficiently fast quenching. This agreed within the limits of error with the transition temperature estimated from the experimental variation of $\Delta\rho_0$ with temperature.

Adding the formation and movement energies we get 1.2 ev for the activation energy for self-diffusion. Nowick (1951) has predicted 1.43 ev but Seymour (1953), using resonance methods, has measured 0.91 ev.

REFERENCES

- BRADSHAW, F. J., and PEARSON, S., 1956, *Phil. Mag.*, **1**, 812; 1957, *Ibid.*, **2**, 379.
 NOWICK, A. S., 1951, *Phys. Rev.*, **22**, 1182.
 SEYMOUR, E. F. W., 1953, *Proc. Phys. Soc. A*, **66**, 85.

The Influence of Retardation on the London-Van der Waals Force

By M. R. AUB, E. A. POWER AND S. ZIENAU
 University College, London

[Received January 23, 1957]

IN a recent issue J. W. Leech has published a perturbation calculation of the retarded interaction between two atoms (Leech 1955). He concluded that the interaction energy at large distances varied as R^{-3} in disagreement with a previous result of Casimir and Polder (1948). Large distance in this context means more precisely $R \gg \lambda$, where λ is the wavelength of the light emitted by one of the two identical atoms in its downward transition from the lowest excited state. On the other hand Casimir and Polder find that the usual London attractive energy proportional to R^{-6} for $R < \lambda$ goes over to one proportional to R^{-7} at $R \gg \lambda$ which has recently found provisional experimental confirmation (Derjaguin *et al.* 1956; Prosser and Kitchener 1956).

In this problem the only physical dimensions, apart from h and c , are the distance R , the static polarizability α of the neutral atom and λ in the simplest model. An energy proportional to R^{-6} will therefore vary like λ^{-1} , one proportional to R^{-7} will only contain λ in so far as it enters into α and one varying like R^{-3} must be proportional to λ^{-1} . If this is considered in conjunction with the fact that the R^{-3} energy law is claimed for $R \gg \lambda$, one sees that Leech's result has an unphysical behaviour.

We have therefore recalculated the retarded force by the conventional stationary perturbation method using the interaction Hamiltonian

$$H = q_i^1 q_j^2 (\delta_{ij} - 3\hat{R}_i \hat{R}_j) / R^3 + \sum_{l=1,2} \left\{ -\frac{e}{mc} p_i^1 A_i(l) + \frac{e^2}{2mc^2} A_i^2(l) \right\} \quad (1)$$

in dipole approximation, identical to that employed by Leech and by Casimir and Polder. We report disagreement with Leech, and obtain by

this symmetrical method the result of Casimir-Polder in closed form. The leading term in an expansion in powers of λ/R is given by

$$\Delta E = -16\pi^2 \langle q^1 \rangle^2 \langle q^2 \rangle^2 \lambda^2 / \hbar c \\ \times \sum_{\mathbf{k}, \mathbf{w}} \left\{ \frac{kw}{k+w} (\hat{k}_i \hat{w}_i)^2 - \frac{k^2}{k+w} \right\} \exp [i(k+w)_j R_j] = - \frac{23\lambda^2 \langle q^1 \rangle^2 \langle q^2 \rangle^2}{\pi R^7 \hbar c}. \quad (2)$$

The error in Leech's work can be traced to his evaluation of the expectation value

$$\langle 0 \left| \frac{e^2}{2mc^2} A^2(1) \frac{1}{-H_0} \frac{e^2}{2mc^2} A^2(2) \right| 0 \rangle \quad . \quad . \quad . \quad . \quad . \quad (3)$$

which equals

$$-8\pi^2 \langle q^1 \rangle^2 \langle q^2 \rangle^2 / (\lambda^2 \hbar c) \sum_{\mathbf{k}, \mathbf{w}} [1 + (\hat{k}_i \hat{w}_i)^2] \frac{\exp [i(k+w)_j R_j]}{kw(k+w)} \quad . \quad (4)$$

and although giving rise to an R^{-3} dependence, this term cancels exactly with the leading terms of the remaining transverse photon contributions.

That this method of evaluating the energy shift in lowest order $\sim (e^4)$ for two neutral atoms in interaction with the radiation field gives the same result as Casimir and Polder's elegant but unsymmetrical procedure is to be expected on general grounds.

Equation (2) can be obtained in a particularly straightforward manner with the aid of the reduced interaction Hamiltonian

$$H = - \sum_{l=1,2} q_i^l E_i(l) \quad . \quad . \quad . \quad . \quad . \quad (5)$$

where E_i is the transverse electric field operator.

REFERENCES

- CASIMIR, H. B. G., and POLDER, D., 1948, *Phys. Rev.*, **73**, 360.
 DERJAGUIN, B. V., ABRIKOSOVA, I. I., and LIFSHITZ, E. M., 1956, *Quart. Rev.*, **10**, 295.
 LEECH, J. W., 1955, *Phil. Mag.*, **46**, 1328.
 PROSSER, A. P., and KITCHENER, J. A., 1956, *Nature, Lond.*, **178**, 1339.

REVIEWS OF BOOKS

Irradiation of Colours and Luminescence. By K. PRZIBRAM. (Pergamon Press.) [Pp. 266+48 bibliography.] Price 63s.

THIS book gives an account of the coloration occurring in crystals as a result of exposure to different types of radiation, in particular those resulting from radioactivity. The associated luminescent properties are also dealt with. Part I discusses general aspects of coloration, especially in alkali halides, with emphasis on the structure sensitive properties, and includes some account of current transfer processes, the colour of glasses, and the effects of colloidal particles. Luminescence and radio-luminescence are also briefly treated.

Part II deals with the colours and luminescence encountered in natural minerals, with special reference to rock salt and fluorite, and the part played by radiation in producing the effects. The impurities present in the crystals, and the sources of the radiation leading to colour and luminescence in natural minerals are also considered.

The interpretation of the many detailed observations in terms of present ideas about colour centres and luminescence avoids the presentation of a mere catalogue of information, though here and there the escape from this a very narrow one. There is an extensive bibliography, dealing with the literature up to 1954.

This book will be of general interest to the mineralogist and physicist, but is unlikely to compete at a specialist level with books already available dealing specifically with alkali halides, luminescent materials and radiation damage.

Mathematics for Electronics with Applications. By HENRY M. NODELMAN and FREDERICK W. SMITH. (McGraw-Hill Book Company, Inc.) [Pp. 391.] Price 52s. 6d.

IN planning this book, the authors have made an analysis of the mathematical content of a number of journals in the field of electronics to determine the incidence and importance of various mathematical processes. The subjects covered are based on this survey and include dimensional analysis, determinants, matrices, series and the solution of differential equations by both classical and Laplace transform methods. In addition, an outline of Boolean algebra is given and some practical examples of the use of calculus are included.

Each subject is presented in two sections. The first is a concise and lucid exposition of the mathematical processes with illustration by worked numerical or abstract examples and the second is the application of the processes to specific electronic problems, again with a number of worked examples and related problems. Much of the practical material is taken from journals to which reference is made so that the reader may determine the context in which a particular problem has arisen.

The clear way in which the authors have presented their subject and the constant recourse to practical problems for illustration will make this book of value to both the student who intends to specialise in electronics and the more experienced scientist who wishes to have at his disposal a number of labour-saving mathematical tools, especially fashioned for the solution of electronic problems.

H. V. BECK.

Lectures on Rock Magnetism. By P. M. S. BLACKETT. (Weizmann Science Press of Israel, Jerusalem.) [Pp. 131.] Price \$5 (Israeli).

Rock magnetism is a subject touching on many fields of research in geology, geophysics, physics, mineralogy and chemistry. It has attracted increasing attention in the last ten years but is, as yet, little known and in a stage of rapid growth in which a textbook is out of place. Professor Blackett's book does not claim to be a textbook but is a valuable account of the attitude and approach of one of the foremost minds of present day physics to a new and enthralling study.

The possibilities of rock magnetism are discussed as well as the results to date and the problems which have arisen in connection with polar wandering, continental drift and the reversal of the geomagnetic field. Naturally, in a somewhat personal book of this kind, the main emphasis is placed on the work of the author's own laboratory but other contributions from many parts of the world are discussed and references quoted. Details are given of apparatus designed to meet some of the rather unusual requirements in these investigations.

The book will prove valuable both to workers within the field and, more particularly perhaps, in stimulating the interest of those in other fields. This stimulation should be of mutual advantage for, while the possible applications of rock magnetism are very wide, its study correspondingly requires techniques and ideas from many different bordering disciplines.

J. H. P.

Les Moments Dipolaires. By J. BARRIOL. (Paris: Gauthier-Villars.) [Pp. 186.] Price: Unbound 3000 fr.; Bound 3300 fr.

THE contents of this excellent book are much wider than the title suggests. Besides treating the connection between dipolar moment and structure of molecules, it contains an up-to-date survey of the theory of dielectric constant and loss, as well as chapters on the dielectric properties of solids, and on experimental methods. In a subject in which so much incorrect theoretical work is done, the author has succeeded in presenting a correct and well-balanced picture. This book can be strongly recommended to physicists, chemists and engineers.

H. F.

Digital Calculating Machines. By G. A. MONTGOMERY. (Glasgow: Blackie and Son Limited.) [Pp. 262.] Price 30s.

THE title of this book tells the strict truth, but it might lead some readers to expect a treatise devoted exclusively to modern electronic digital computers. In fact, most of the book deals with desk calculating machines: punched card machines are dealt with in a single chapter, another chapter contains a description of the earlier electromechanical automatically sequenced machines, and the two final chapters deal respectively with the logical design of, and programming for, electronic sequenced machines.

The author's method in the earlier chapters is to divide machines into groups according to their type, and to give for each group a description of typical mechanisms, followed by a detailed discussion of the operating procedures appropriate to that group. Some readers may feel that the operating procedures are discussed in excessive detail, particularly as the author is concerned with operating pure and simple, and not with numerical analysis or with the overall planning of large-scale computations. Most

computers pick up their technique on the job, learning from others more experienced than themselves: in some ways the present book is of the 'teach yourself' type, adapted to the use of those who are denied such opportunities. The last chapter on programming for electronic digital computers, brief as it is, contains a sound introduction to the subject.

The author is, undoubtedly, well-qualified in the field he covers, but the words 'Member of the Association for Computing Machinery', proudly displayed by the publisher on the dust-cover, can hardly be said to prove this, since that admirable Association is open to all who are interested in the subject, regardless of their qualifications.

M. V. W.

BOOK NOTICES

The Plastic Methods of Structural Analysis. By B. G. NEAL. (London: Chapman and Hall.) [Pp. xi+353.] Price 45s.

Transactions of the Symposium on Partial Differential Equations held at the University of California at Berkeley from June 20 to July 1, 1955. Edited by A. ARONSZAJN, A. DOUGLIS and C. B. MORREY, JR. (New York and London: Interscience Publishers.) [Pp. vi+334.] Price \$6.50.

Elements of Pure and Applied Mathematics. By H. LASS. (London: McGraw-Hill.) [Pp. xi+491.] Price 56s. 6d.

The International Journal of Applied Radiation and Isotopes. Volume 1, numbers 1/2. July 1956. (New York and London: Pergamon Press.) [Pp. (in this issue) 144.] Price per volume for private subscribers £3 10s.

Scientific Inference. 2nd Edition. By SIR HAROLD JEFFREYS. (Cambridge: University Press.) [Pp. viii+236.] Price 25s.

Year Book of the Physical Society. (London: The Physical Society.) [Pp. 76.] Issued free to Members; price to non-members 10s.

Annual Review of Nuclear Science. Volume 6, 1956. Edited by J. G. BECKERLEY, M. D. KAMEN and L. I. SCHIFF. Palo Alto (California: Annual Reviews, Inc.) [Pp. 471.] Price (postpaid in U.S.A.) \$7.00; (postpaid outside U.S.A.) \$7.50.

Table of the Fresnel Integral to Six Decimal Places. Compiled by T. PEARCEY. (Cambridge: University Press.) [Pp. 63.] Price 12s. 6d.

Interpolation and Allied Tables. Prepared by H.M. Nautical Almanac Office. (London: Her Majesty's Stationery Office.) [Pp. 80.] Price 5s.

Irrational Numbers. Carus Monograph No. 11. By I. NIVEN. (London: Chapman and Hall.) [Pp. xii+164.] Price 24s.

Surface Area. By L. CESARI. Princeton University Press. (London: Cumberlege.) [Pp. x+594.] Price 68s.

Viscous Flow Theory. I: Laminar Flow. By S. PAI. (Van Nostrand Co.) [Pp. 384.] Price 58s. net.

Analysis of Deformation. Vol. 3. By K. SWAINGER. (London: Chapman & Hall.) [Pp. xxvii+266.] Price 65s.

- Changes of State.* By H. N. V. TEMPERLEY. (London : Cleaver-Hume Press Ltd.) [Pp. xi+324.] Price 50s.
- The Theory of Suspension Bridges.* By Sir ALFRED PUGSLEY. (London : Edward Arnold Ltd.) [Pp. vii+136.] Price 42s.
- The Analysis of Engineering Structures.* By A. J. S. PIPPARD and J. F. BAKER. (London : Edward Arnold Ltd.) [Pp. xii+564.] Price 60s.
- Contributions to the Theory of Nonlinear Oscillations.* Vol. III. Edited by S. LEFSCHETZ. (Princeton University Press. London : Oxford University Press.) [Pp. vi+285.] Price 32s.
- Théorie des Circuits de Télécommunication.* By V. BELEVITCH. (Louvain : Librairie Universitaire.) [Pp. viii+384.] Price (Belgian francs) 450.
- Relaxation Spectrometry.* By E. G. RICHARDSON. (Amsterdam : North-Holland Publishing Company.) [Pp. viii+140.] Price 40s.
- Geometric Algebra.* By E. ARTIN. (New York : Interscience Publishers, Inc. London : Interscience Publishers Ltd.) [Pp. x+214.] Price \$6.00.

CORRIGENDUM

Amendment to "A Method for the Mapping of Vector Potential Distributions in Axially Symmetrical Systems", by the late Dr. G. LIEBMANN, published in *Phil. Mag.* (7), **61**, 1143-1151, 1950. By F. C. GAIR (A.E.R.E., Aldermaston).

EQUATION (7) does not follow from (6), which is the wrong transformation to use.

Instead, let

$$\begin{aligned} r &= \{(1-k)\rho\}^{1/1-k} & (k \neq 1) \\ r &= r_0 e^{\rho} & (k=1, r_0 = \text{constant}) \end{aligned}$$

but leave z untransformed.

Then, eqn. (9) becomes :

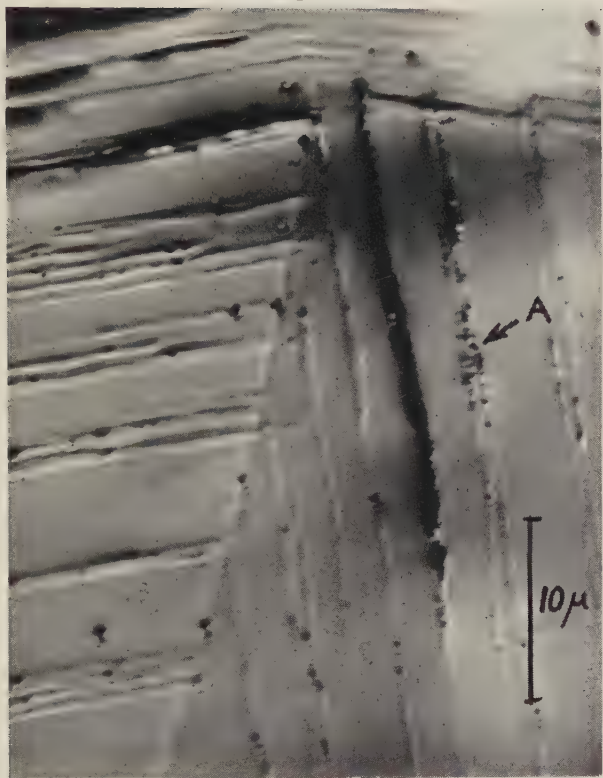
$$r^{2k} \frac{\partial^2 f}{\partial z^2} + \frac{\partial^2 f}{\partial \rho^2} = r^{2k} g^*.$$

For meshes of unit length in both r and z directions, the appropriate resistors can be specified by eqns. (10) ($k \neq 1$), and the currents to be fed in by eqn. (11).

In both figs. 1 and 2, R_2 and R_3 are labelled the wrong way round. In fig. 3, the label on R_2 has been omitted.

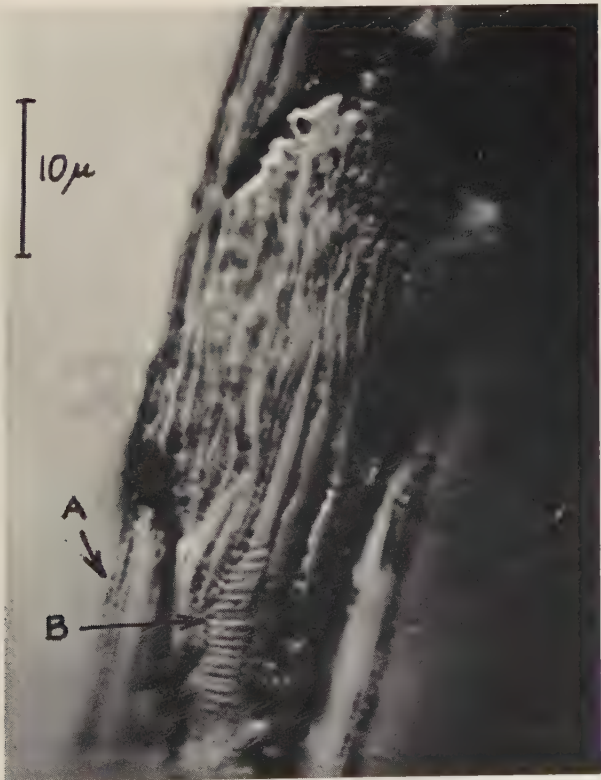
[The Editors do not hold themselves responsible for the views expressed by their correspondents.]

Fig. 1



Fatigue specimen repolished to remove approximately 4 microns. $\times 2500$.

Fig. 2



A section through a group of damage bands. $\times 2000$.

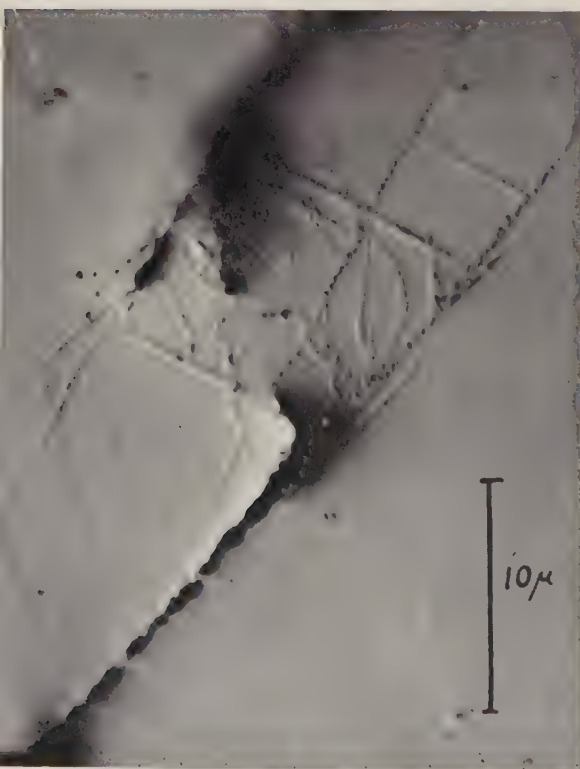
Fig. 4



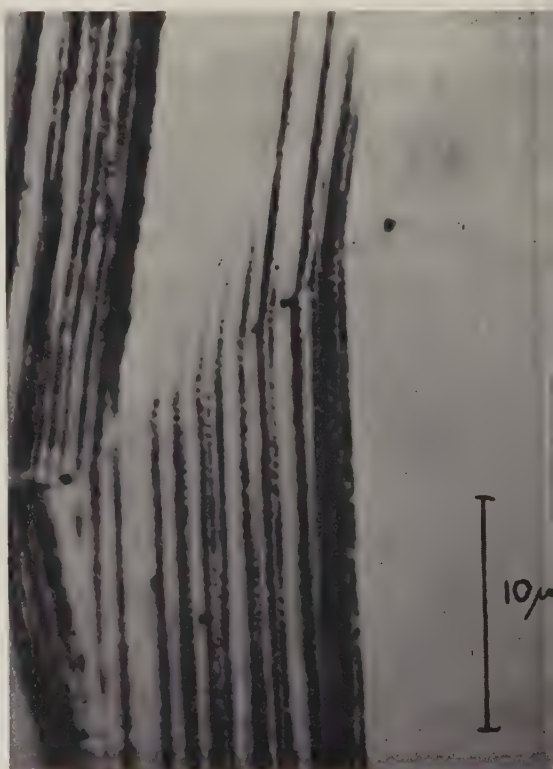
Grain boundaries and sub grains after electropolishing and etching for 20 sec in Wassermann's reagent. $\times 3000$.

Fig. 5

Fig. 6



Section through approaching fatigue cracks.



As polished specimen surface after fatigue. $\times 3000$



Fig. 1

Pattern from 2 Å of copper on rocksalt at 160°C [110] azimuth.

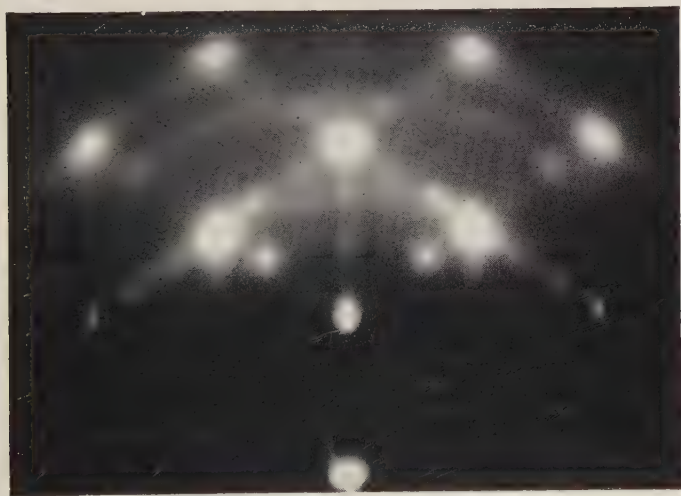


Fig. 2

12 Å of copper on rocksalt at 160°C.

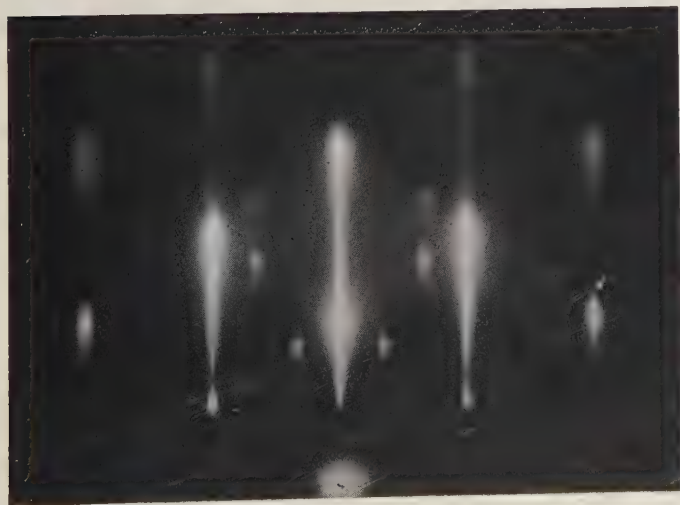


Fig. 3

160 Å of copper on rocksalt at 160°C.

Fig. 4



Pattern from 150 Å of gold on rocksalt at 295°C.
[110] azimuth. Glancing angle of 0.7°.

Fig. 5



As fig. 4, but glancing angle of 1.7°.

Fig. 1

Fig. 2

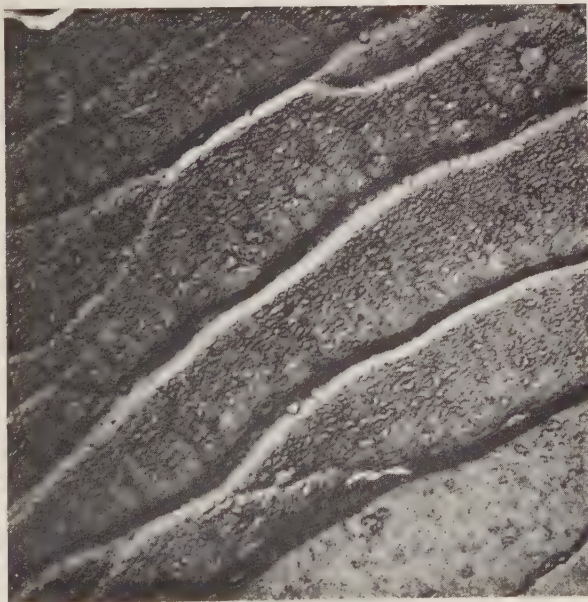


Light profile of steel slowly compressed 4%.
× 1700.

Deformation band in steel rapidly
compressed 4%. × 1700.

Fig. 3

Fig. 4



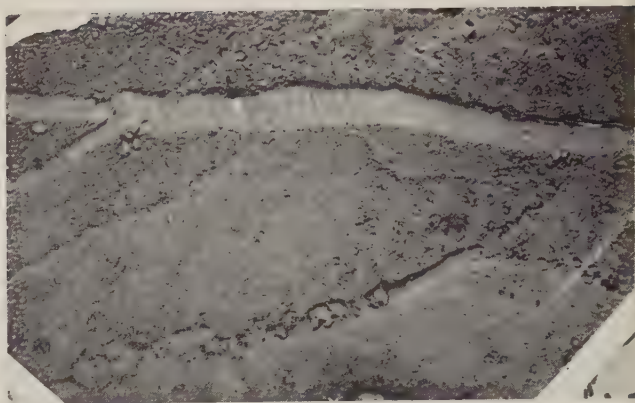
Rapidly compressed (8%) steel, sectioned.
electropolished and electrolytically
etched. Oblique illumination.
× 1700.

Coarse slip lines in slowly compressed ferrite.
× 7500.

Fig. 5



Slip steps following a grain boundary in rapidly deformed ferrite. $\times 7500$.



Structure of coarse slip step in slowly strained ferrite. $\times 7500$



Fig. 7

Coarse slip steps in slowly strained ferrite. $\times 7500$

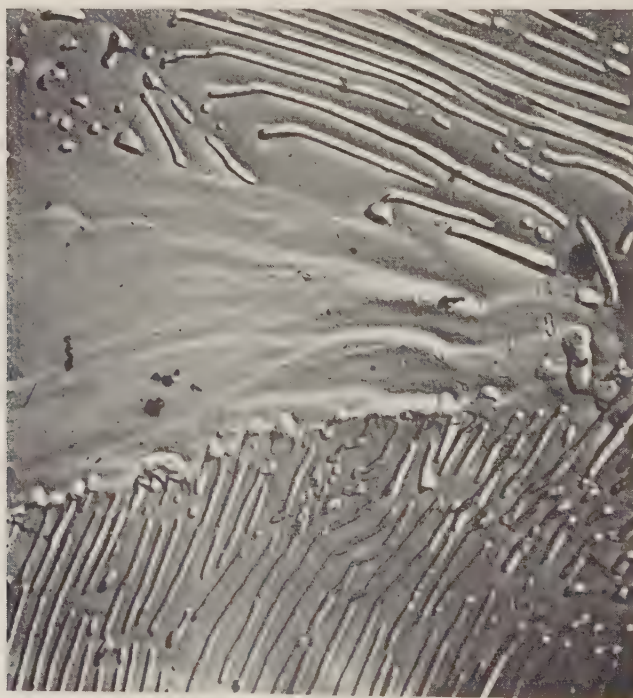
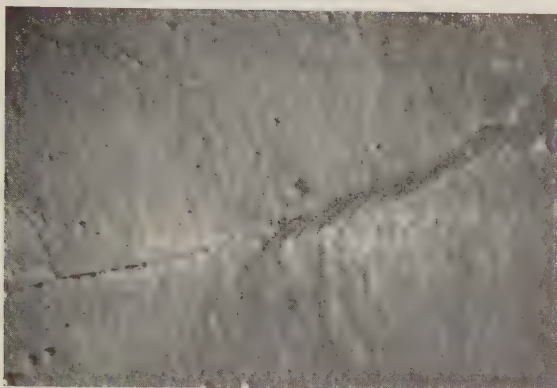


Fig. 8

Slip in slowly deformed ferrite devoid of precipitate. $\times 7500$

Fig. 9



Precipitation of carbide along ferrite grain boundary. $\times 7500$.

Fig. 10



Carbide precipitation in ferrite grain. $\times 7500$.

Fig. 11

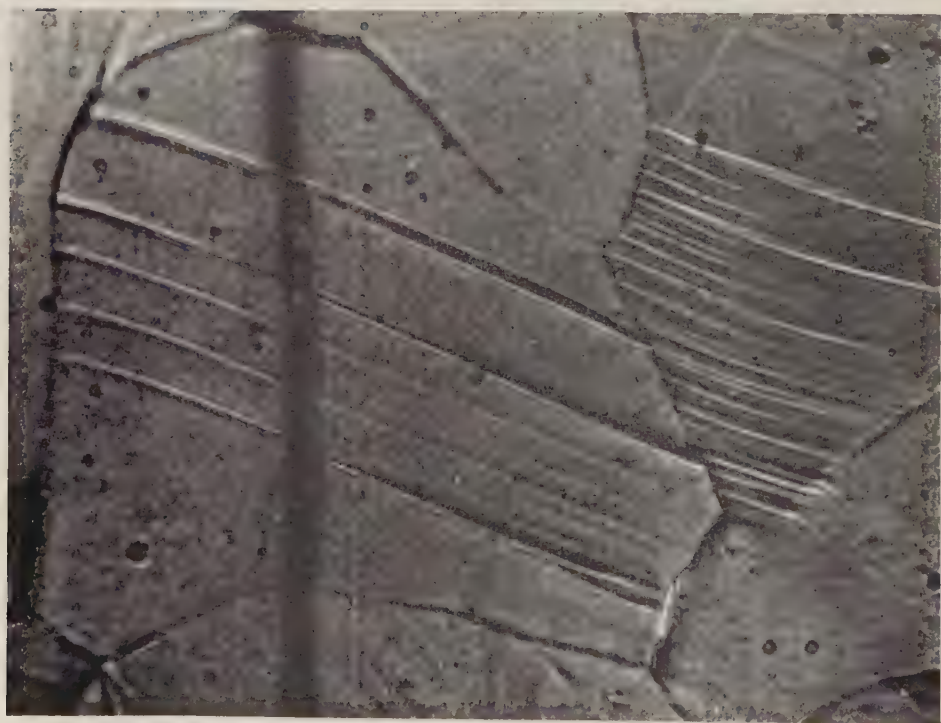


Carbide precipitation in ferrite grain. $\times 11,250$.

Fig. 12



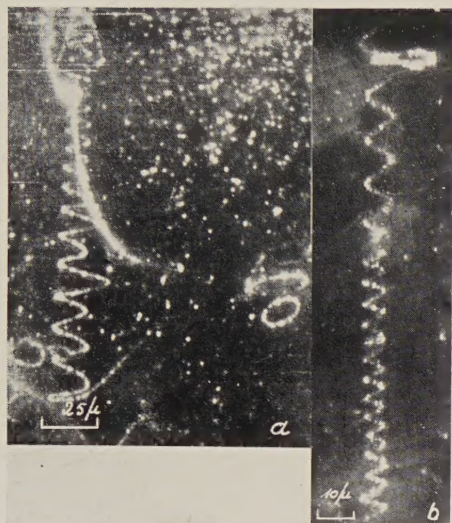
Fig. 13



Twins formed by impact in ferrite.

×1700.

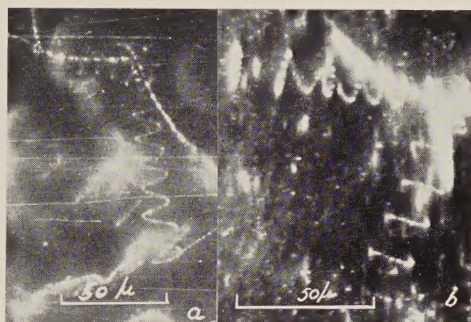
Photograph 1



(a) A helix with two windings of a larger radius. A single closed dislocation line can be observed.

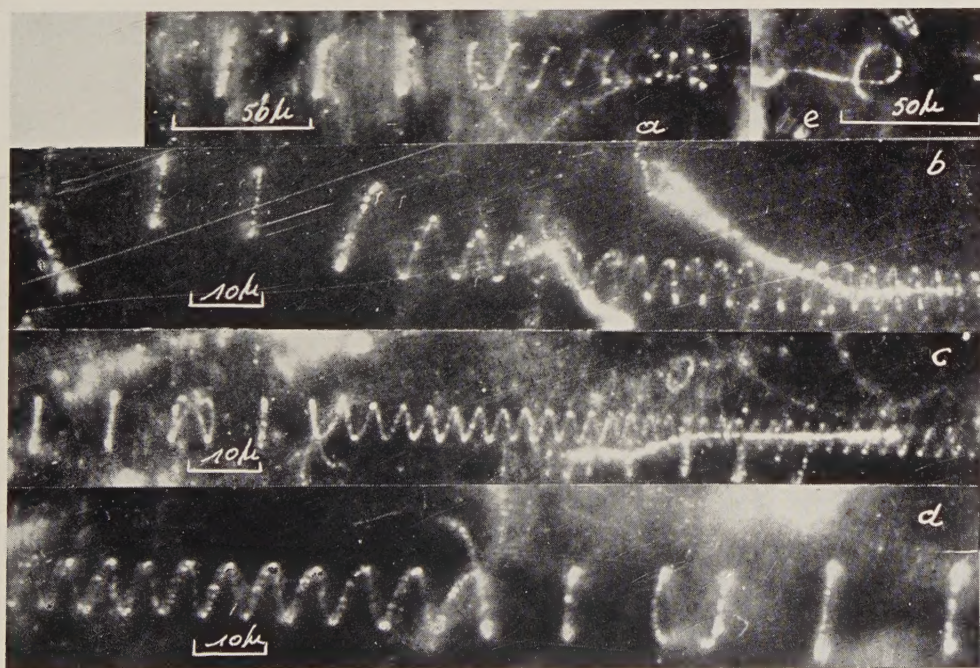
(b) Helix with variable radius and pitch.

Photograph 3



(a) and (b) Set of two helices forming angles of $\pm 60^\circ$ and 120° .

Photograph 2



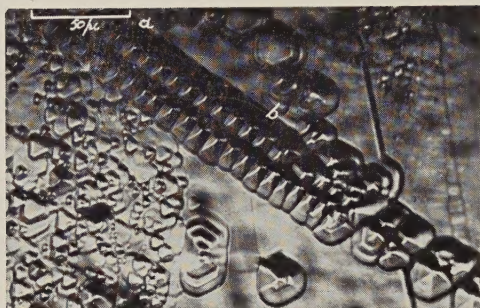
(a) Helix followed by a row of closed loops.

(b) Dislocation pattern which may be the result of the formation mechanism of fig. 2.

(c) and (d) Helices followed by a sequence of closed loops. Lissajoux like configurations can be observed.

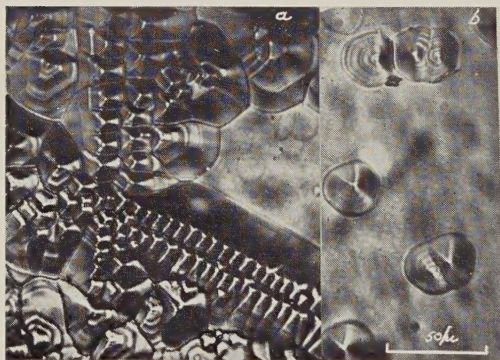
(e) Helical dislocation with only one winding.

Photograph 4



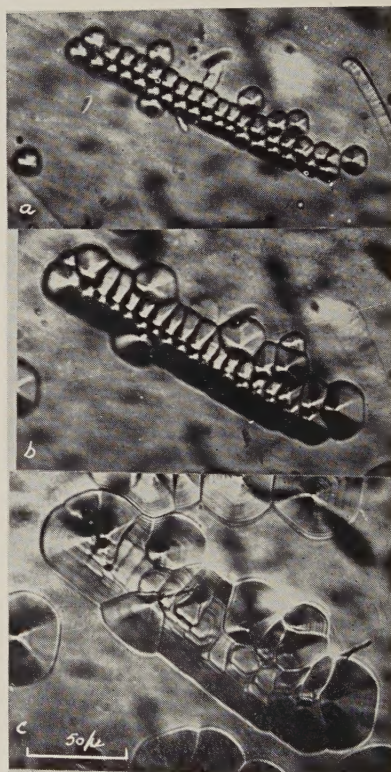
- (a) Etch structure of a helical dislocation line.
 (b) Etch structure of a row of closed loops.

Photograph 6



- (a) Etch pattern of two helical dislocations which form an angle of 115° .
 (b) Emergence points of isolated closed loops after etching.

Photograph 5

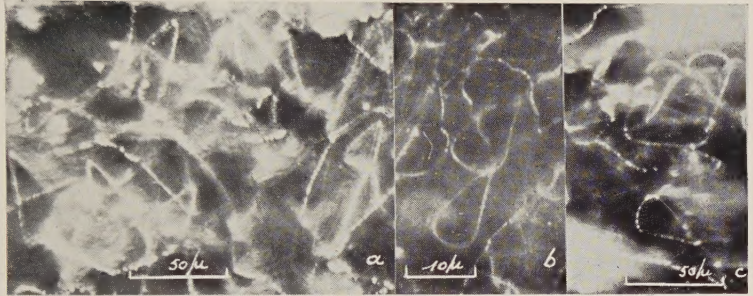


The etch structure of a helical dislocation after successive etchings. In (c) most of the pits have disappeared.

Photograph 7



Photograph 8

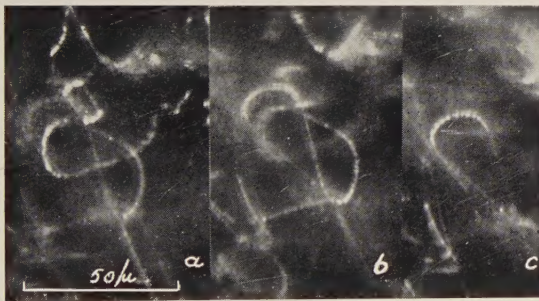


Photograph 7. (a) and (b) First stages of the Bardeen-Herring climb mechanism.

Photograph 8. (a) and (b) Climbing dislocations.

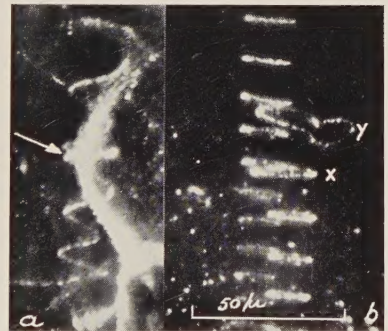
(c) A polygonized Bardeen-Herring source.

Photograph 9



Polygonized helix seen on different depths.

Photograph 10



(a) Influence of the interaction of dislocations on the shape of helical dislocations.

(b) Interaction between two rows of closed loops (*x* and *y*).

